All Dissertations

Dissertations

8-2017

Coaxial Cable Sensors Based on Fabry-Perot Interferometers and Their Applications in Distributed Sensing

Baokai Cheng

Clemson University, baokaic@g.clemson.edu

Follow this and additional works at: https://tigerprints.clemson.edu/all_dissertations

COAXIAL CABLE SENSORS BASED ON FABRY-PEROT INTERFEROMETERS
AND THEIR APPLICATIONS IN DISTRIBUTED SENSING

A Dissertation
Presented to
the Graduate School of
Clemson University

In Partial Fulfillment
of the Requirements for the Degree
Doctor of Philosophy
Electrical Engineering

by
Baokai Cheng
August 2017

Accepted by:
Dr. Hai Xiao, Committee Chair
Dr. Fei Peng
Dr. Lin Zhu
Dr. Pingshan Wang

ABSTRACT

Aging civic infrastructures in the world has put tremendous pressure in their

maintenances because potential failure of the large size civil structures will be

catastrophic. Structure health monitoring (SHM) has been proven effective to prevent

these failures, and distributed sensing technologies are preferred in SHM as they are

effective to provide comprehensive evaluation of the structures. Fiber optic sensors are

well developed in the past two decades for distributed sensing, but the lack of robustness

and the limited deformability of silica make them not suitable for heavy duty and large

deformation applications, which is very common in SHM. To address the above

limitation of optical fiber sensors, we change the sensing platform from optical fibers to

coaxial cable. Inspired by optical FPI, we created two reflectors on a coaxial cable to

form a coaxial cable Fabry-Perot interferometer (CCFPI). The reflectors are commonly

made by drilling half way holes or crimp on the cable, which introduce impedance

discontinuity and hence partial reflection of EM wave in the cable. The two reflectors can

produce interference patterns with multiple resonant frequencies which can be tracked to

indicate changes in physical parameters such as temperature and strain. To realize

distributed sensing, multiple reflectors are implemented along a coaxial cable, where

every two consecutive reflectors will form a low finesse CCFPI. A specific signal process

technique is used to reconstruct each individual CCFPI interferogram from the complex

frequency domain signal. As examples of the distributed sensing capability of the coaxial

cable platform, distributed torsion sensing and 3D beam shape estimation system are

demonstrated in this thesis. By modifying the cable material and structure, we can

achieve other special function for CC-FPI sensors. By fabricating the cable with ceramics as dielectric material and implanting built in reflectors, a high temperature CC-FPI sensor is developed and tested. Another example is a magnetic field sensor made by filling a cavity in a semi-rigid cable with ferrofluid. When external magnetic field change, the property of the ferrofluid will also change, resulting in spectrum shift of the FPI.

The coaxial cable FPI sensors have many potentials to measure different physical parameters in distributed sensing form, which makes it a very good sensing platform for long distance and distributed sensing in harsh environment and heavy duty applications.

DEDICATION

This dissertation is dedicated to my family; I love you.

ACKNOWLEDGMENTS

First, I would like to express my sincere gratitude to my advisor Prof. Hai Xiao for the continuous support of my Ph.D study and related research, for his patience, motivation and immense knowledge. His guidance helped me in all the time of research and writing of this thesis. I could not have imagined having a better advisor and mentor for my Ph.D study.

I would also like to thank the rest of my committee members: Prof. Lin Zhu, Prof. Fei Peng and Prof. Pingshan Wang, who are more than generous with their expertise and precious time, for their insightful comments and encouragement, but also for the hard question which incented me to widen my research from various perspectives.

I thank my fellow labmates for all the stimulating discussion, the sleepless night we were working together and for all the fun we have in the last few years.

Finally, I want to thank my wife, Xia Fang, for always standing beside me and encouraging me to overcome all the difficulties in my life, and my son, Kyler, for the joys, responsibilities and wonderful moments you brought to me.

TABLE OF CONTENTS

Table of Contents (Continued)

LIST OF TABLES

LIST OF FIGURES

List of Figures (Continued)

List of Figures (Continued)

List of Figures (Continued)

List of Figures (Continued)

CHAPTER ONE

I.   INTRODUCTION

1.1 Sensors for structure health monitoring

Due to inadequate maintenance, excessive loading and adverse environmental conditions, civil infrastructures are deteriorating and in a state of disrepair. In addition to the normal loads, unexpected forces from nature and human disasters such as earthquakes, hurricanes, floods and terrorist attacks are also threatening the state of their conditions. Potential failure and collapse of these structures have to be prevented to avoid catastrophic impact on economy and human lives. Structure health monitoring (SHM) is one of the most powerful tools to manage the challenge to monitor and maintain the structures in a satisfactory state. A typical SHM system consists of a network of sensors that monitor the relevant parameters of the state of the structure. The interested parameters include physical quantities such as strain, temperature, position, deformation, pressure, vibration; chemical quantities such as PH value, humidity; and other environmental parameters such as air temperature, wind speed, etc. Comprehensive evaluation of the health status of the structure as a whole prefers distributed sensing to provide spatially-uninterrupted information along the entire span of the structure. Conventional sensors based on mechanical or electrical transducers have the ability to measure most of the parameters, but they are usually difficult to deploy over large scale structures or cannot survive harsh environments. For distributed sensing, multiplexing the sensors usually requires cumbersome wiring.

In the past two decades, fiber optic sensors have attracted increasing interest and emerged as a mainstream technology in SHM due to their advantages such as high sensitivity, compactness, immunity to electromagnetic interference, chemical stability, remote operation, and multiplexing capability [1]. A widely used fiber sensor network scheme is cascaded fiber Bragg gratings (FBGs) [2][3]. In this scheme, weakly reflection FBGs are cascaded along a single optic fiber and interrogated by an optical spectrum analyzer or optical edge filter. The FBGs have different Bragg wavelengths so that the spectrum shifts can be determined unambiguously. Besides FBGs, fiber optic interferometers such as Fabry-Perot interferometers (FPIs) can also be multiplexed. As an example, cascaded FPIs with different cavity lengths can be multiplexed onto a fiber. During interrogation, different FPIs can be identified by Fourier transform the optical interferogram. However, the multiplexed sensing technique is only quasi-distributed or spatial-interrupted. The parameters are only measured at discrete sampling points, leaving dark zone between them. Fiber optic sensors based on back-scattered signals generated by elastic (e.g., Rayleigh) [4] or inelastic (e.g., Raman or Brillouin) [5] scattering can achieve spatially continuous measurement or truly distributed sensing. Typical probing method in these sensors is called optical time domain reflectometry (OTDR) [6]. In OTDR, an optical pulse is sent along a fiber, and the reflections from the back-scattered signal are collected and recorded in time domain. TDR based distributed sensing can cover a long range and keeps spatial continuity, but the measurement resolution is generally low because of the inherent weak back-scattering. To increase the SNR and resolution, optical frequency domain reflectometry (OFDR) [7] can be used. In OFDR, a

2

frequency scanning laser is used to probe the back-scattering signal in frequency domain, which is then interpreted in time domain by Fourier transform. OFDR has high SNR and spatial resolution comparing to OTDR thanks to its high throughput, but has shorter coverage length than OTDR. The back-scattering based fiber optic distributed sensors are mostly used for strain and temperature sensing.

However, a major disadvantage that limit the application of fiber optic sensors in SHM is their lack of robustness. Conventional fiber sensors are based on pure silica glass fibers. These fibers are fragile and have a limited deformability, causing the sensors to have a small dynamic range. When subject to large strain above 0.4% or a shear force, the fiber sensors can easily break even with rigorous packaging. This disadvantage greatly limited the fiber optic sensors applications because heavy duty or large strain measurements are common in SHM. Comparing to optical fibers, coaxial cables share the same principle regarding guidance of electromagnetic waves. To address the above limitation of optical fiber sensors, we change the sensing platform from optical fibers to coaxial cable. Physically, coaxial cables are more robust, capable of surviving large strain and relatively resistant to lateral forces. From the electromagnetic point of view, optical fibers and coaxial cables are two basic forms of cylindrical structure that guide EM waves and share the same fundamental physical principles, although the EM wave frequency supported in optical fiber (optical frequency) is much higher than that in coaxial cable (RF frequency). Inspired by optical fiber sensor devices, coaxial cable sensors are made in our lab. Due to the robustness and relatively high measurement accuracy, this kind of sensor is an attractive alternative to fiber sensors in SHM.

1.2 Fiber optic and coaxial cable sensors

As discussed above, coaxial cable and optical fiber are two possible platforms for distributed sensing. They are two basic waveguides that guide or transmit electromagnetic(EM) waves with small losses. The EM wave signals provide information for sensing parameters along the waveguide, while the small loss can assure long distance operation. Figure 1.1 shows the structure of coaxial cable and optical fiber. We can see that they have similar structures and share the same fundamental physics.

(a)   (b)
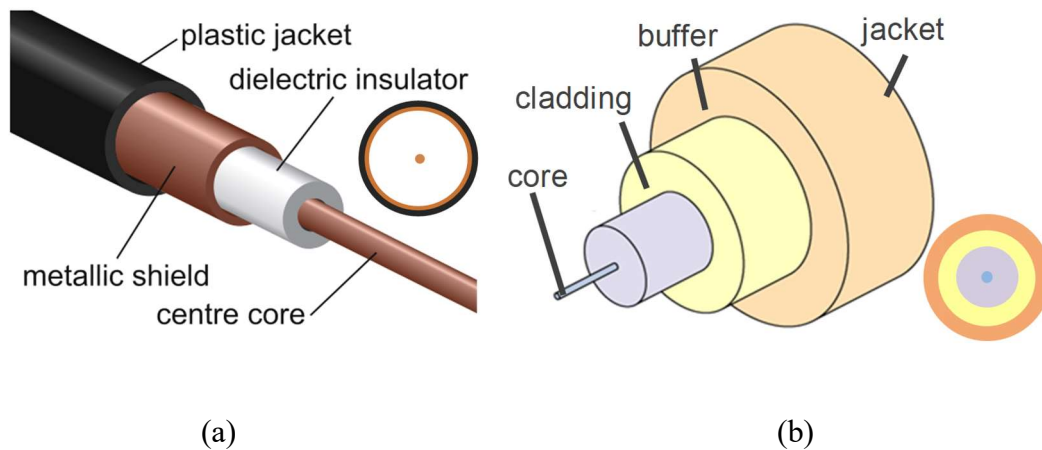
Figure 1.1. Structure of (a) coaxial cable and (b) optical fiber.

The differences of these two kinds of waveguides are also significant. For operating EM wave frequency, the optical fiber support optical frequency, which is about 1015 Hz, while the coaxial cable support radio frequency (RF) or microwave frequency, at the range of hundreds of MHz to several GHz. The material that makes the fibers is optical grade materials such as silica and sapphire, and the materials for coaxial cables are good

conductors and good dielectric, with a lot of choices. The size of a fiber is small (e.g., 125μm OD for silica fiber, 70μm OD for sapphire fiber) but fragile, while coaxial cables have relatively large size and robust. In fiber optical system, signals are excited and probed in optical form using devices such as lasers and photodetectors, but processed in electrical form. In coaxial cable system, signals are excited probed and processed all in electrical forms. Comparing to optical fibers, the coaxial cable platform has the quite some special features. They always operate in single mode, which eliminate some problems concerning multimode operation. They can also deliver power while transmitting signals, which could bring some convenience such as power distributed filters and amplifiers. There are lots of commercial off-the-shelf components available, such as amplifiers, phase lock loop and filters. They can also have direct modulation and detection in multiple ways such as amplitude, polarization, phase and frequency. Because coaxial cables are developed long before optical fibers, in the early time when optical fiber were developed, a lot of coaxial cable devices are migrated into fiber optic devices, such as couplers and resonators. However, because of the advantages optical fibers such as low loss, immune to EM interference and high chemical resistance, optical fiber sensors received a lot of attention, hence many fiber optic sensor devices have been developed. It is now a good chance to migrate some of the fiber optic sensor devices back to coaxial cable platform. A very important example is the fiber Bragg gratings (FBG) which has been developed in the past 20 years and have numerous applications in optical fiber communication and sensing areas. Inspired by the principle FBG, coaxial cable Bragg gratings have been developed recently.
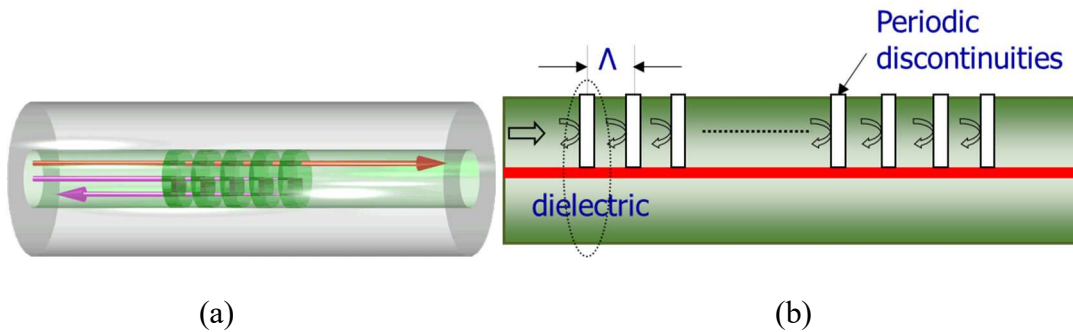
Figure 1.2. The structure of (a) FBG and (b) coaxial cable Bragg grating.

Just like the FBGs, coaxial cable Bragg gratings can reflect EM waves at selected frequency bands according to the parameters of the gratings, such as the pitch length, material dielectric constants and cable dimensions. The coaxial cable Bragg grating will respond to environment temperature and strain applied to the cable with the frequency shift of the reflection EM wave frequency. The problem of coaxial cable Bragg gratings is that the device is relatively big, with the pitch length of several centimeters and tens of periods, the device could be as long as in meters. The large dimension of the device limited the application of it. Another kind of fiber optic sensor device is a fiber Fabry-Perot interferometer (FPI). Unlike the coaxial cable Bragg grating, the coaxial cable FPI only have two reflectors as their optical counterpart, which is only a few centimeters long. The coaxial cable FPI can respond to temperature and strain applied to the cable, and can be made into other sensors if proper working media is integrated into the cavity.

1.3 Coaxial cable FPIs

FPI is an important interferometer in optics. It consists of two partially reflection mirror, as shown in Figure 1.3.
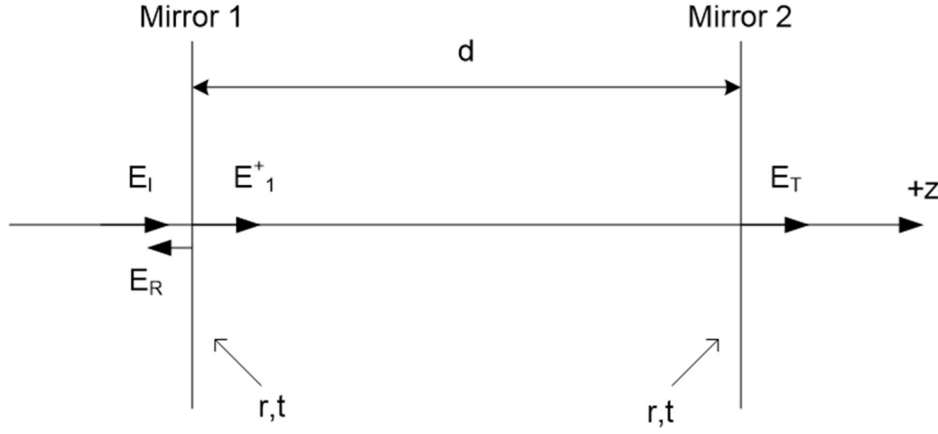
Figure 1.3. Schematic of a FPI.

Assume that the two mirrors are identical and the reflection and transmission of each mirror is r and t. The distance between the 2 mirrors is d. δ is the phase difference between the two mirrors. The electric field of the incident light is E_I, the electric field of the reflected light is E_R and the electric field of the transmitted light is E_T. E_{0I}, E_{0R} and E_{0T} are the amplitude of E_I, E_R and E_T.The relationship between these quantities are

$$r^2 + t^2 = 1$$

$$\delta = 2kd$$

$$E_I = E_{0I}e^{i\omega t}$$

The transmission of this FPI is the power of the transmited light devided by the power of the incident light, and can be calculated as

$$T = \frac{I_T}{I_I} = \frac{E_{0T}E_{0T}^*}{E_{0I}E_{0I}^*} = \frac{t^4 e^{-\frac{i\delta}{2}}e^{\frac{i\delta}{2}}}{(1 - r^2 e^{-i\delta})(1 - r^2 e^{+i})}$$

$$= \frac{t^4}{1 + r^4 - 2r^2 cos\delta} = \frac{(1 - r^2)^2}{1 + r^4 - 2r^2 cos\delta}$$

If cos(δ) is replaced represented by 1- $sin^2(\frac{\delta}{2})$ by trigonometric identity, we can obtain

the Airy function as shown below

$$T(\delta) = \frac{1}{1 + \left[\frac{4r^2}{(1 - r^2)^2}\right] sin^2(\frac{\delta}{2})}$$

When the transmission of the Fabry-Perot cavity T is plotted against the phase difference

between the two reflections on the cavity ends δ, we can have a curve with peaks and

valleys in the spectrum at different positions. A small change in the phase will cause the

peak or valley position to change, which is the principle of FPI working as sensors.

In optical FPIs, the reflectors are usually partially reflection mirrors. Here, if we

want to make a FPI on coaxial cable, a partial reflector should be made on the cable. A

reflection on coaxial cable will happen when there is an impedance mismatch. The

characteristic impedance is calculated from the R, G, L, C of the equivalent circuit of the

coaxial cable. Those parameters are determined by the material properties and the

geometry dimensions of the cable.

To create impedance mismatch, we can change either the material or the geometry

on the cable. In our research work, we found two relatively easy ways to make reflectors.

The first one is hole drilling, where a half-way hole is drilled on the selected position of a

cable, as shown in Figure 1.4(a). It is worth noting that the drill shall not destruct the

center conductor of the cable, thus the drilling should stop before touching the center

conductor. The other way is ferrule crimping, as shown in Figure 1.4(b). Here, a

cylindrical metal ferrules that have an inner diameter slightly larger than the outer diameter of the cable is crimped on selected locations, and the crimping depth will influence the reflection intensity. For half-way hole drilling, the structure is not stable, and there are package issues. Crimp ferrule is easier and no package problem, so we tend to use this method to create reflectors in our work.

| (a) | (b) |
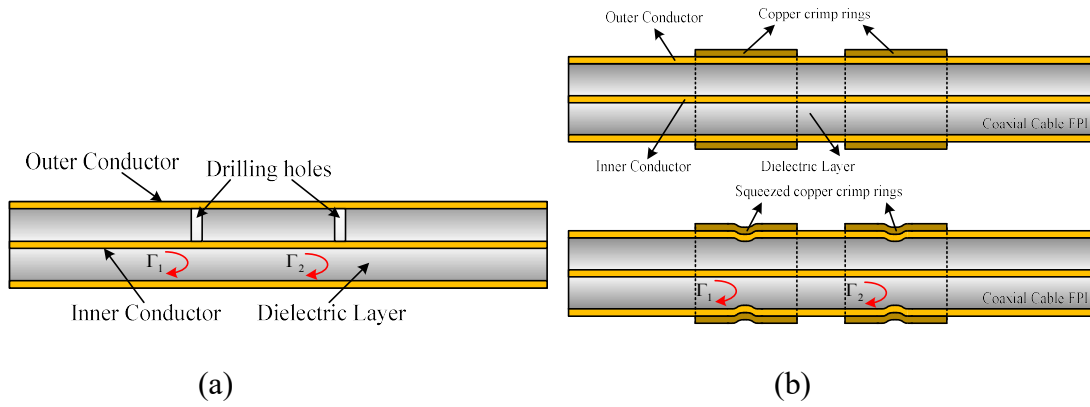
Figure 1.4. Reflectors created on coaxial cables by (a) whole drilling and (b) ferrule crimping.

1.4 Dissertation outline

In this dissertation, principle and applications of coaxial cable FPI sensors are discussed.

Chapter 2 introduced the principle of the coaxial cable FPI sensors and their characteristics. The spectrum change with regard to environment temperature and strain of the sensor is discussed. The joint-time-frequency domain demodulation method is used to realize distributed sensing capability of cascaded coaxial cable FPIs.

In chapter 3, a high temperature coaxial cable FPI sensor is made by drilling holes on commercially available ceramic coaxial cable. The sensor works below 550 C, but above 600C, the spectrum shift of the sensor became abnormal. The main reason is the dielectric material in the cable cannot survive high temperature.

To overcome this difficulty, a metal ceramic coaxial cable FPI sensor is developed in the lab, which is discussed in chapter 4. Cable materials are selected and dimensions are designed. The reflectors can be built in the cable during fabrication process, instead of hole drilling or ferrule crimping. The thickness of the thin disk reflector or air gap is discussed to achieve proper reflection and stability. The fabricated sensor is tested up to 900C with good temperature response as well as repeatability.

Apart from temperature sensor, coaxial cable strain sensing also has a lot of applications. Chapter 5 demonstrated a coaxial cable distributed torsion sensor, which has potential application in petroleum industry. A commercial coaxial cable with multiple reflectors on it is arranged along a shaft in spiral form, which transfer the torsion of the shaft into the strain of the cable. By analyzing the strain distribution along the cable, the torsion distribution on the shaft can be calculated.

The distributed strain sensor can also be used for 3D beam shape estimation, as demonstrated in chapter 6. Here, two coaxial cable sensors are arranged along a beam in orthogonal position to measure the strain distribution of the beam in y and z direction. Using displacement-strain transformation(DST), the shape of the beam can be estimated in real time.

Other than temperature and strain sensing, the CC-FPI sensor can be modified to measure other parameters. Chapter 7 discussed the development of a magnetic field sensor based on CC-FPI structure. A section of the dielectric material is cut away from a semi-rigid cable to create a cavity. The cavity is then filled with ferrofluid which is a type of magnetic nanoparticle dispersed colloidal suspension that will change its property under external magnetic field. The sensor is tested up to 160 Gauss and the spectrum shift shows a linear response to external magnetic field.

CHAPTER TWO

II. COAXIAL CABLE FPI SENSOR AND DISTRIBUTED SENSING

2.1 Coaxial cable Fabry-Perot interferometer

Coaxial cable FPIs have many similarities to traditional fiber optics FPIs. A typical fiber optic FPI is illustrated in Figure 2.1. Two reflectors are written on the commercial SMF to build a FPI cavity, with a spacing of tens to hundreds of micrometers. The two reflected light has a phase delay, which is related with the wavelength of the transmitted light. In the spectrum domain, the reflectance performs a sinusoidal wave, i.e., an interferogram spectrum. Variation of environment temperature and/or tensile force could bring in the change of the physical length and/or the property of the dielectric within the FPI cavity, resulting in a corresponding shift of spectrum. The shift could be used to identify the change in temperature and/or strain.
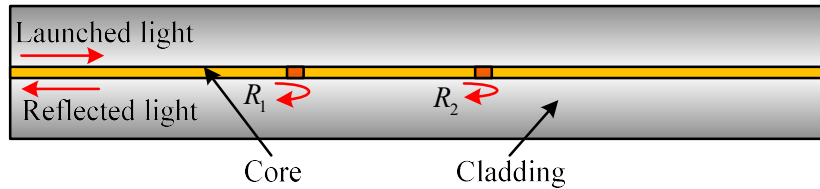
Figure 2.1. Schematic of optical fiber FPI

In the same way, the coaxial cable Fabry-Perot interferometer (CCFPI) could be fabricated based on the aforementioned principle, shown in Figure 2.2. Since the negligible scattering in RF waveguide, the two small reflections in CCFPI are easier to generate than fiber optic FPI. Hole-drilling on dielectric material and outer conductor-

clamping are two typical ways to make the reflectors. When an EM wave is launched into the coaxial cable, the power will be partially reflected at two reflectors. The reflected wave is a superposition of the two reflections with a phase difference. Similar to the fiber optic FPI, there would exhibit interferogram in frequency domain.
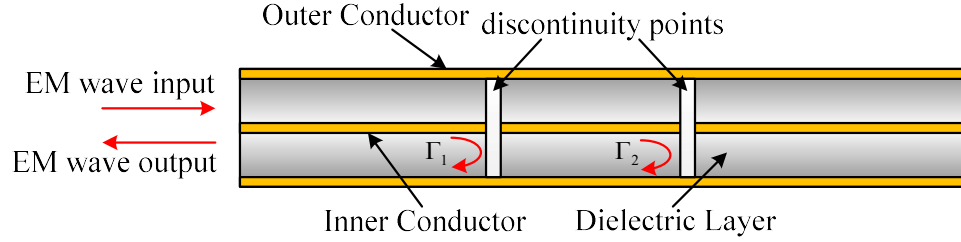
Figure 2.2. Schematic of CCFPI

The two reflectors can be engineered to have a low reflectivity. As a result, multiple reflections between two reflectors can be negligible in the calculation. Assuming the amplitude reflection coefficients of the two reflectors are the same, the two reflected waves (U1 and U2) can be written as

$$U_1 = \Gamma(f)e^{-\alpha z}\cos(2\pi f t)$$

$$U_2 = \Gamma(f)e^{-\alpha z}\cos[2\pi f(t+\tau)]$$

$$\tau = \frac{2d\sqrt{\varepsilon_r}}{c}$$

where $\Gamma(f)$ is the amplitude reflection coefficient of the reflector; f is frequency of the EM wave traveling inside the cable; α is the propagation loss coefficient; z denotes the cable axial direction; t is time delay between the two reflected waves; d is the distance between two reflectors; εr is the relative permittivity of the inner dielectric material of the cable; c is the speed of light in vacuum.

The two reflected waves have a time delay and the delay is associated with the distance between the two reflectors and the phase velocity of the wave. The interference signal (U) is the summation of the two reflected waves, which can be written as

$$U = 2\Gamma(f)e^{-\alpha z}\cos(2\pi f\tau)\cos[2\pi f(t+\tau)]$$

The equation describes a wave with its amplitude given by $2\Gamma(f)e^{-\alpha}\cos(2\pi f\tau)$ and its phase of $2\pi f\tau$. The amplitude and phase vary as functions of frequency and the delay. In essence, the amplitude of spectrum varies sinusoidally as the frequency of wave is scanned.

In the equation, the only unknown parameter is the reflection coefficient $\Gamma(f)$. A partial reflector can be generated by introducing an impedance discontinuity in a coaxial cable.

2.2 Temperature and strain impact on the CCFPI

From the theory of Fabry-Perot interferometer, the resonance frequencies could be expressed as

$$f_N = \frac{N}{\tau}, \quad N = 1,2,3,\dots$$

Where τ is the time delay between the two reflectors, a function of the distance (d) and dielectric constant (ε_r) between the interference cavity, given by

$$\tau = \frac{2d\sqrt{\varepsilon_r}}{c}$$

where c is the speed of light in vacuum. In differential form, the relative resonance frequency shift can be expressed as

$$\frac{\Delta f_N}{f_N} = -\frac{\Delta d}{d} - \frac{1}{2}\frac{\Delta \varepsilon_r}{\varepsilon_r}$$

When the coaxial cable is elongated with the strain change of $\Delta \varepsilon$, the length of the cable

(d) will expand by Δd and the dielectric constant (ε_r) would decrease by $\Delta \varepsilon_r$.

$$\frac{\Delta d}{d} = \Delta \varepsilon, \quad \frac{\Delta \varepsilon_r}{\varepsilon_r} = -P_{eff}\Delta \varepsilon$$

Where P_{eff} represents the effective Pockels coefficient of the inner dielectric material in

the coaxial cable. Therefore, the relative resonance frequency shift can be rewritten by

$$\frac{\Delta f_N}{f_N} = \left(\frac{P_{eff}}{2} - 1\right)\Delta \varepsilon \cong -\Delta \varepsilon$$

Since the value of Pockels coefficient is usually less than one, the strain change ($\Delta \varepsilon$) is

approximately the same value as the relative resonance frequency shift.

Figure 2.3 shows the experiment setup for a coaxial cable strain sensor. The dynamic

range of the strain test was from 0 to 1000 $\mu\varepsilon$ (0 to 0.65 mm) with fourteen steps,

controlled by a digital force tester (Chatillon TCD225). Figure 2.4(a) shows that the

interference resonant frequency shifts towards high frequency as the applied strain

increases. The trend of the frequency shifts as a function of applied strain matched well

with the theoretical prediction model. The test was conducted for three times to validate

the repeatability of the sensor. The resonant frequency as a function of applied strain of

the three test results ARE plotted in a Figure 2.4(b). In general, the resonant frequency

shifts towards higher frequency as applied strain increases, following a linear

relationship.
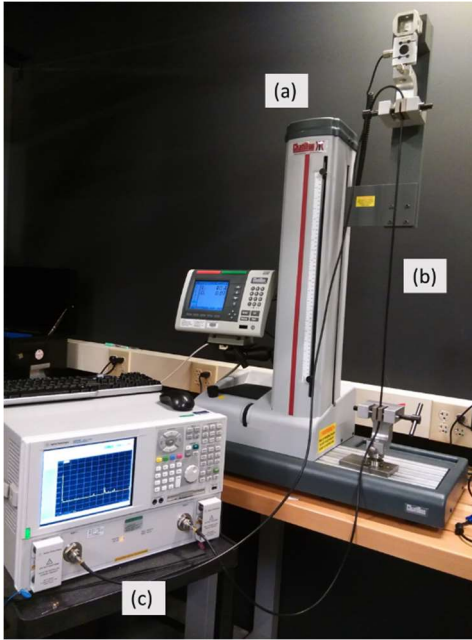
Figure 2.3. Test setup of strain sensor. (a) force tester, (b) cable under test, and (c) VNA.

(a)

(b)
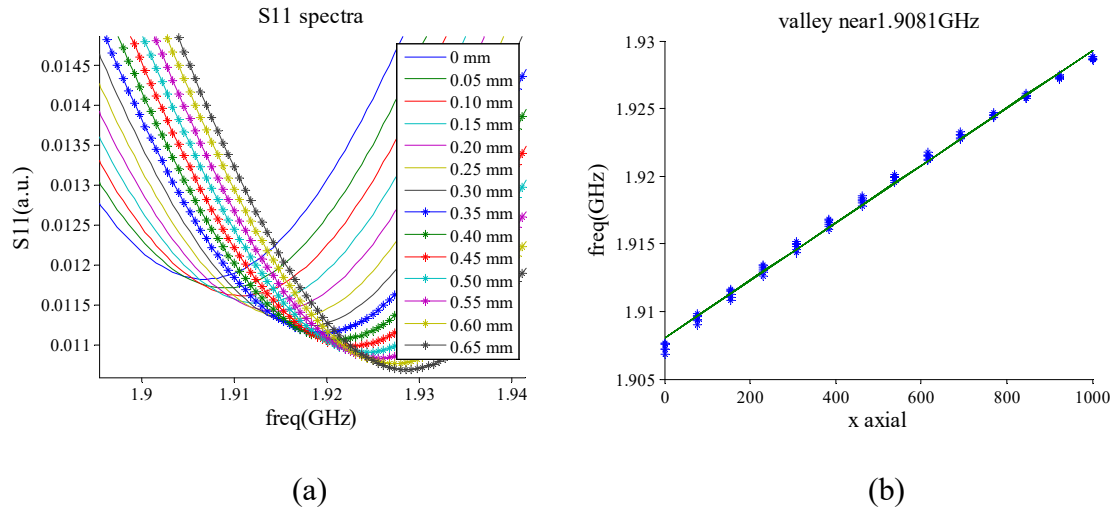
Figure 2.4. (a) Microwave interferograms at different applied strain. (b) Interference

resonant frequency shift as a function of applied strain.

When the ambient temperature around the cable increases by ΔT, both dielectric constant (ε_r) and length (d) would change by Δd and $\Delta\varepsilon_r$, respectively.

$$\frac{\Delta d}{d} = \alpha_{CTE}\Delta T, \frac{\Delta\varepsilon_r}{\varepsilon_r} = \alpha_{TCK}\Delta T$$

where α_{CTE} and α_{TCK} are the temperature coefficients of thermal expansion and dielectric constant, respectively. Combining these two factors together, the relative resonant frequency shift can be rewritten by

$$\frac{\Delta f_N}{f_N} = -\left(\frac{\alpha_{TCK}}{2} + \alpha_{CTE}\right)\Delta T$$

The equation above indicates that both thermal expansion and dielectric thermal effect can contribute to the relative resonant frequency shift. We now discuss the crosstalk between temperature and strain on CCFPI.

When a coaxial cable is under tension in ambient temperature environment, the relative resonant frequency shift is related to both strain and temperature change.

$$\frac{\Delta f_N}{f_N} = \left(\frac{P_{eff}}{2} - 1\right)\Delta\varepsilon - \left(\frac{\alpha_{TCK}}{2} + \alpha_{CTE}\right)\Delta T$$

The relative resonant frequency shift is a simple superposition of the shifts induced by the strain change ($\Delta\varepsilon$) and temperature change (ΔT), respectively. Given all these coefficients (i.e., P_{eff}, α_{TCK}, and α_{CTE}), and the temperature change (ΔT) are obtained, theoretically we could readily get the strain change by the following expression.

17

$$\Delta\varepsilon = \frac{\dfrac{\Delta f_N}{f_N} + \left(\dfrac{\alpha_{TCK}}{2} + \alpha_{CTE}\right)\Delta T}{\dfrac{P_{eff}}{2} - 1}$$

Nevertheless, there would be an inevitable temperature random error or finite precision from practical gauges, such as a thermometer, even after calibration. The error could give rise to the temperature cross talk on the strain sensor and affect its sensing precision. For instance, assume that the P_{eff} is zero, α_{TCK} and α_{CTE} are 100 ppm/°C and 120 ppm/°C, respectively. When the precision of the temperature we can get is 0.1 °C, the temperature fluctuation can bring an equivalent strain variation of 170 $\mu\varepsilon$,

$$\Delta\varepsilon = \frac{\dfrac{\alpha_{TCK}}{2} + \alpha_{CTE}}{\dfrac{P_{eff}}{2} - 1}\Delta T \approx \left(\frac{\alpha_{TCK}}{2} + \alpha_{CTE}\right)\Delta T$$

in which case the intrinsic precision of the strain sensor is overwhelmed by the temperature cross talk. Therefore, in order to reduce and eliminate the temperature cross talk, the effective thermal coefficient should be lower enough.

$$|\alpha_{eff}| = \left|\frac{\alpha_{TCK}}{2} + \alpha_{CTE}\right| \leq 1$$

Likewise, when we design the temperature sensor, the strain effect should be eliminated.

2.3 Principle of cascaded coaxial cable FPIs for distributed sensing

We can cascade multiple FPIs on a single cable to fulfill distributed sensing, as illustrated in Figure 2.5. When multiple reflectors are inscribed or written on a signal

coaxial cable, the reflection spectrum (S11) is a superposition of these individual

reflections, including magnitude and phase information. When the reflection spectrum is

transformed to time domain, the reflected pulse could be distinguished, and pulses

correspond to the locations of reflectors, respectively. Any two consecutive pulses could

be picked up by applying a window to filter the unwanted signals. The two selected two

reflections in the applied window construct a single CCFPI sensor. Then the

interferogram of the selected FPI can be restored after transferring to the time domain.

The whole cable can be considered as a combination of multiple isolated FPIs. Since a

FPI sensor is able to identify the variation of physical length and dielectric constant

within the FPI cavity, the cable consisting of multiple CCFPIs could be spatially

continuous characterized as a fully distributed sensing network.
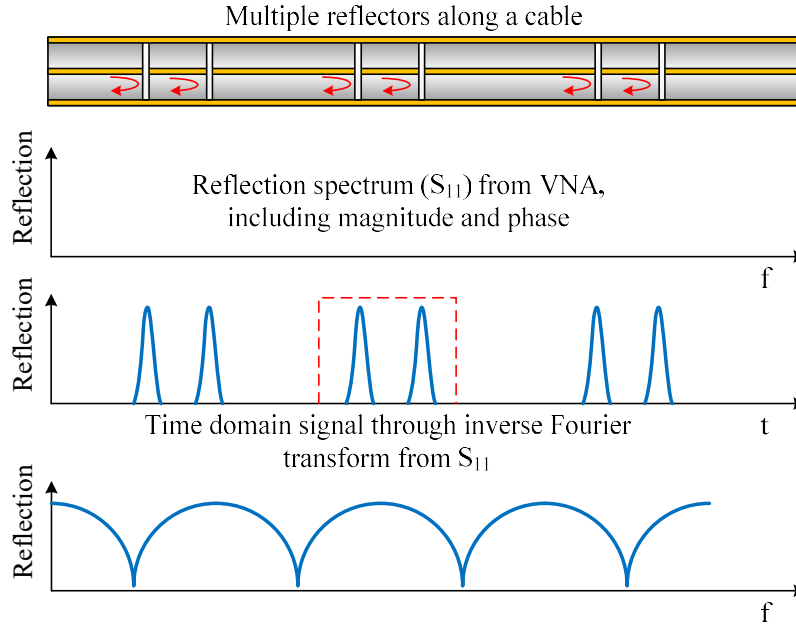
Figure 2.5. Interrogation of multi- FPI in a single coaxial cable for spatially continuous

fully distributed sensing.

19

To better understand the performance of the distributed sensing system, numerical study and simulation is conducted. Assume that the voltage of the microwave launched into the cable is given by

$$V_o = A \exp j\left(\omega t + \varphi\right)$$

Where t is the time, A is the amplitude, ω is the angular frequency, φ is the initial phase, and V_o is the voltage. The microwave travels in the cable, and a small portion of the power is reflected at each reflector along the path. Because the reflectors are weak, the multiple reflection between those reflectors are negligible. The total reflected signal is then the sum of the reflection from each reflector, and can be expressed as

$$V_{total} = \sum_{i=1}^{N} V_{o,i}\left(t, z_i\right)$$

Where N is the total number of the reflectors, z_i is the location of the i-th reflector. And $V_{o,i}$ is expressed by

$$V_{o,i}\left(t, z_i\right) = \Gamma_i A \exp j\left[\omega\left(t - \frac{2z_i\sqrt{\varepsilon_r}}{c}\right) + \varphi\right]$$

Where Γ_i is the reflection coefficient of the i-th reflector, c is the speed of light in vacuum, and ε_r is the effective relative dielectric constant of the coaxial cable medium.

We can calculate the transfer function of the distributed sensing system at frequency ω as the ratio of the total reflected signal over the source signal, expressed as

$$H(\omega) = \frac{V_{total}}{V_o} = A_{eff} \exp j\Phi_{eff} = \sum_{i=1}^{N} \Gamma_i \exp j\left(-\frac{2z_i\sqrt{\varepsilon_r}}{c}\omega \right)$$

Where A_{eff} is the amplitude of the transfer function, and Φ_{eff} is the phase of the transfer function.

In experiments, we usually sweep the microwave frequency over a given band. Let us assume that the swept frequency is from ω_{min} to ω_{max}. The impulse response of the system can be obtained by the microwave reflection spectrum with an inverse Fourier transform, as shown below.

$$h(t) = \frac{1}{2\pi} \int_{\omega_{min}}^{\omega_{max}} H(\omega) \exp(j\omega t) d\omega$$

$$= \frac{1}{2\pi} \int_{\omega_{min}}^{\omega_{max}} \sum_{i=1}^{N} \Gamma_i \exp j\left(-\frac{2z_i\sqrt{\varepsilon_r}}{c}\omega \right) \exp(j\omega t) d\omega$$

$$= \sum_{i=1}^{N} \Gamma_i \sin c\left[(\omega_{max} - \omega_{min})(t - \tau_i) \right]$$

Where $\tau_i = \frac{2z_i\sqrt{\varepsilon_r}}{c}$ is the propagation delay of the i-th reflector. The above equation shows that because of the limited bandwidth, the impulse response is a series of sinc functions. The peak intensity of each sinc function represents the reflection coefficient of the corresponding reflector. The limited bandwidth ($\omega_{max} - \omega_{min}$) also indicates that the sinc function could overlap with adjacent signal if the reflectors are very close, and the overlap happens when the distance between two adjacent reflectors is less than $\frac{c}{2\sqrt{\varepsilon_r}(\omega_{max} - \omega_{min})}$, which indicates the spatial resolution of the sensing system. To

increase the spatial resolution, we should increase the bandwidth so that the pulse width of the sinc function can be narrower.

To reconstruct the interferogram of arbitrary two adjacent reflectors, a gating function is needed. Let us assume that the gating function is $g(t)$. After the gating, the time domain impulse response is now $h(t)g(t)$. The gated signal is then converted to frequency domain by Fourier transform to reconstruct the spectrum. The reconstructed spectrum can be written as

$$H_G(\omega) = H(\omega) * \left[G(\omega) \exp(-j\omega\tau_o) \right]$$

Where $G(\omega)$ is the inverse Fourier transform of the gating function $g(t)$, and τ_o is the time delay of the gatiing function. The above equation clearly shows that the reconstructed microwave spectrum is the convolution of the signal $H(\omega)$ and the shifted gating function $G(\omega) \exp(-j\omega\tau_o)$.

The above method can be illustrated in the following experiment example. The data is from a distributed strain data experiment that is a part of the 3D beam shape sensor experiment result explained later in Chapter 6.

In the experiment, the frequency response of the system is obtained from a VNA. The VNA sends out the linearly swept frequency microwave signal, and measures the reflected or transmitted magnitude and phase of the input signal at the same swept frequency within the intermediate frequency bandwidth (IFBW). The measurement target is a cable sensor with 10 reflectors on them, with about 10 cm distance between each adjacent reflector. Figure 2.6 shows the signal processing method from the VNA data to

the interferogram of a selected pair of reflectors. Figure 2.6(a) and 2.6(b) show the amplitude and phase of the reflection signal. In the measurement, the sampling rate or total sampling points is 10001, and the swept frequency range is from 2 MHz to 6 GHz. Figure 2.6(b) only shows the frequency span from 2 MHz to 2 GHz, because the spectrum is basically periodic, and a smaller span can provide a better view of the curve. An inverse complex Fourier transform is applied to the signal to achieve the time domain reflection signal as shown in figure 2.6(c). The ten embedded reflectors can be clearly observed in this graph as ten peaks at reflection intensities about 0.015. The intensities of the last few reflectors are declining a little bit because the incident power become less as previous reflectors bounce back some power to the source. Suppose we are currently interested in the virtual Fabry-Perot cavity formed by the 5th and 6th reflector, a gating window (indicated by the red dotted lines in figure 2.6(c)) can be applied in the time domain that covers the two reflectors, while isolating out other signals. Zero padding is also added here to improve the frequency domain resolution. Fourier transform is applied on this gated data to reconstruct the interferogram of the virtual Fabry-Perot cavity as shown in figure 2.6(d). The free spectra range (FSR) is about 1 GHz, and the fringe visibility is about 17dB. When bending occurs on the beam, the strain on the selected cable section will cause the interferogram to move, and the strain can be calculated with $\varepsilon x=\Delta f/f$. Applying the gating window on other reflector pairs and repeating the same processing method, the strain data on all the sections can be obtained. In this experiment, $\omega\_max-\omega\_min$ is 6 GHz, $\sqrt{\epsilon_r}$ is about 1.5, so the spatial resolution is about 1.7 cm. In

applications where reflectors are closer, increasing of the sweeping frequency bandwidth

will be needed.

CHAPTER THREE

III.   THE FABRY-PEROT CAVITY BASED HIGH TEMPERTURE SENSOR ON

COMMERCIAL CDRAMIC COAXIAL CABLES

3.1 Introduction

CCFPI (coaxial cable Fabry-Perot interferometer) has been reported as a

temperature and strain sensor recently [8][9]. The advantage of CCFPI comparing to fiber

optic FPIs, which is CCFPI's counterpart in optical domain [10][11], is that coaxial

cables usually have larger dynamic range than fiber optic sensors [12]. It is also more

robust than optical fibers physically, and can hence endure harsher environments

[13][14]. It is also more cost effective, since CCFPI operates in microwave domain, while

fiber sensors involve optical sources, detectors and spectrum analyzers that are usually

more expensive.

However, traditional coaxial cables cannot stand high temperature. Most coaxial

cables (flexible, semi-flexible, semi-rigid cables) that have traditional dielectric insulators

between inner and outer conductors cannot operate over 200°C. The reason is that the

insulator is made of polymers (PTFE, PVC, polyethylene, etc), and they cannot withstand

high temperature. One special kind of coaxial cable is called ceramic coaxial cable,

which use ceramics as insulator. It is an ideal cable that a CCFPI higher temperature

sensor can be made from.

In this paper, we study the possibility of using this cable to fabricate a good high

temperature sensor. The way to create reflectors in the cable is to drill holes on the cable

in our lab. Here we will first study the relationship between hole drilling and reflection

intensity on different cables. Then, we will use the Fabry-Perot cavity that has been created on the cable to test its temperature response.

3.2 Creation of reflectors on coaxial cables

The impedance of a coaxial cable is determined by its geometric shape and material properties. For a ordinary coaxial cable, its characteristic impedance is

$$Z_0 = \sqrt{\frac{R + j\omega L}{G + j\omega C}}$$

For a lossless transmission line,

$$Z_0 = \sqrt{\frac{L}{C}} = \frac{1}{2\pi}\sqrt{\frac{\mu_0}{\varepsilon_0 \varepsilon_r}} \ln\left(\frac{D}{d}\right)$$

It depends on the outer and inner diameter, and the dielectric constant of the insulator. When a hole is drilled on the cable, the shape of the cable is changed, and the characteristic impedance becomes a different value. Let us say the new value is ZL, so the reflection at the point where the impedance change happens is

$$\Gamma = \frac{Z_L - Z_0}{Z_L + Z_0}$$

The deeper we drill, the more difference we have for the new impedance, and hence a larger reflection. An experiment is performed on a flexible cable, when we drilled four holes with different depth (2.8mm, 2.9mm, 3.5mm and 4.2mm) consecutively on the same cable. The time domain reflection is shown in Figure 3.1.
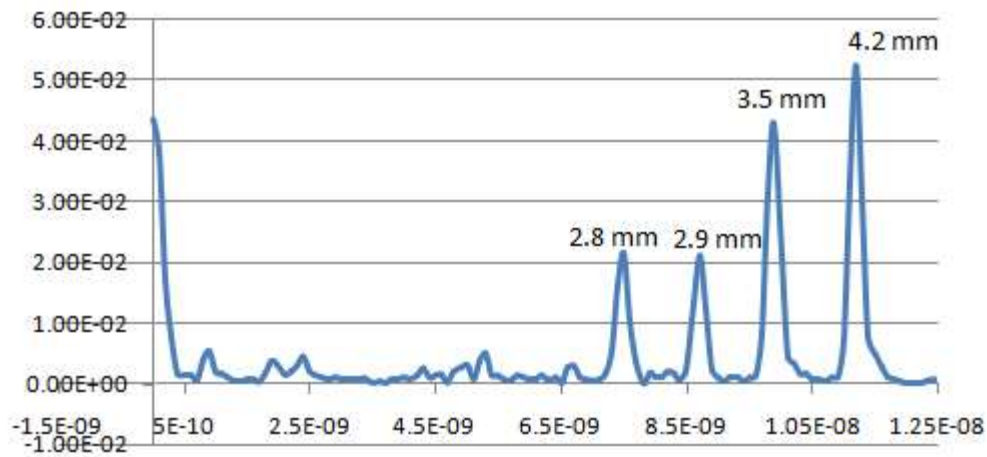
Figure 3.1. Reflection intensity VS hole drilling depth on a flexible cable.

It is clear that deeper holes produce bigger reflection. The only issue is that the 2.9mm hole is slightly less intense than the 2.8mm hole, that is because that, 1) The 2.9mm hole is farther than the 2.8 mm hole and there is loss when EM wave travel between them on the cable, and 2) the 2.8mm hole already reflected more than 2% of the power so there is less power arrive on the 2.9mm hole.

Another way to increase the intensity on the reflectors is to drill multiple holes at the same position of the reflector. In the next experiment, we drilled 4 sets of holes with 4 different depths (1.6 mm, 1.9mm, 2.1mm, 2.2mm), and in each set, we drilled four holes one after another in the sequence that is shown in Figure 3.2(a). The reflection intensity is recorded after each hole is drilled, and the result is shown in Figure 3.2(b).

(a)   (b)
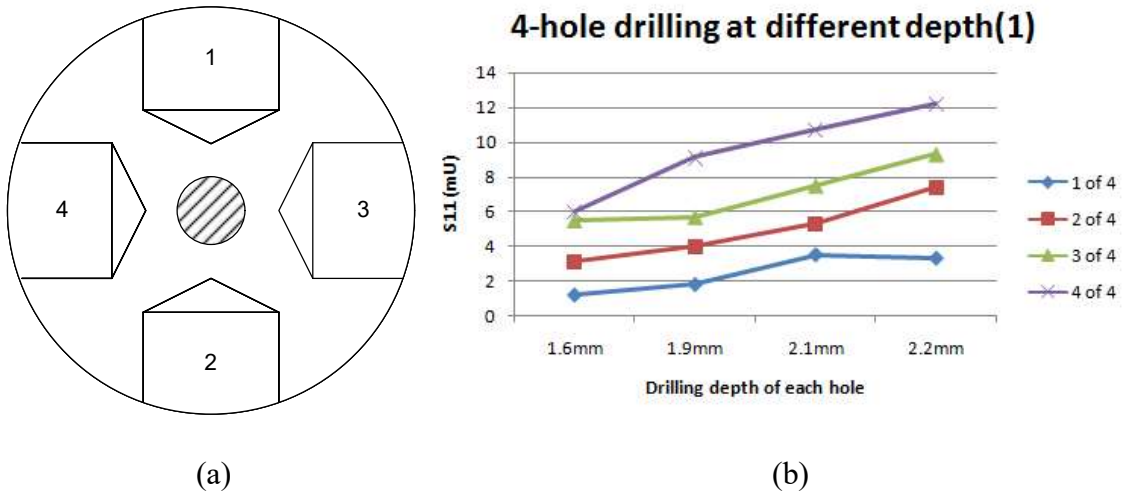
Figure 3.2. (a) Multi-hole drilling pattern, and (b) intensity of reflectors with different

depth and hole number.

From the result we can clearly see that drilling multiple holes at the same position

can increase the reflection intensity almost in proportion to the number of holes. For

example, comparing the intensity between four holes and one hole, there is a roughly 3 to

4 times difference for all the 4 depth in the experiment.

Multiple and deeper holes can produce big reflection. If it is still not enough, we

can fill the hole with some conductive material. Figure 3.3 shows the experiment result of

several holes with different depth filled with conductive material. The filling material is

liquid tape mixed with graphite powers, so it is easy to fill in. The result shows that this

method can increase the reflection intensity when the drilling depth passed a certain

threshold. Under the threshold (about 1.6mm), there is very little difference, but above

that threshold, the difference is significant.

| (a) | (b) |
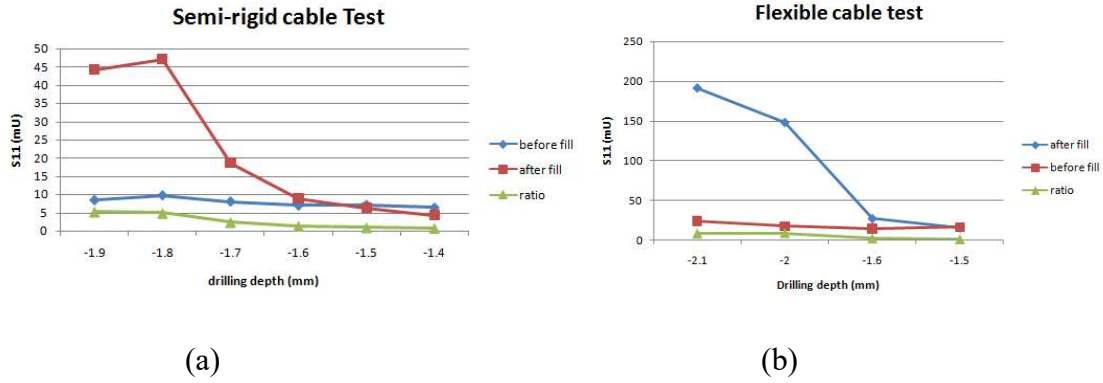
Figure 3.3. Reflection intensity before and after filled with conductive material.

For high temperature applications, we need to drill holes on ceramic cables to create reflections. Ceramic cable has a smaller diameter but large hardness, making it difficult to control the drilling depth. Simply drilling a hole will create reflection, but very small. Filled the hole with conductive material can increase the reflections a lot, so that we can have a good signal to noise ratio.

3.3 Temperature sensing using ceramic cable interferometer

After the two reflectors are fabricated on the ceramic cable, we can observe the two reflectors from time domain. But there are other reflection signals from the system, including connectors, terminators, and the small reflections from the ununiformed cable. The way to get rid of other reflections is to add a time domain gate on the signal, only covering the part where the two reflectors are located, and then transform the remaining signal back to frequency domain. A time domain signal after gating on two reflectors is shown in Figure 3.4. Ceramic cables have big non-uniformity along the cable, so we can

see the ripples and noises almost 1% high in S11 between the two reflectors. Outside the

two reflectors, the gate filters out the noises.
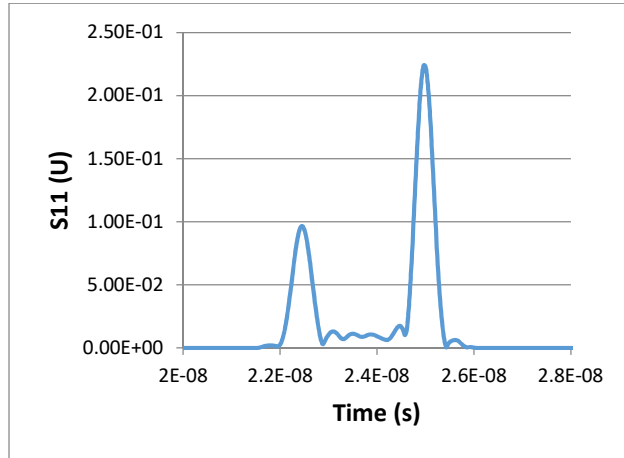
Figure 3.4. Time domain signal of the two reflectors after gating.

The temperature response of the two reflectors is then tested under high

temperature. The cable is put in a furnace which has its temperature risen from room

temperature to 800°C. The reflection intensity of the two reflectors are recorded and

shown in Figure 3.5.
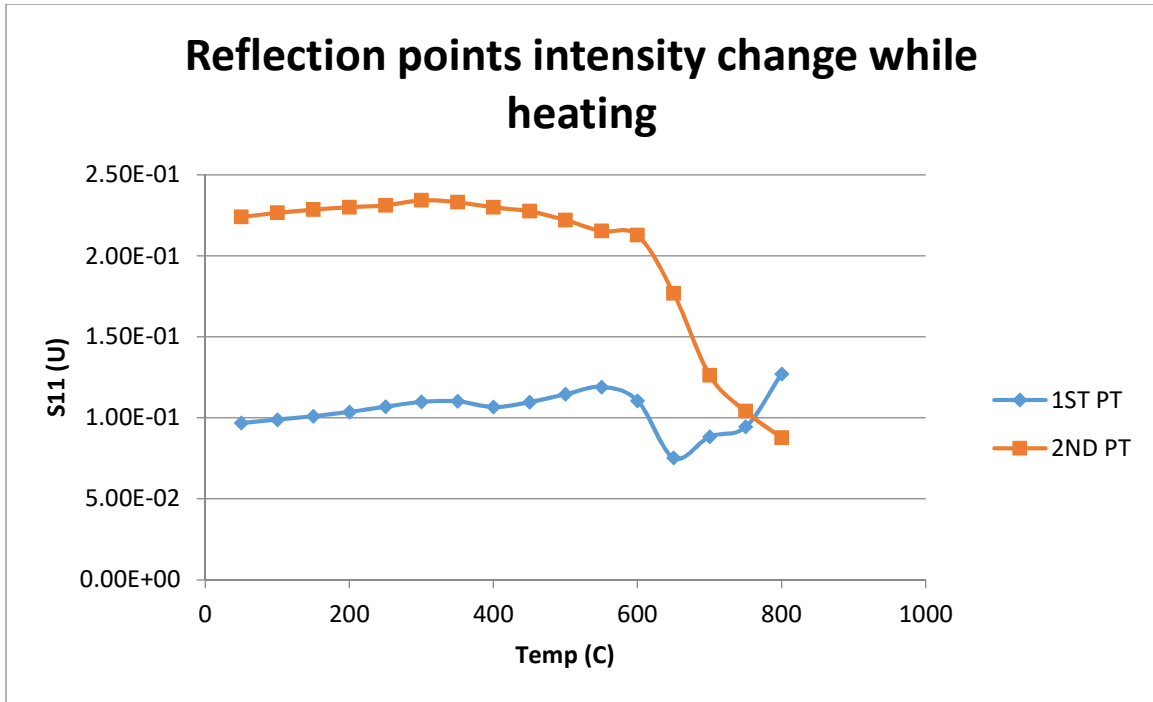
Figure 3.5. Reflection intensity change during heating process.

From the figure we can see that the reflection of both reflectors are stable until the temperature hit 600ºC. After that the reflection changed significantly in different trends. The change could be either the ceramic insulator or the filler inside the hole. This change will result in abnormal behavior of the interference pattern from the two reflectors.

Figure 3.6 shows the change of the mass center of the interference pattern when temperature rises from 50ºC to 800ºC. When the temperature is not very high, from 50ºC to 250ºC, the mass center of the interference pattern almost kept the same. Above 250ºC and lower than 600ºC, the mass center decreases linearly in frequency as the temperature rises. Above 600ºC, the mass center rises abruptly till 700ºC, and then drops. The abnormal part above 600ºC matches the sudden change of the reflection intensity at

600ºC. From this we can conclude that this ceramic cable FPI sensor cannot work over

600ºC.
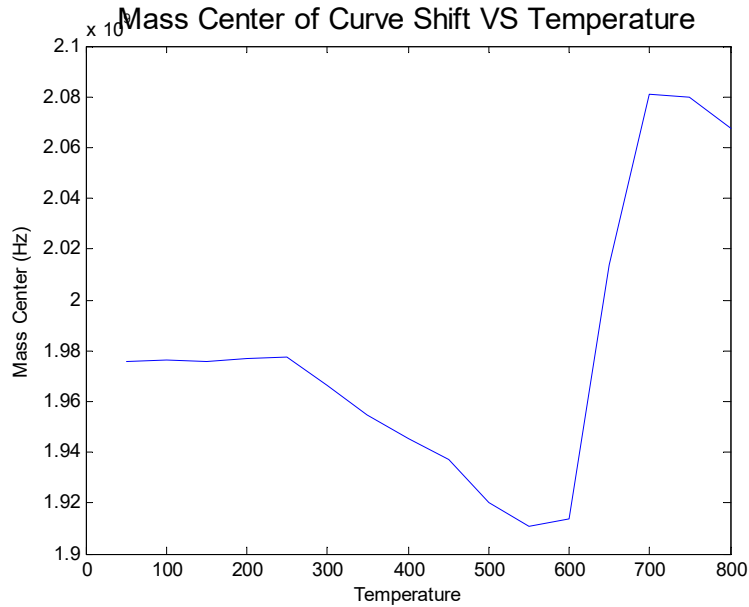
Figure 3.6. Interference pattern mass center change when temperature changes from 50ºC

to 800ºC.

To accurately calibrate this sensor, we pick the lowest point at around 3G Hz of

the interference pattern to study its temperature behavior. We already know that the

sensor does not work above 600ºC, so the data only goes up to 550ºC. When the

temperature is under 550ºC, the change of the interference pattern is shown in Figure 3.7.

The spectrum moves up and left slowly with the rising temperature. At the first 200ºC,

the change is small. After that, the change is relatively big.
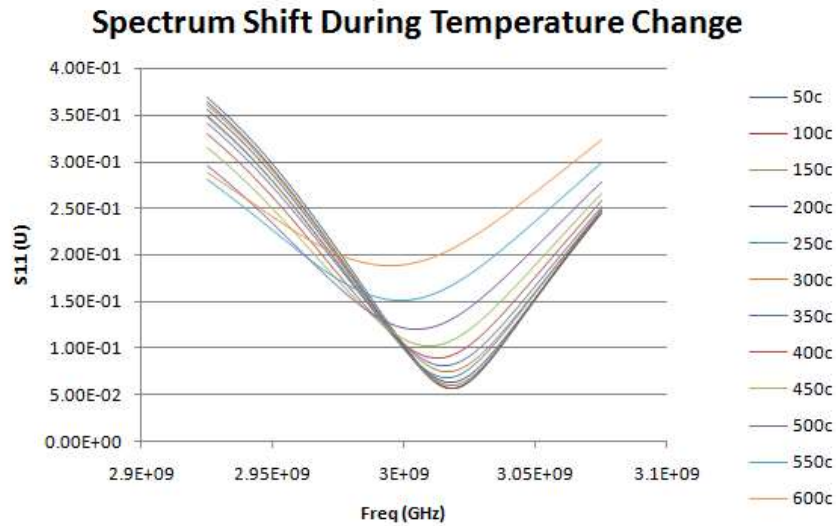
Figure 3.7. Temperature response of the interference pattern near 3G Hz when temperature changes from 50ºC to 550ºC.

Figure 3.8 shows the frequency change of the lowest point around 3G Hz of the interference pattern when temperature change from 50ºC to 550ºC. The trend is fit into a cubic curve as shown in the figure. Again we can see the small response below 200ºC and large response above 250ºC.
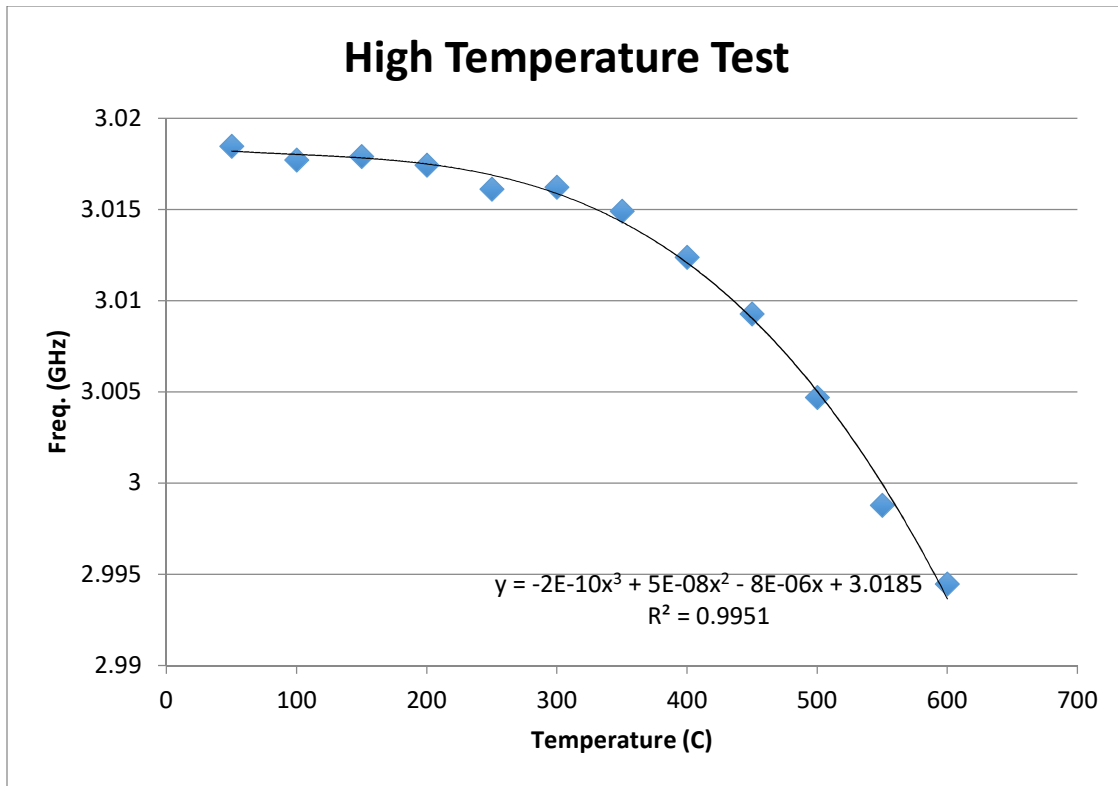
Figure 3.8. Frequency change of the lowest point around 3G Hz of the interference pattern when temperature change from 50°C to 550°C.

3.4 Discussion and conclusion

There are two factors that account for the temperature response of this sensor. The first one is the thermal expansion, which elongate the material while heating. The second one is the dielectric constant change with temperature, which change the dielectric constant of the insulator material and hence change the effective length of the cable section between the two reflectors. These two factors have opposite influence, so they are competing with each other when temperature changes. At low temperature, the two factors have similar influence, so the temperature response is small. But at high

temperature, one of them becomes dominant, so the temperature response becomes very obvious. We have no information on the insulator material, so there is no quantitative way to know the exact property of this cable. In the future, we can use this small temperature response property to make this cable into a temperature insensitive sensor to eliminate crosstalk with other physical quantities, such as strain sensing. Another way is to fabricate our own coaxial cable where we can choose the insulators, to exploit the specific properties of the materials for further applications, which will be discussed in the next chapter.

CHAPTER FOUR

IV.   METAL CERAMIC COAXIAL CABLE HIGH TEMPERTURE SENSOR

4.1 Cable material and dimension

The Fabry-Perot sensor consists of two reflectors, which are created by impedance mismatch along the coaxial cable. From transmission line theory, the characteristic impedance of a coaxial cable can be calculated by The Fabry-Perot sensor consists of two reflectors, which are created by impedance mismatch along the coaxial cable. From transmission line theory, the characteristic impedance of a coaxial cable can be calculated by $Z_0 = \sqrt{\frac{R+j\omega L}{G+j\omega C}}$, where R is the series resistance, L is the series inductance, G is the shunt conductance, and C is the shunt capacitance. They are distributed parameters of a transmission line. For a coaxial cable with outer diameter D, inner diameter d, permittivity ε and permeability μ and conductivity σ of the dielectric material, permeability μ_c and conductivity σ_c of the conductor, the parameters are given by , where R is the series resistance, L is the series inductance, G is the shunt conductance, and C is the shunt capacitance. They are distributed parameters of a transmission line. For a coaxial cable with outer diameter D, inner diameter d, permittivity ε and permeability μand conductivity σ of the dielectric material, permeability μ_c and conductivity σ_c of the conductor, the parameters are given by

$$R = \frac{1}{2\pi}\sqrt{\frac{\pi f \mu_c}{\sigma_c}}\left(\frac{1}{a}+\frac{1}{b}\right)$$

$$G = \frac{2\pi\sigma}{\ln(\frac{D}{d})}$$

$$L = \frac{\mu}{2\pi}\ln\left(\frac{D}{d}\right)$$

$$C = \frac{2\pi\varepsilon}{\ln(\frac{D}{d})}$$

Ideally, the conductivity of the conductor σ_c is a very big number, and the conductivity of the dielectric σ is very close to 0. Thus R and G are negligible. In this case, the characteristic impedance can be calculated by $Z_0 = \sqrt{\frac{L}{C}} = \frac{1}{2\pi}\sqrt{\frac{\mu_0}{\varepsilon_0\varepsilon_r}}\ln(\frac{D}{d})$.

When using a lossy material as the dielectric, or using a conductor with some resistance, the original equation $Z_0 = \sqrt{\frac{R+j\omega L}{G+j\omega C}}$ should be used.

When we create an interface in the cable by a sudden change of the material or dimension, the characteristic impedance will change. Assume that the new characteristic impedance is Z_L, the reflection at the interface is given by $\Gamma = \frac{Z_L-Z_0}{Z_L+Z_0}$.

The equations above give the theoretic methods to evaluate the impedance of the cable. However, in practice, the coaxial cable that we make will have some error, such as air gap between outer conductor and dielectric, air gap between inner conductor and dielectric, position error of the inner conductor, or non-circular shape of the inner and outer conductor. It is worthwhile to know how much the impedance deviation is when there is a small amount of error.

It is very difficult to calculate the impedance analytically when we have these errors. In this case, numerical method is desirable. Here we can use a FEM software, COMSOL multiphysics, to calculate the impedance. The impedance is given by $Z_0 = \frac{V}{I}$, where the voltage can be evaluated by lineally integrate the electric field between the two conductors as $V = V_i - V_o = -\int_{r_o}^{r_i} E \cdot dr$, while the current is evaluated by lineally integrate the magnetic field along any closed contour C around the inner conductor as $I = \oint_C H \cdot dr$. These integrations are shown in Figure 4.1(a).

(a)   (b)   (c)
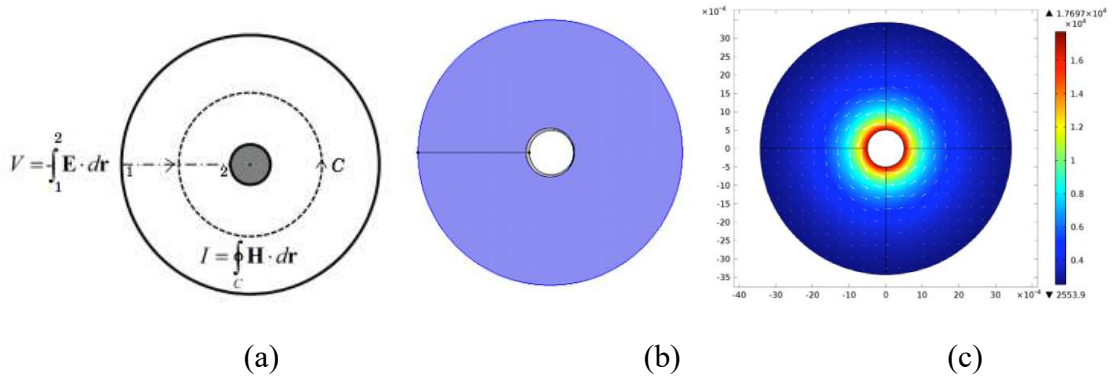
Figure 4.1. Numeric simulation of the cable cross section. (a) How the integrations are performed to evaluated V and I(from COMSOL model gallery, Model ID12351), (b) a geometric model of the cable cross section when there is inner air gap and position error of the inner conductor, (c) a graph of a typical FEM simulation result.

For a cable with 0.5mm inner conductor radius, 3mm outer conductor radius and dielectric constant of 9, several errors caused by air gaps are simulated cable when there is inner, outer or off-center gap, and the results are shown in Table 4.1. The unit is in Ohm.

Table 4.1. Impedance of the cable with different gap positions.

gapsize (um)	inner gap	off center gap	outer gap
0	35.8703	35.8703	35.8703
1	36.0231	36.0384	N/A
5	36.6495	36.6491	35.9476
10	37.4077	37.3807	36.0853
50	42.7641	42.3611	37.1736
100	48.1992	47.2792	38.5048

The results show that of all kinds of gaps, inner gaps induce most significant impedance error. Also, if the gap size is under 10um, the impedance error is relatively small.

4.2 Thin disk reflectors for FPI sensors

Fabry-Perot interferometer is widely used in optical measurement where the F-P cavity consists of two reflecting interfaces. Our sensor is made by migrating this structure to coaxial cables. In the MCCC-FPI structure, the reflector is created by implanting a small disc that has a different dielectric constant into the insulation layer of the cable. This indicates a fact that instead of two reflections that occur in optical FPI, a coaxial cable FPI that realized by our method will have four reflection interfaces, as shown in Figure 4.2.
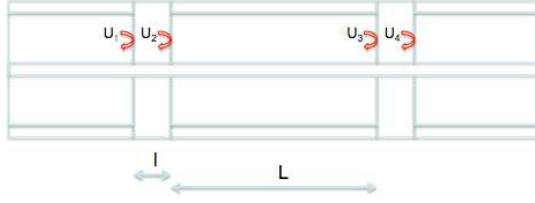
Figure 4.2. Reflection scheme of the MCCC-FPI sensor.

Assume the thickness of the reflector disc is l, and the distance between the two reflectors is L. The time for the EM wave to travel through the disc (distance l) is Δt, and the time for the EM wave to travel from one disc to the next one (distance l+L) is ΔT. The reflection coefficient at each interface is $\Gamma(f)$, and the voltage that arrive at the front interface of the first reflector disc is U_0. The reflected waves are

$$U_1 = U_0\Gamma(f)e^{j2\pi ft}$$

$$U_2 = -U_0\Gamma(f)[1 - \Gamma(f)]e^{j2\pi f(t+\Delta t)}$$

$$U_3 = U_0 e^{-2\alpha L}[1 - 2\Gamma(f)]\Gamma(f)e^{j2\pi f(t+\Delta T)}$$

$$U_4 = U_0 e^{-2\alpha L}[1 - 2\Gamma(f)]\Gamma(f)[1 - \Gamma(f)]e^{j2\pi f(t+\Delta T+\Delta t)}$$

Assume $\Gamma(f) \ll 1$, $e^{-2\alpha L} \approx 1$

The total wave is the sum of all them

$$U = U_1 + U_2 + U_3 + U_4 \approx U_0\Gamma(f)e^{j2\pi ft}(1 + e^{j2\pi\Delta T})(1 - e^{j2\pi\Delta t})$$

If $\Gamma(f)$ is a constant, omitting the time harmonic term $e^{j2\pi ft}$, U is actually a fast oscillating sinusoidal wave (period determined by Δt) modulated by an envelope sinusoidal wave (period determined by ΔT). Figure 4.3 shows the experiment and simulation spectrum of two MCCC-FPI sensors.

(a)   (b)

(c)   (d)
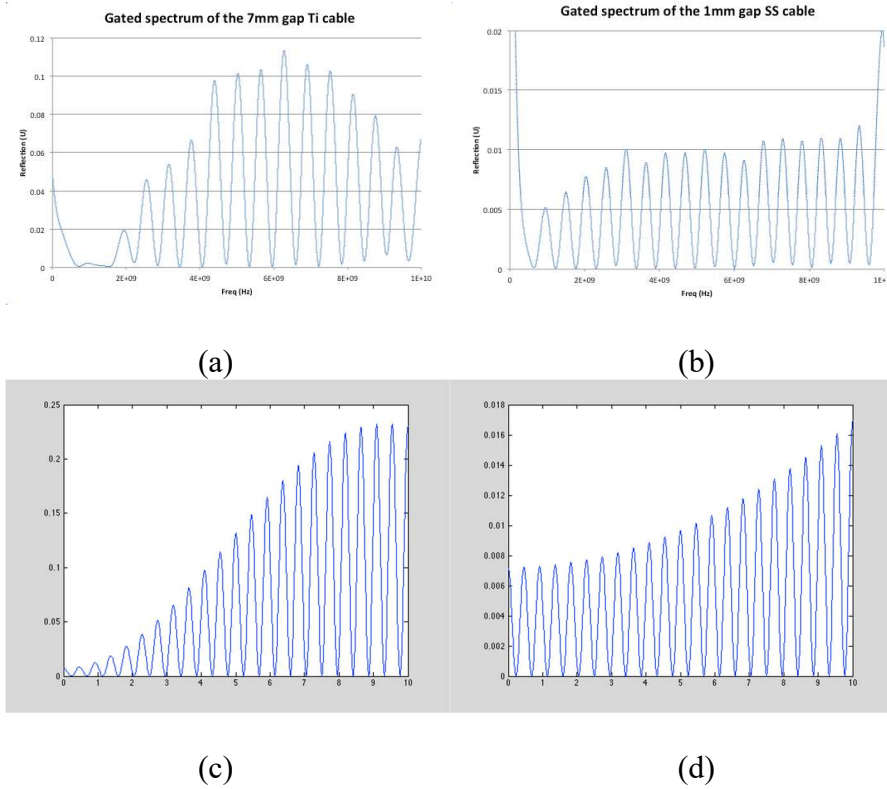
Figure 4.3. Measurement and simulation spectrum of CC-FPI sensor. (a) and(c) Experimental and simulation spectrum of a FPI sensors with a 7mm air gap as reflector in a MCCC cable. (b) and (d) Experiment and simulation spectrum of a FPI sensors with a 1mm air gap as reflector in a MCCC cable.

The simulation result is a little different from that of the experiment result. This is caused by the fact that some of the assumptions we made does not hold in practice. For example, assuming the reflection at the interfaces $\Gamma(f) \ll 1$ makes it much easier to deduce the formula, but this relation does not hold in out experiment. We need to improve this mathematic model in our future work to better describe the FPI sensor.

By choosing the disc thickness l and cavity length L, we can determine the FSR of the

interferogram as well as the envelope period. To achieve the best fringe visibility, the two

disc thicknesses can be adjusted to have the same reflection level in time domain.

To precisely control the reflection intensity of the reflectors in the cable is very important

for distributed applications. Too low reflection leads to low signal to noise ratio and bad

measurement result, but too high reflection will waste too much energy on single

reflectors, hence not many reflectors can be seen during interrogation. Here we will study

the relationship between the reflection intensity and the thickness of the disks. To

simplify the experiment setup, the disk is actually an air gap so that we can easily vary

the 'thickness' of it. The conclusion we draw from this study will also apply to other

materials as long as we replace the refractive index of air (1) with the refractive index of

that particular disk material.

We start from calculating the transmittance of the air gap. It is actually a Fabry-

Perot cavity that has two interfaces. The transmittance of this cavity is given by the well-

known Airy function:

$$T(\delta) = \frac{1}{1 + \left[\frac{4r^2}{(1 - r^2)^2}\right]sin^2(\frac{\delta}{2})}$$

T is the transmittance of the Fabry-Perot cavity, r is the reflectance of the interface, and δ

is the phase difference between the two reflections on the cavity ends. δ is a function of

cavity length L and wave frequency f. It can be written as

$$\delta(f,L) = \frac{\pi L f}{nc}$$

Where c is the vacuum light speed and n is the refractive index of the medium, which is 1 when the cavity is filled with air.

If the VNA calculates the reflection in the time domain by averaging the reflectance over the whole frequency span, the reflection can be represented by

$$R(L) = \frac{1}{\Delta\varphi} \int_{\varphi_0}^{\varphi_1} T(\delta(f,L)) df$$

Where φ_0 and φ_1 are the start and stop frequency that we set when doing the measurement. $\Delta\varphi = \varphi_0 - \varphi_1$ is the frequency difference of the span.

Assume that the single interface reflection is r=0.3 according to previous experiment results, and the frequency span is 0 to 10G, the reflection of the air gap with length L is simulated using a Matlab program. The simulation result is shown in Figure 4.4.
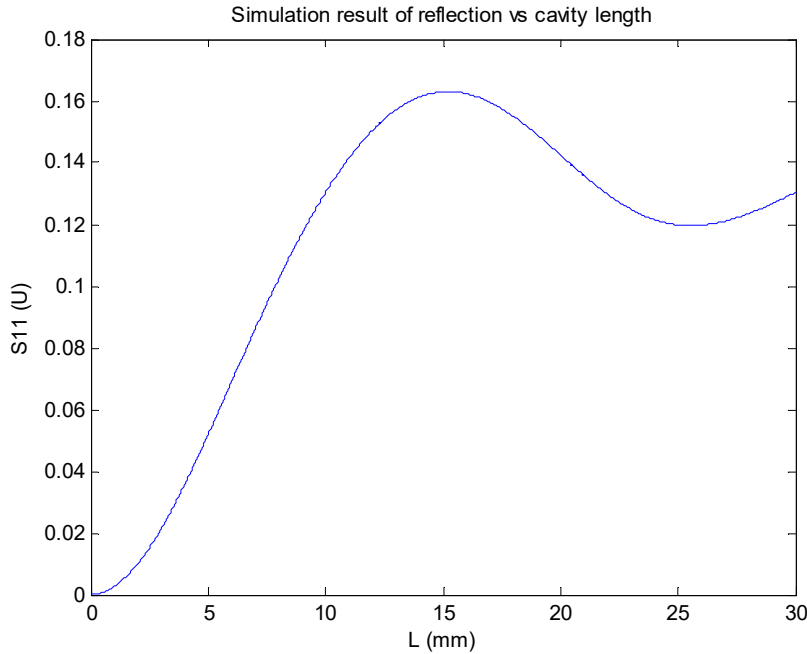
Figure 4.4. Simulation result of the reflection intensity change with cavity length.

To verify this simulation, an experiment is carried out to measure the total reflection of

an air gap between two alumina tubes with different gap sizes.
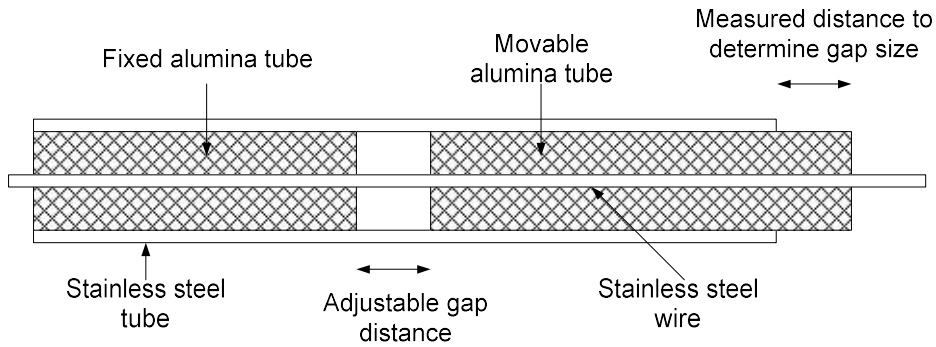
Figure 4.5. Cable structure for the experiment of reflection intensity measurement.

As shown in Figure 4.5, the air gap size is adjusted by moving one of the alumina tubes,

and the distance is calculated by measuring the position of the end of the moving alumina

tube. The size of the air gap and the resulted reflection intensity is shown in Figure 4.6.
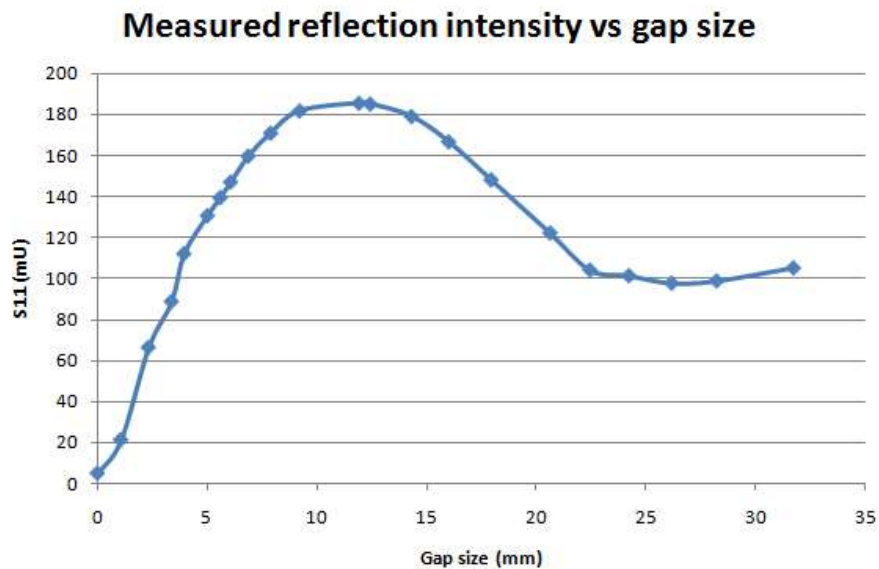
Figure 4.6. Reflection intensity as a function of cavity length, experiment result.

Comparing the measurement result and simulation, we can see that they have similar trend and intensity distribution as gap size increases. However, in the simulation, the biggest reflection occurs at about 14.5mm, while in experiment the biggest reflection occurs at about 12.5mm. Also, in experiment, after the highest point, the reflection goes down to about 0.56 of that peak value, while in simulation, it is 0.75. The reason of the difference is probably as follows.

First, the lead in cable, the connectors and the sensor itself have transmission loss over the frequency range that we used. At low frequency, the loss is small, but at high frequency it is increasing significantly. In the simulation, we are not taking into account the transmission loss, especially at high frequency. This is the main reason that the simulation is different from experiment result.

Secondly, the VNA has its own algorism to transform frequency domain data to time domain data. In our simulation, we are assuming that each frequency contributes equally to time domain, meaning that we are using a square window for the transform, but the VNA clearly is using some other kind of window function that we have no way to know exactly. That also account for the simulation error.

4.3 Attenuation of the cable

Attenuation is an important parameter for the coaxial cable that we made in the lab. Low attenuation is desirable as we want good signal to noise ratio even after long

transmission and reflection on multiple reflectors. When testing cables with multiple reflectors, it can be observed that the time domain reflection intensities of the reflectors are dropping one by one as they are further away from the testing port. Two reasons will cause this effect to happen, one is that the cable have inherent losses, and the other one is that the previous reflectors have consumed some power. The first reason is dominating, especially when the reflectors are created so that they are very weak, such as 1% to 3%. To address the problem, we need to take a look at the losses on the cable.

The losses on the cable can be divided into two main categories; the loss in dielectric, and the conduction loss. We will first look at the dielectric loss, then the conduction loss.

To test the dielectric loss, attenuation and time-domain reflection are measured for two of the MCCC cables. The first Cable is a Ti-Teflon-Air cable, which has titanium as outer and inner conductor, Teflon disks as reflectors, and the dielectric material is air. The second cable is a Ti-Teflon-Alumina cable, which has titanium as outer and inner conductor, Teflon disks as reflectors and the dielectric material is alumina.

For cable 1, The attenuation (loss) is measured using S21 of the VNA. A reference was first measured by connecting the lead in semi-rigid coaxial cable directly between the two ports of VNA. Cable 1 was then inserted between the lead in cable and the port and the result is calculated and shown in Figure 4.7 after subtracting the reference.
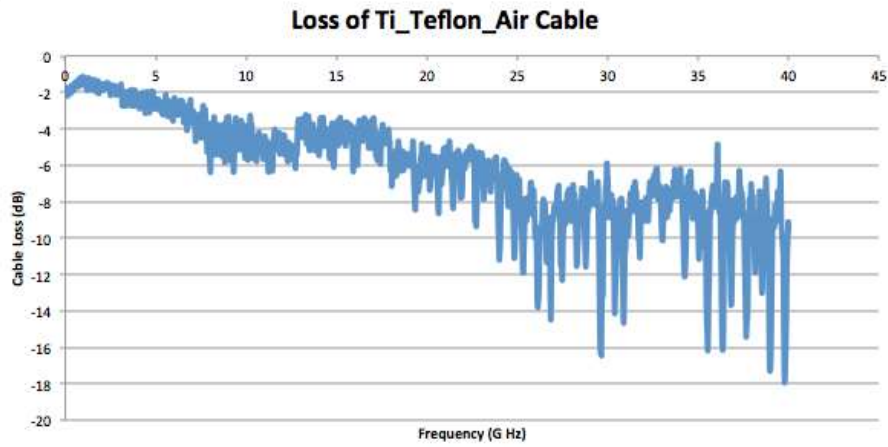
Figure 4.7. Loss of Cable 1.

The result shows that the loss increases slowly with frequency. It is about 2dB at the beginning, 3dB at 5G, 4.5dB at 10G and about 6dB at 20G. After 20G the curve is not stable.

It is worth noting that the loss includes both the cable and the two connectors. The real attenuation of the cable should be this curve minus the loss at the two connectors.
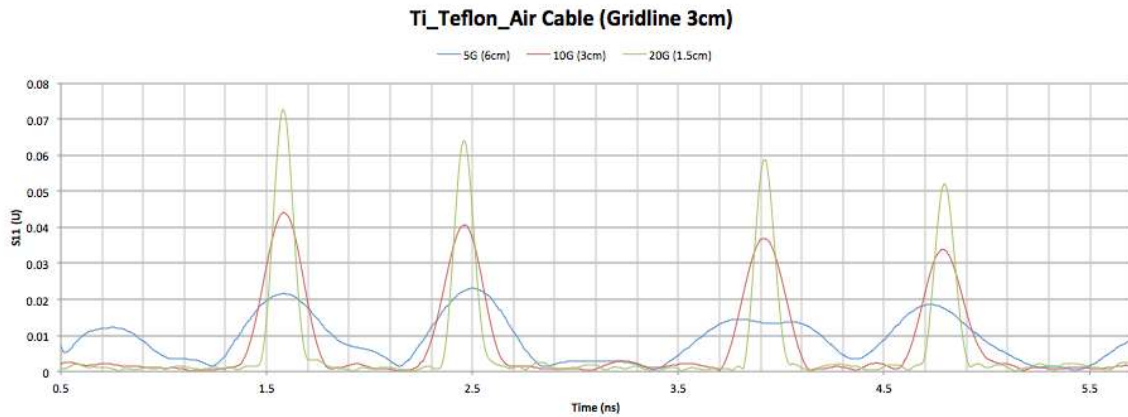
Figure 4.8. Time Domain Reflection of Cable 1.

47

The time domain reflection signal is shown in Figure 4.8. Three curves are shown with stop frequency at 5G, 10G and 20G. We can achieve higher spatial resolution with higher frequency, but the tradeoff is higher attenuation as shown in Figure 4.8. The resolution is 6cm for 5G stop frequency, while 3cm for 10G and 1.5cm for 20G.

The Teflon reflectors are separated by 21.8/13/21/8/13/21.8 cm. It is obvious that the blue curve with 6cm resolution (5G frequency) is not acceptable, as it can hardly separate the signals, especially for the reflectors 13 cm apart. From the green curve with 1.5cm resolution (20G frequency) we can see the reflection signal drops a little from 7% to 5% due to loss along the cable, but acceptable. The noise level between the signals is very low, less than 0.2%.

For Cable 2, the loss curve of Cable 2 is shown in Figure 4.9. It decreases from 0 dB to -50dB almost linearly from 0 to 40G. There is also a dip at 20G and the reason is yet to be studied.

This loss is significantly larger than Cable 1. It already has a loss of -10dB at 5G for this 1-meter long cable. The reason of this high loss maybe due to: 1, The absorption of microwave of Alumina material (not likely); 2, The non-uniformity of the Alumina in the cable; 3, The grain size of the Alumina is similar to the wavelength, which increased the scattering.
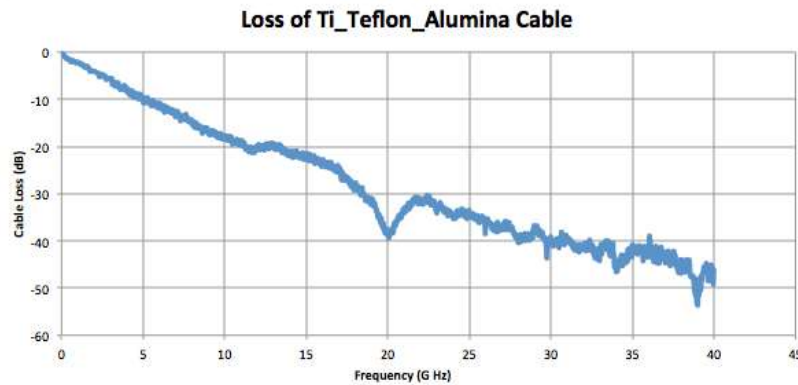
Figure 4.9. Loss of Cable 2.

The time domain reflection signal is shown in Figure 4.10. From the red curve (10G) and green curve (20G) we can see that the signals of the 4 reflectors are dropping very fast due to the loss at high frequency. Also, we can observe noises with 1% to 1.5% reflection (green curve between 0.6 to 1.6ns). This may be due to the non-uniform distribution of Alumina in the cable. The loss of the blue curve (5G) is acceptable, but the resolution is not sufficient as discussed before.
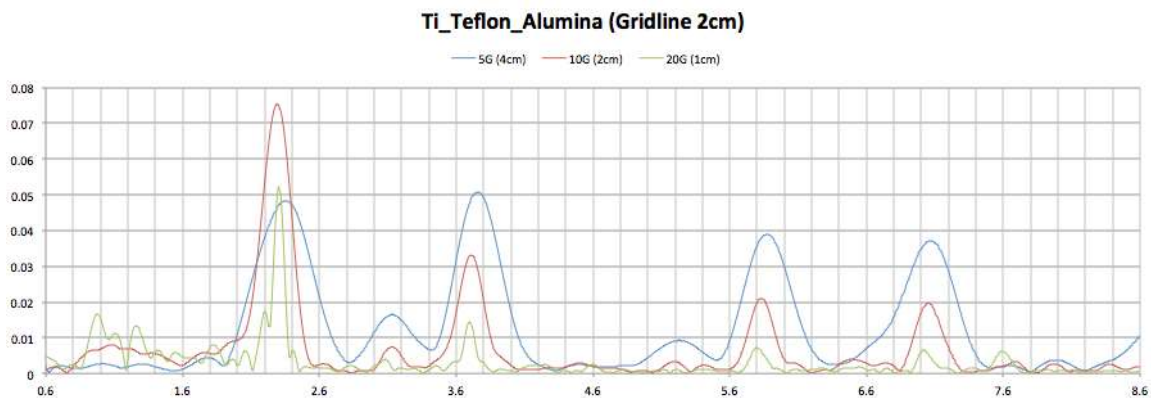
Figure 4.10. Time Domain Reflection of Cable 2.

49

From the above experiment, we can see that the loss depends on the dielectric material, as well as the interrogating frequency. Air cavity have low loss, but dielectric material with grain size have huge loss. When there is discontinuity in the dielectric material, scattering effect will also cause a lot of loss. But we do have the interrogating frequency under control. To lower the loss, highly recommended that lower frequency should be used.

The other part that induces loss is conducting loss, which is mainly determined by the conducting material of the cable. A higher conductivity of the material, hence lower resistivity, will cause fewer conduction loss. Table 4.2 shows the conductivity and resistivity of several kinds of metal materials that we plan to try on the cables we make.

Table 4.2. Conductivity and resistivity of several metal materials.

	Conductivity (10E6, S/m)	Resistivity (10E-8, Ohm/m)
Copper	58.5	1.7
Titinium	2.4	41.7
SS 316L	1.32	76
SS 304	1.37	73
SS 310	1.28	78

We tested the three metal materials in the cable by making three cables, with copper, titanium and stainless steel as the conductor. All three cables have no filling

materials. The transmission loss of them are tested by measuring the S21 on the VNA. The result is shown in Figure 4.11.
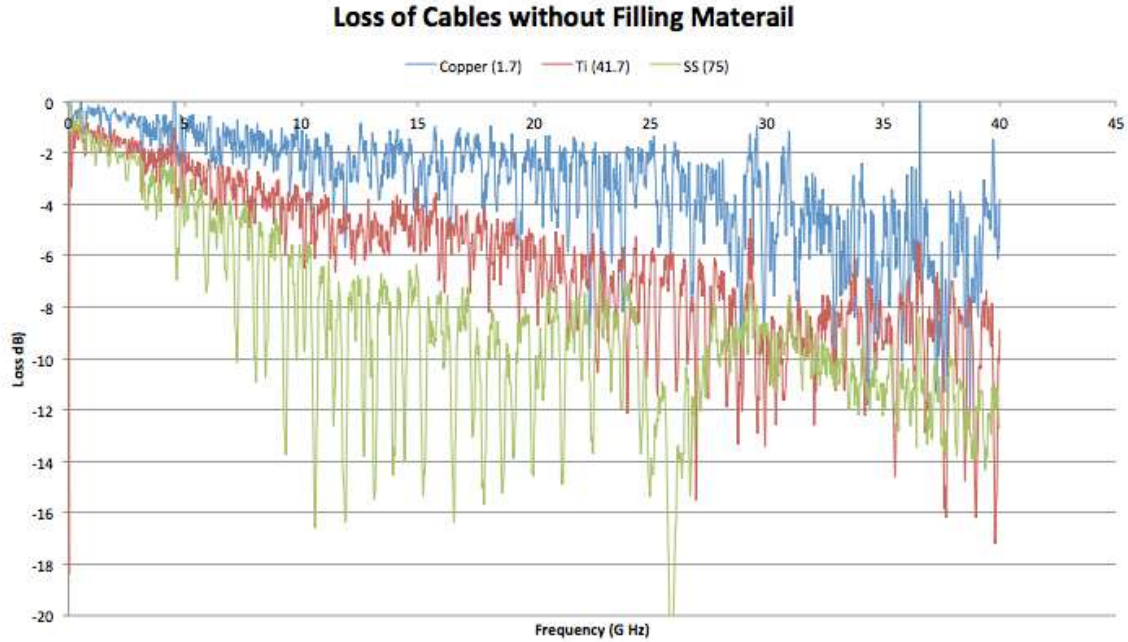
Figure 4.11. Loss of copper, titanium and stainless steel made cables.

The result matches well with the theory and it means that metal with good conductivity such as copper have lower loss.

The above experiment can also be explained in theory. Theoretically, the attenuation constant of a cable can be expressed as

$$\alpha = \frac{1}{2R_0}(R + G|Z_0|^2) \ \text{(Np/m)}$$

Where R_0 is the real part of the characteristic impedance of the transmission line. For

coaxial cable, R and G can be represented by $R = \frac{\sqrt{f\mu_c}}{\sqrt{\pi\sigma_c}}(\frac{1}{a} + \frac{1}{b})$ and $G = \frac{2\pi}{\ln(\frac{b}{a})}$, Where a

and b are the diameter of the inner and outer conductor of the cable, σ is the equivalent

conductivity of the lossy dielectric, which can also be written as

$$\sigma = \omega\epsilon''$$

Where ϵ'' is the imaginary part of the complex permittivity of the dielectric material.

Both R and G will increase with the microwave frequency, meaning that at higher

frequency, the cable will have a bigger loss. From the equation we can infer that for the

conducting material, higher conductivity means lower loss on the cable. For the dielectric

material, higher resistivity means lower attenuation.

4.4 FPIs with disk reflectors for high temperature sensing

The schematic of the metal ceramic coaxial cable with thin disk reflectors is

shown in Figure 4.12 below. The metal tube and metal wire are acting as the outer and

inner conductor of the cable. The ceramic tube is the dielectric material in the cable. Thin

disc reflectors are fitted in between the ceramic tubes. The thin disks can be made of

different materials and sizes to achieve different reflection intensities.
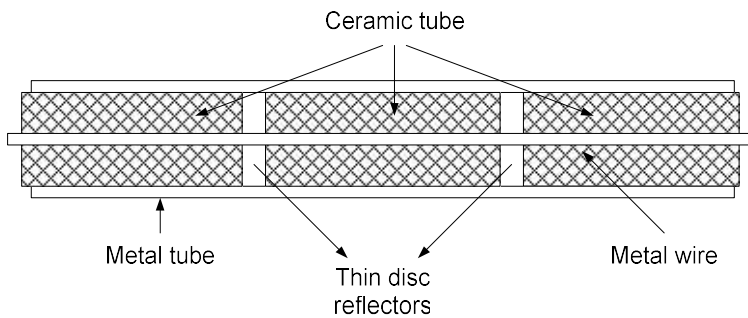
Figure 4.12. Schematic of the metal ceramic coaxial cable with thin disk reflectors.

Figure 4.13 shows the schematic diagram of the apparatus for high temperature

MCCC-FPI sensor test. The CC-FPI is connected to a VNA via a lead in RG58 cable.

The VNA is connected to a computer for data acquisition and analysis. The CC-FPI cable

is put in a tube furnace and the temperature of the furnace is programed to rise from

100°C to 500C, then drop down to 100°C. Every 50°C, the temperature is kept still for a

few minutes, and the cable data is recorded during the time.
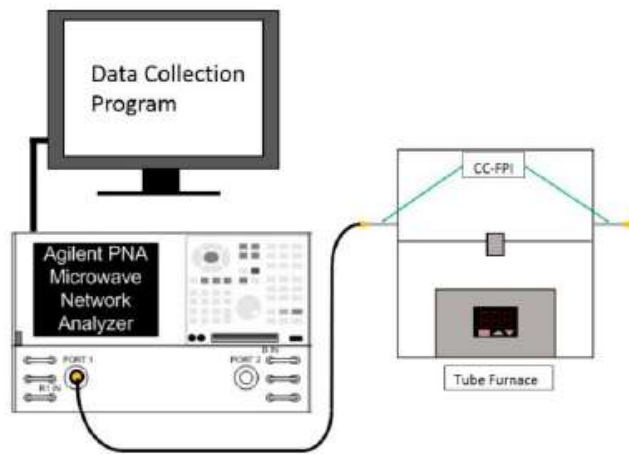
Figure 4.13. Schematic diagram of the apparatus for high temperature MCCC-FPI sensor

test.

Four different materials are made into four thin disk reflectors and tested with the

schematic shown above. These disks are 1mm thick Macor disks, 1mm thick ZTA disks,

1mm Sapphire disk, and 2mm thick Quartz disks. The dielectric constants of Macor,

ZTA, Sapphire and Quartz are 5.7, 12.4, 10 and 3.5 respectively. The test result is shown

in Figure 4.14 to Figure 4.16 below.
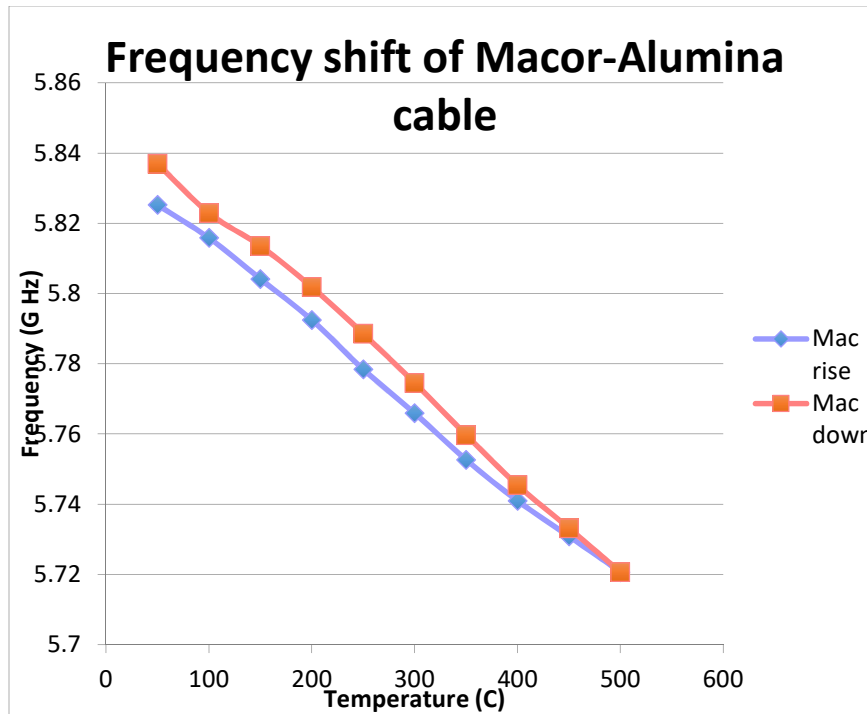
Figure 4.14. Frequency shift of Macor-Alumina cable during test.
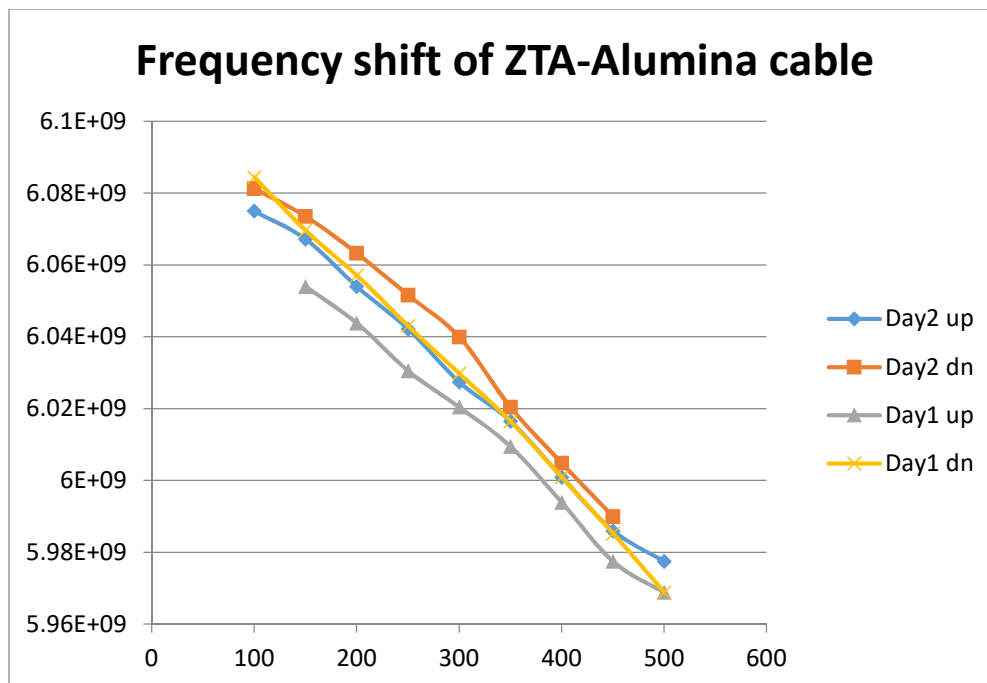
Figure 4.15. Frequency shift of Sapphire-Alumina cable during test.
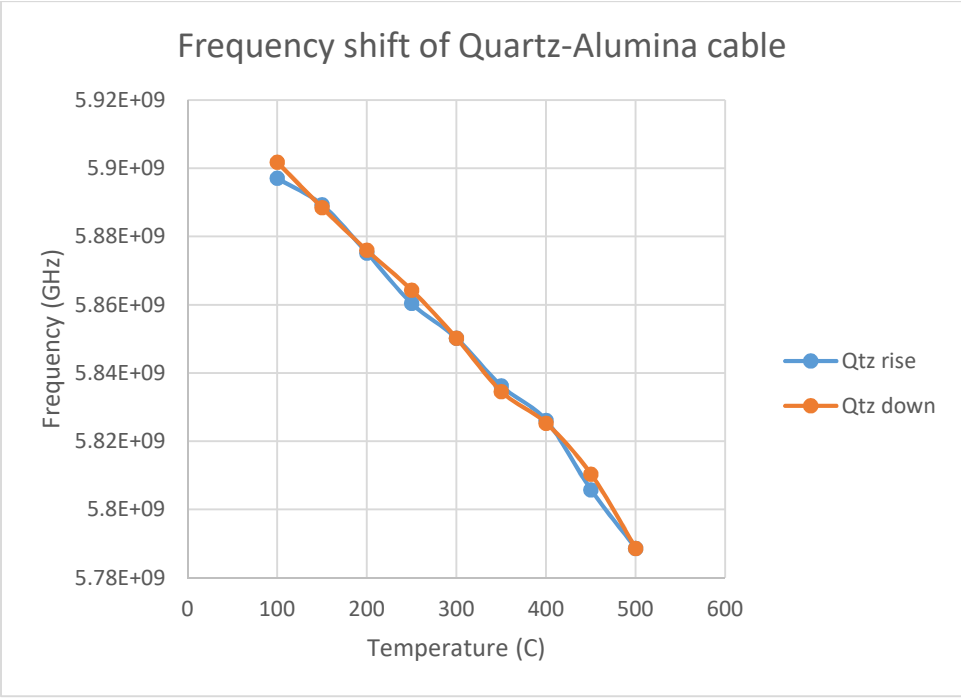
Figure 4.16. Frequency shift of Quartz-Alumina cable during test.

Table 4.3 summarizes the frequency shift data of the experiments. In each experiment, the frequency dip at around 6G Hz is picked, as this dip has a relatively better fringe visibility. Based on the frequency shift, the sensitivities of the sensors are calculated. To study the sensor structure difference before and after the heating/cooling cycle, the frequency difference at the starting (also the ending) temperature is also recorded and shown in the table.

Table 4.3. Frequency shift data in the experiments.

	1mm Macor	1mm ZTA (Day1)	1mm ZTA (Day2)	1mm Sapphire (to 400C)	2mm Quartz
Chosen Peak frequency	5.8G	6.0G	6.0G	6.0G	5.9G
Sensitivity when Rising	40.1ppm/C	40.5 ppm/C	40.1 ppm/C	80.4 ppm/C	46.0 ppm/C
Sensitivity when dropping	44.6ppm/C	47.9 ppm/C	42.7 ppm/C	82.1 ppm/C	48.0 ppm/C
Frequency difference	11.7M Hz (@50C)	15.6M (@150C)	6.3M (@100C)	6.3M (@100C)	4.7M (@100C)
Distance difference	241.2 μm (@50C)	312.2 μm (@150C)	124.3 μm (@100C)	124.3 μm (@100C)	95.6 μm (@100C)

Theoretically, if the frequency shift is contributed mainly by the alumina tube, the sensitivity should be

$$\frac{\Delta f/f}{\Delta T} = \alpha_{CTE} + \frac{1}{2}\alpha_{TCD}$$

Where α_{CTE} is the coefficient of thermal expansion, α_{TCD} is the temperature coefficient of dielectric constant. For alumina, $\alpha_{CTE} = 6ppm/C$, $\alpha_{TCD} = 115ppm/C$. Thus the sensitivity is

$$\frac{\Delta f/f}{\Delta T} = 63.6ppm/C$$

For the cables with Macor, ZTA and Quartz as thin disk reflector, the measured sensitivities are all about 40ppm/C, roughly one third less than the theoretical value. For the cable with sapphire as reflector, measured sensitivity is about 80ppm/C, roughly one third higher than theoretical value. The reason is that the assembly of the reflectors is loose contact. The thin disks are simply placed between the alumina tubes, but the positions are not fixed. During the heating process, all the materials have dielectric

56

constant change, and all the different parts have thermal expansion. There might also be relative movement between the parts, as their thermal expansions coefficients are different. All these uncertainties caused the sensitivity of these cables to be different from theoretical value.

Another proof of the relative movement of the parts in the cable is that after the heating and cooling cycles, the frequency points will not return to the original points at the same temperature. The frequency differences are listed in the table, and the corresponding distance change is also listed. We can see that the distance changes are between 95 μm to 312 μm, comparing to the disk thickness of 1mm and 2mm. The peak intensity of the reflectors during the temperature change are also recorded. One of the curve of peak intensity change is shown below in Figure 4.17. The numbers 5.7 and 9 means the dielectric constants of the Macor and Alumina respectively.
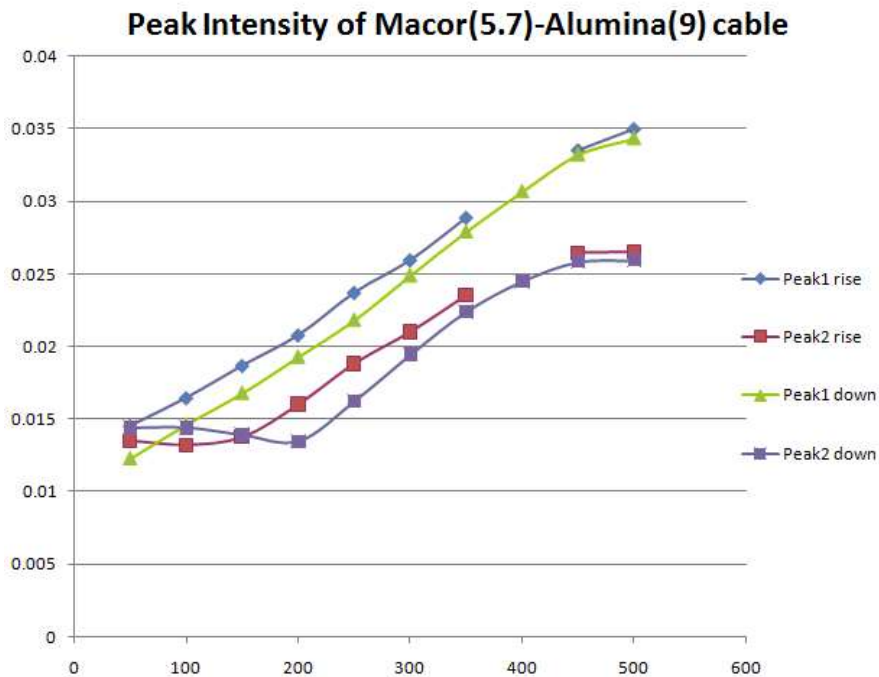
Figure 4.17. Peak intensity of Macor-Alumina cable during temperature change.

Table 4.4 is the reflection intensity data in the experiments. Since the disk reflector is made of different materials other than the cable dielectric, ideally, if the disk reflector is very long, we can calculate the characteristic impedance of the cable containing this new material, denoted by Z_L. Comparing to the characteristic impedance of the original cable Z_0, we can calculate the reflection using

$$\Gamma = \frac{Z_L - Z_0}{Z_L + Z_0}$$

The calculation results are shown in the table. However, the reflector is a thin disk, and the real reflection is the sum of the two reflections at the two end-faces of the disk. Combining this effect with the loss from the cable and connectors, the measured reflections are much smaller than the ideal single reflection value.

Table 4.4. Reflection intensity data in the experiments.

	1mm Macor	1mm ZTA (Day1)	1mm ZTA (Day2)	1mm Sapphire (anisotropic)	2mm Quartz
Ideal single reflection	10.9%	8.0%	8.0%	6.1% or 1.35%	23.2%
1st Peak 100C	1.65%	4.19%	3.99%	2.11%	5.22%
2nd Peak 100C	1.32%	3.58%	2.61%	1.81%	4.23%
1st peak 500C	3.50%	2.84%	2.43%	0.66%	6.07%
2nd peak 500C	2.66%	2.69%	2.72%	0.49%	5.70%

1st peak Intensity with rising temp.	Increasing	Decreasing	Decreasing	Decreasing	Increasing

All the cables have two reflectors in the cable, which are represented as the 1st peak and the 2nd peak in the table. The first reflection intensity is always monotone increasing or decreasing, but the 2nd peak does not usually change monotonically. The reason is that the power arrived at the second reflector is the total power subtracting the power reflected from the first reflector, as well as the power attenuated along the cable. The changing of the reflected power from the first reflector will also influence the peak intensity of the second reflector, hence the complex changing trend of the intensity. For this reason, the value of the first peak gives more accurate information on the reflector property than the second peak.

During the temperature change from 100°C to 500°C, the 1st peak intensity almost doubled on the 1mm Macor cable. For the 1mm ZTA and 1mm sapphire cable, the peak intensity almost halved. For the 2mm quartz cable, the intensity increased for about 20%. It is also interesting to see that for disk material with lower dielectric constant such as Macor and Quartz, the peak intensity increase with rising temperature, while for disk material with higher dielectric constant such as ZTA and Sapphire, peak intensity will decrease with rising temperature.

To demonstrate the reflection intensity change with temperature of a single interface, a 'hollow cavity' structure cable (shown in Figure 4.18) was tested. The first interface is represented by peak1, and the second interface is peak2. The intensity change is shown in Figure 4.19.
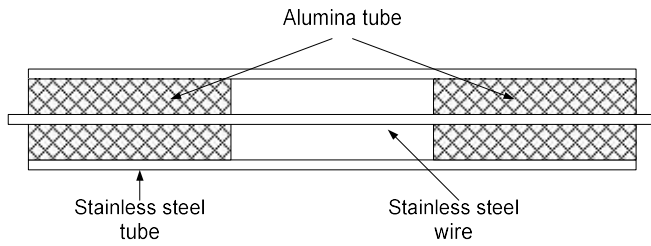
Figure 4.18. Hollow cavity structure under test.
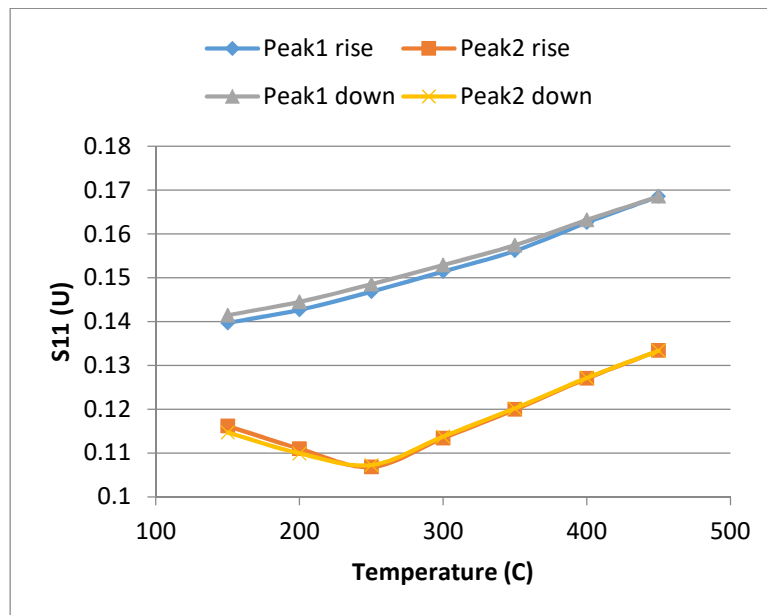
Figure 4.19. Peak intensities of the hollow cavity structure.

Figure 4.19 shows that the single interfaces do have the reflectivity of 15% and more, higher than that of disk reflectors, which agrees with our assumption. Also, the reflection intensities follow almost the exact same curve during the heating and cooling procedure. Comparing to the intensity difference at the same temperature in previous experiments, this means that without the complex assembly parts, the structures are more stable.

Similarly, a 'disk-cavity-tube' structure cable shown in Figure 4.20 is tested to verify the stability of a single thin disk. The reflection intensity change of the disk and the first interface of cavity and alumina tube are shown in Figure 4.21.
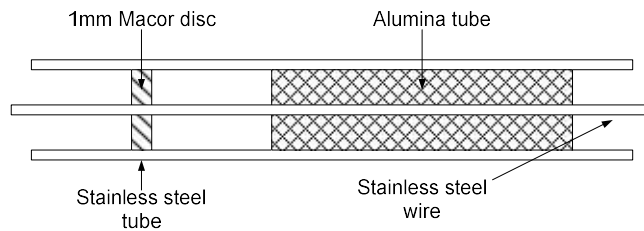
Figure 4.20. Disk-cavity-tube structure under test.
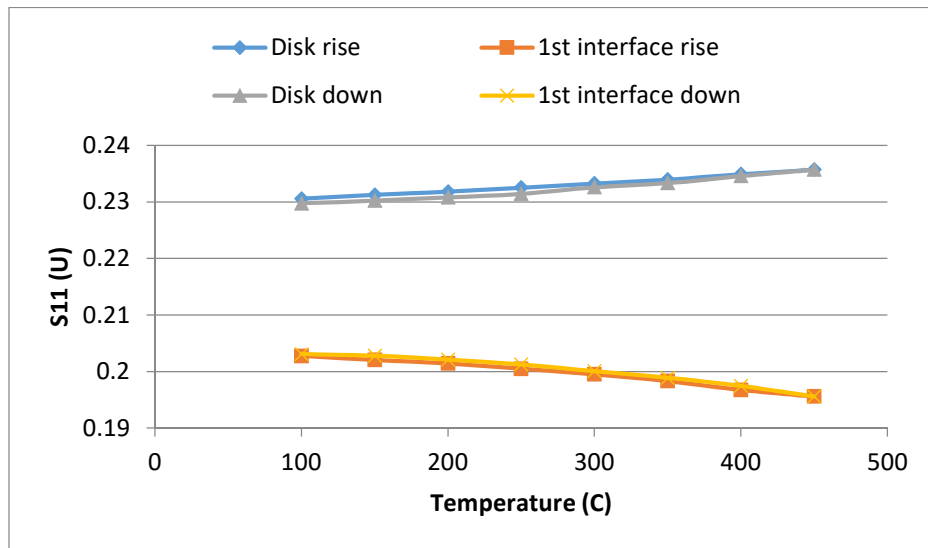
Figure 4.21. Peak intensities of disk-cavity-tube structure.

Again, as expected, the thin disk has a very high reflection of more than 23%. The reflection intensity is also stable at the cavity to alumina tube interface, but not as stable at the thin disk reflector.

From the above experiment results we can see that using different material as thin disk reflector is a valid way to adjust the reflection intensity. However, after putting the disk into the cable, due to assembly errors, gaps between interfaces and small cracks on the disks, the measured results usually do not have good repeatability. That means after a heating and cooling procedure, the cable structure will have a slight change in dimensions (95μm to 212μm as in our experiments). We should try to minimize or eliminate this dimensional instability to improve the sensor structure.

4.5 Air gap reflectors in the MCCC-FPI

We have shown that the thin disk reflectors have stability and repeatability issue during the temperature tests. Another way to create the reflectors is to directly cut materials off the ceramic tube, and the reflection will occur due to the dielectric material mismatch. To cut into the ceramic tube, a DeWalt 4 inch continuous diamond circular saw blade is mounted onto a Mark V series 600 Metallurgical Sectioning Machine (Figure 4.22), and the ceramic tube is fixed at the cutting point. The cutting depth is controlled so that the inner hole is just reached by the diamond blade.

Figure 4.22. Diamond blade and the sectioning machine for groove cutting.

In this experiment, two grooves are cut into the ceramic tube with a separation of 7.5cm. The cutting process is almost the same for the two grooves so that roughly the same depth is reached, and hence the induced reflections are very similar to each other. The resulted tube is then mounted on a stainless steel wire as inner conductor, and a stainless steel tube is mounted outside it as an outer conductor. This cable is then measured with VNA and the time domain reflection (TDR) signal is shown in Figure 4.23.
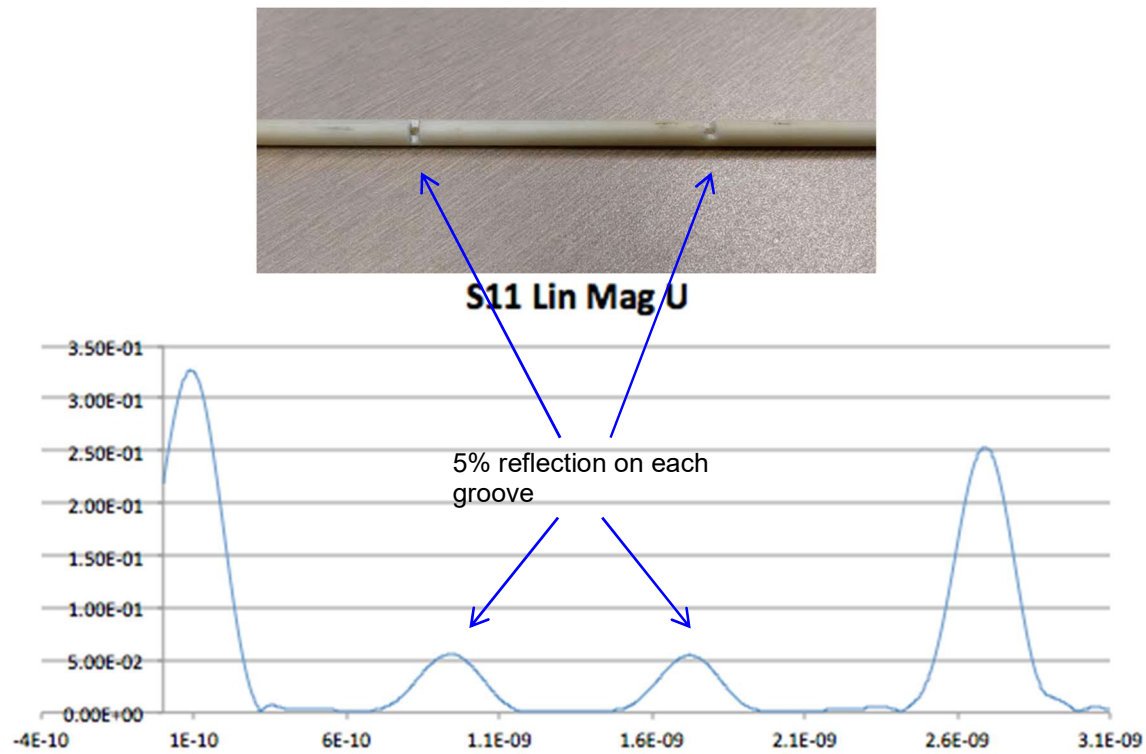
Figure 4.23. Ceramic tube after cut and the time domain reflection signal of the cable made from it.

The TDR signal shows that the reflection at this cutting depth is slightly above 5%, which is good for reflectors in distributed sensing applications. The left and right peak with reflections of 32% and 25% are from the interface of the tube ends and the air.

We put this cable into furnace and performed temperature cycle tests. The cycle started at 200C, and then ramped to 275°C, 350°C, 425°C, and 500°C. It was then decreased to 425°C, 350°C, 275°C and 200°C. Each ramping/decreasing section took 20 minutes, and at each temperature, it was hold for 10 minutes. A temperature cycle took about 4 to 5 hours.

The test results of the first 3 cycles are shown in Figure 4.24. In the first cycle, we saw some hysteresis phenomenon as expected. This is because of the heat treatment effect of the ceramic tube during the temperature cycle after the cutting. The position of the frequency peak at about 7.1G Hz was recorded. After the first cycle, the cable's response became better, as the peak positions of rising and dropping period got closer to each other at the same temperature. At the 3rd cycle, we can see that the rising and dropping period almost have the same peak position. Further examining the data of the 3rd cycle, we can calculate that at 7.1G Hz, the sensitivity in frequency is -337.3 KHz per degree. Divided by the operating frequency 7.1G, we have,

$$\frac{\Delta f / f}{\Delta T} = 47.6 ppm/C$$

This value is about a quarter smaller than the theoretical value of alumina, which is 63.6ppm/C as we calculated in the previous reports. The reason might be that the structure is not pure alumina, but with metal wire inside. The spectra of the 5 temperature points during the rising period in the 3rd cycle are show in Figure 4.25. We can see that the spectra moved left with the temperature rising.
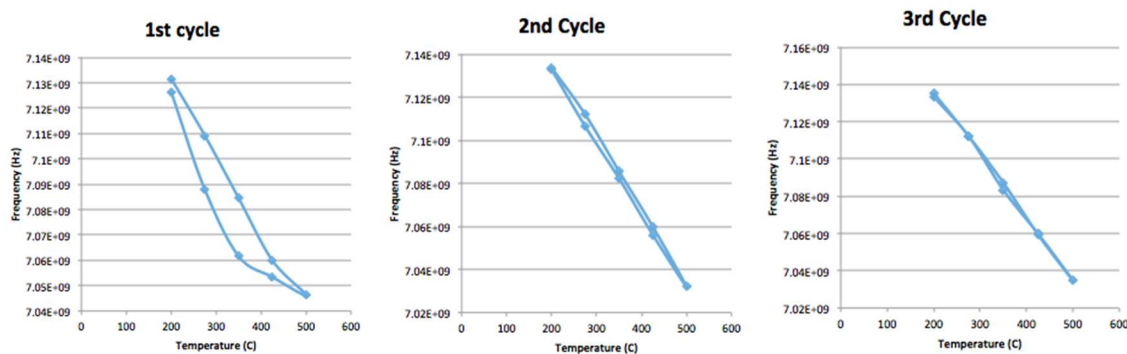
Figure 4.24. Peak frequency shift of the first 3 temperature cycles from 200C to 500C.
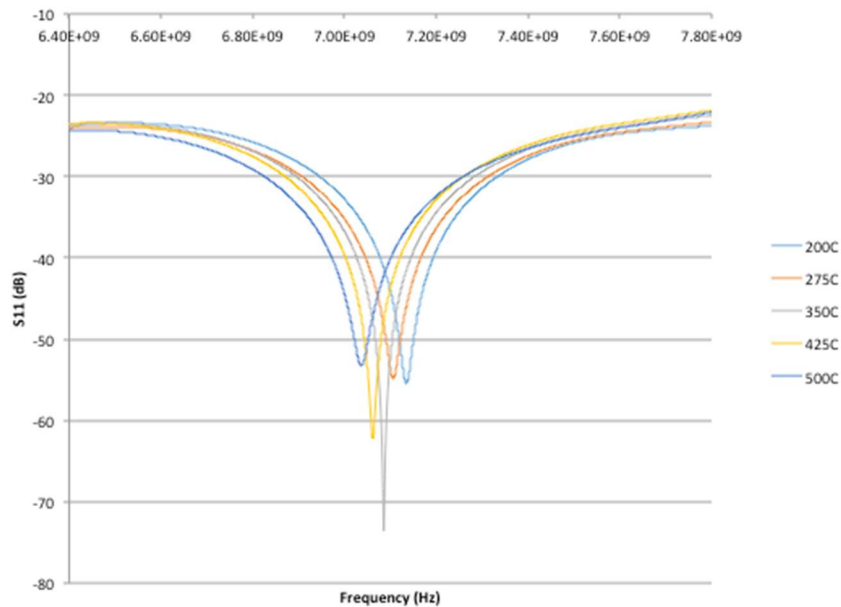
Figure 4.25. Peak Spectra at different temperatures in the rising half of the 3rd temperature cycle.

We continued to run 2 more temperature cycles on the cable with the same temperature profile. Excluding the first cycle, which has obvious hysteresis effect, the data of the 2nd to 5th cycles are plotted together in Figure 4.26. From the figure we can see, at each temperature, there is about 8 to 10 MHz frequency fluctuation. The good sign is that it is a random fluctuation, not a drifting effect that goes in one direction with more cycles done. The peak is at 7.1G Hz, so the relative fluctuation is small comparing to the other tests when the peak is at 4G Hz.
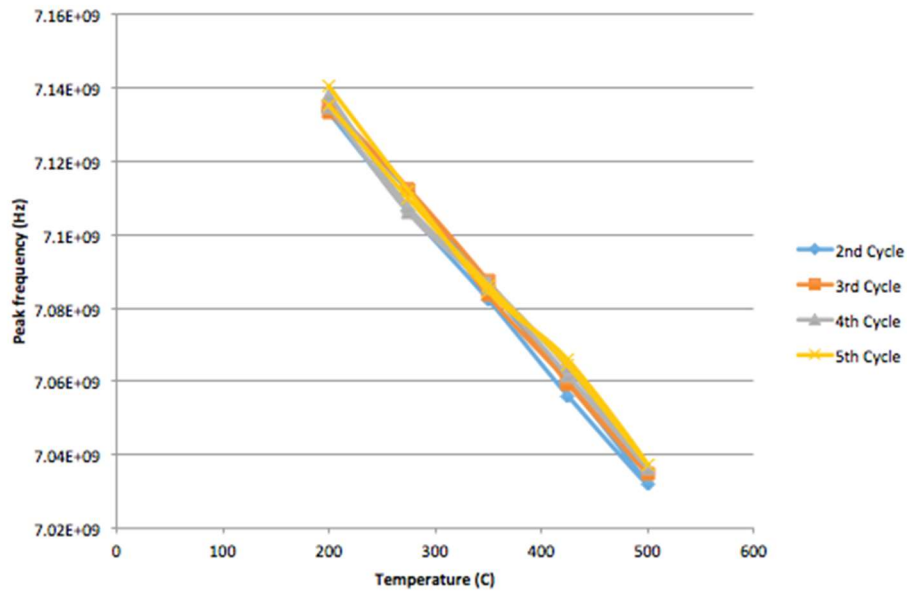
Figure 4.26. Frequency peak shifts of 4 cycles from 200C to 500C plotted together.

To make sure that the drift at high temperature is small, we modified the temperature profile so that the furnace held for 2 hours at 500°C, instead of 10 minutes. We recorded two data points at 500°C, at the beginning and the ending of the 2 hours. The holding time at other temperatures were still 10 minutes and the ramp time were still 20 minutes. Another 2 cycles were run and the result is show in Figure 4.27. In this figure, there is no obvious drift at 500°C, which means that this structure can help to reduce the temperature-drifting problem.
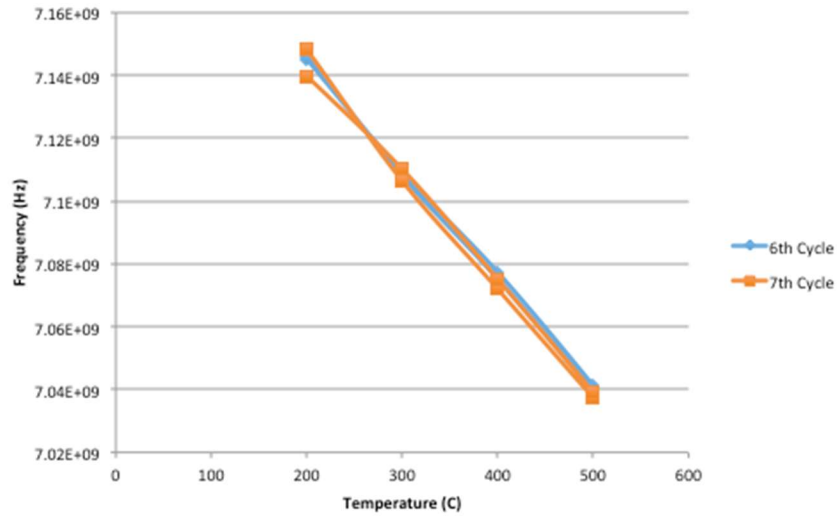
Figure 4.27. Frequency peak shifts of 6th and 7th cycles. Temperature was kept at 500C for 2 hours during these two tests.

The above experiment results show that using a diamond blade to directly cut into the ceramic tube, we are able to make two reflectors with about 5% reflection without assembly issue. The sensor made from it is tested in temperature cycles between 200°C to 500°C. The sensitivity of this sensor is about 47.6ppm/C, and during the 4 days' tests, there is a fluctuation of about 10M Hz for each temperature at the 7.1G peaks. Despite the fluctuation, there is no obvious drift in a 2 hours holding period at 500°C. We believe that sensors with air gap as reflectors have better repeatability than thin disk reflectors.

4.6 High temperature experiment and result

A CC-FPI sensor made from air gap reflector is then tested from 100°C to 900°C to test its performance under high temperature. Figure 4.28 shows the spectrum shift

when the temperature is rising and dropping. Figure 4.29 shows the movement of the resonant dip near 6G during the temperature test. After the first temperature rising, the sensor shows good repeatability during temperature cycle up to 900°C.
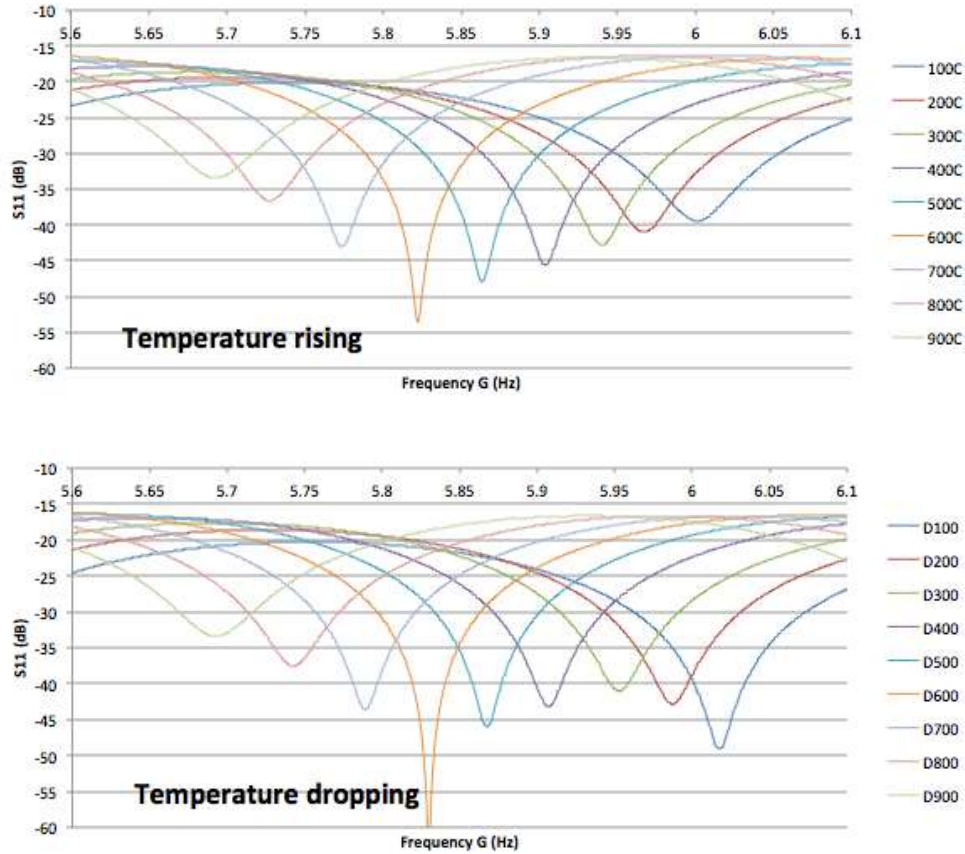
Figure 4.28. Spectrum shift of a CC-FPI sensor during temperature rising and dropping between 100C to 900C.
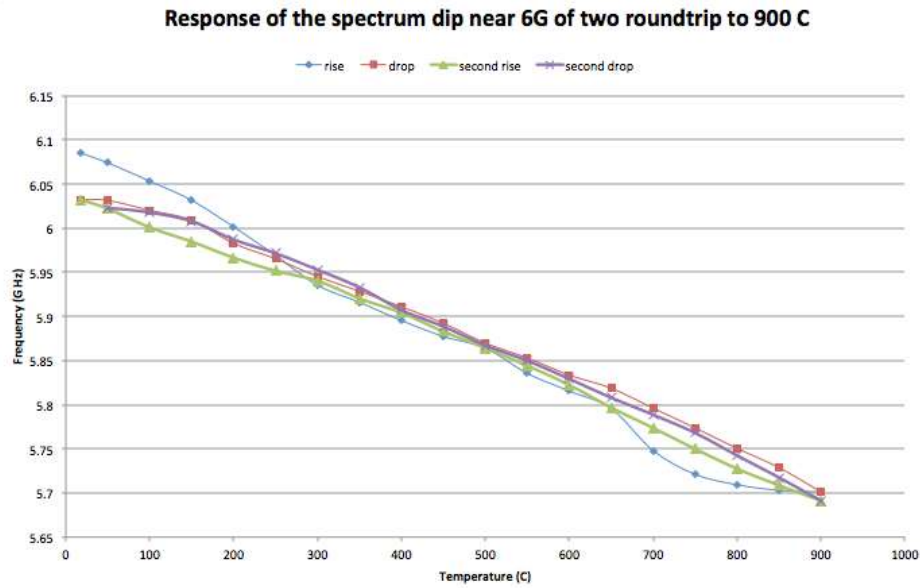
Figure 4.29. The resonant dip near 6G of the spectrum during the temperature test.

A real time temperature monitoring test is carried out to show the sensor's response time to environmental temperature changes. Figure 4.30 shows the frequency change as in response to the programmed temperature change of the tube furnace. The sensor shows a fast response time of less than 180 s for a heating rate of 10° C/min.

70
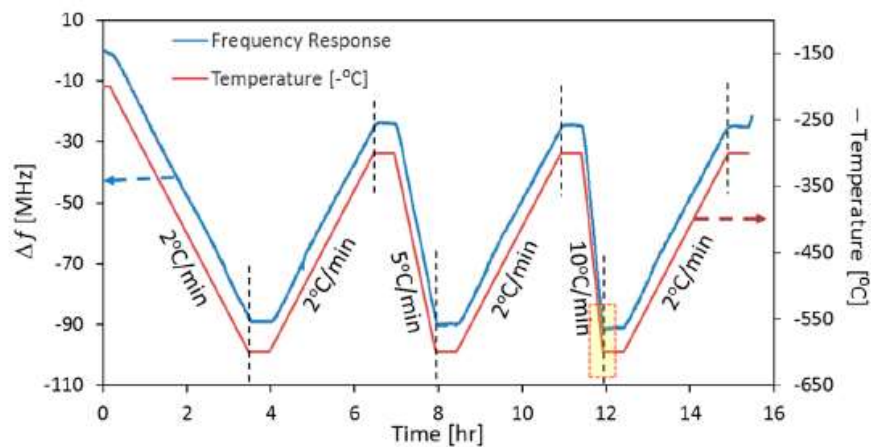
Figure 4.30. The frequency change in response to temperature change of the furnace.

The above experiments demonstrated the lab developed MCCC-FPI sensor response up to 900°C. High temperature performance is proved for this kind of sensor. The sensor here only includes 2 reflectors, which forms only one sensor. By building in more reflectors, we can form more temperature sensors, and by employing the joint-time-frequency domain demodulation method, a distributed temperature can be made which works at very high temperature.

CHAPTER FIVE

V.   DISTRIBUTED TORSION SENSOR BASED ON CASCADED COAXIAL

CABLE FABRY-PEROT INTERFEROMETERS

5.1 Introduction

[15]Torsion/torque is an important physical parameter that needs to be measured
in various industry applications. For example, in the petroleum industry, the torque or
torsion monitoring during the drilling process for oil and gas explorations and
productions has attracted a lot of interests. Drilling into the subsurface to exploit oil and
gas requires large surface equipment in the form of a drilling rig connected to a drill
consisting of a drilling bit and connecting pipes to the surface. There has been substantial
improvement in drilling operations in the last decades with focus on better control of the
drilling process for improved safety and productivity [16][17]. Currently there is a big
emphasis to automate the drilling operation [18]. One of the key element in automate the
drilling operation is to have good downhole data as input of drilling algorithms [19]. A
key parameter is torque/torsion in the bit and in the pipe to improve drilling efficiency
and avoid twist-off of the drill pipe [20]. Surface measurements are less preferred due to
all the vibration and frictional losses occurring while drilling [21][22]. Thus, a sensing
system that can monitor the torque/torsion distribution in the bit and pipe is of great
interest. In addition to drilling process controls, distributed torsion measurement can be
useful in many other applications such as for condition monitoring of an oil or gas
pipeline and the drivetrain of heavy machineries.

Torsion measurement is commonly based on strain gauges or other elastic deformation transducers bonding on the shaft under torsion. If the shaft is rotating, a slip ring is used to take the signal from the gauge. One of the challenges in strain-gauge based approaches is the difficulty to route multiple strain gauges' signals using a slip ring. Non-contact torsion sensors such as magnetic [23], capacitive [24] or optical based [25] sensors can avoid the slip ring arrangement. For example, a non-contact torque sensor with multiple hall sensors has been developed, and performs well under rotation speeds ranging from 300 rpm to 500 rpm with less than 2% of linear and repeatable data [26]. But most of the non-contact sensors have limitations in shaft material, rotation speed, or measurement resolution. Fiber optic torsion sensors, such as fiber Bragg gratings (FBG) [27][28], long period fiber gratings (LPFG) [29], Photonic Crystal Fiber (PCF) based Sagnac interferometers [30], and polarization-based sensors [31] have also been investigated for torsion measurement. In general, fiber sensors are lightweight, flexible and easy to embed. Some of them can have multiple sensors fabricated on the same fiber to realize distributed sensing. However, their robustness has been a concern due to the brittleness of the fiber, especially in many applications where heavy machineries are involved.

Coaxial cables are low-loss waveguides for transmission of radio frequency (RF) signals, which have a much lower frequency than that of the light waves. Coaxial cables and optical fibers are governed by the same electromagnetic theory. Many fiber optic sensor techniques can be mimicked on a coaxial cable, such as Bragg gratings [32] and Fabry-Perot interferometers [9]. Different from an optical signal, the phase of a RF signal

73

can be easily obtained using commercial equipment, such as the vector network analyzer (VNA). This offers the coaxial cable based sensor the distributed sensing capability. In addition, a coaxial cable can be constructed using many types of materials, offering the much needed robustness in filed applications. These features make the coaxial cable based sensor a very good candidate for many sensing applications, especially for those involving heavy duty, larger strain, and other harsh conditions.

In this chapter, we propose a coaxial cable based distributed torsion sensor based on cascaded Fabry-Perot interferometers. The sensing mechanism is described and the distributed torsion measurement capability is demonstrated experimentally.

5.2 Working principle of coaxial cable based distributed torsion sensor

The schematic of the proposed sensor and the operation principle are illustrated in Figure 5.1, where the cable sensor is mounted firmly on a shaft or other structure in a helical form. When the shaft is under torsion, the sensor measures the strain of the structure and correspondingly the torsion that produces the strain. The coaxial cable torsion sensor consists of a series of Fabry-Perot cavities on a flexible coaxial cable. Each cavity is constructed by two adjacent reflectors on a coaxial cable. The transmitted RF signal is partially reflected from the two reflectors and the reflected signals superimposed to form an interference pattern (i.e., an interferogram) that can be observed in the spectrum domain. When a strain is applied on the cable, the cavity length and the dielectric constant of the insulating material will change. As a result, a shift in the interferogram can be recorded and used to calculate the applied strain. To realize

distributed sensing, multiple weak reflectors can be constructed on a single coaxial cable

[33]. Each reflection along the cable should be weak enough so that the majority of the

RF signal can transmit through the whole cable and the multiple reflections between the

reflectors are negligible. In such a configuration, the entire structure is divided into

sections defined by the cascaded coaxial cable Fabry-Perot interferometers for distributed

measurement.
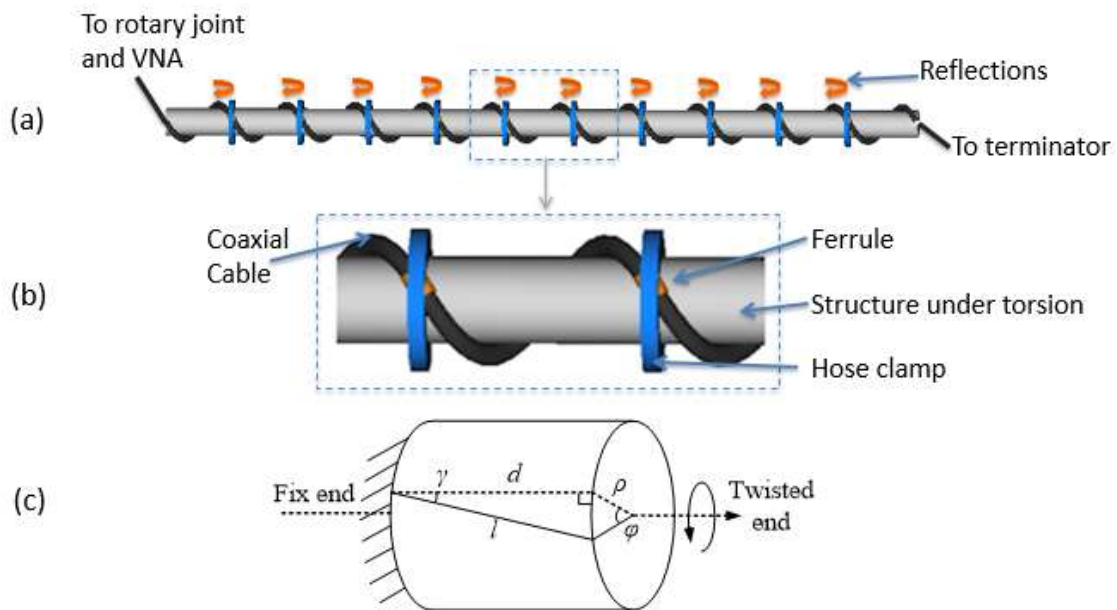
Figure 5.1 Schematic of the distributed torsion sensor: (a)Sensor installation on the

structure under torsion (b)Enlarged view of a sensor section and (c) Relationship between

twisted angle of the shaft and the strain on the cable.

For each section of the torsion sensor, the relationship between the twisted angle

of the shaft and the strain on the coaxial cable is shown in Figure 5.1 (c), where the

section of the shaft is considered to be fixed at the left end and torsion is applied on the

right end for easy calculations. On the actual sensor, these two ends are defined by the two adjacent reflectors on the coaxial cable. In the installation, the coaxial cable sensor is spiraled on the shaft, and the installation angle between the cable and the axial direction of the shaft is γ. When radial offset angle of φ occurred, the twist rate of the shaft on this section is defined as

$$\tau = \frac{\varphi}{d} \qquad\qquad (5.1)$$

where d is the axial length of the shaft between the two reflectors.

The length (l) of the cable between two reflectors is given by

$$l = \sqrt{d^2 + (\rho\varphi)^2} \qquad\qquad (5.2)$$

where ρ is the radius of the shaft. The installation angle $\square$ is related to the cable length l and the radial angle φ by the following equation

$$\sin\gamma = \frac{\rho\varphi}{l} = \frac{\rho\varphi}{\sqrt{d^2 + (\rho\varphi)^2}} \qquad\qquad (5.3)$$

A torsion applied to the shaft will produce a change to the radial offset angle in the amount of $\square\square$. Correspondingly, when $\Delta\varphi$ is small the length change of the cable Δl can be calculated by taking the derivative of l in equation (5.2) with respect to φ, resulting in

$$\Delta l = \frac{\rho^2\varphi}{\sqrt{d^2 + (\rho\varphi)^2}}\Delta\varphi \qquad\qquad (5.4)$$

Rewriting equation (5.3), we have

$$\frac{\Delta l}{l} = \frac{\rho^2 \varphi^2}{d^2 + (\rho \varphi)^2} \left(\frac{\Delta \varphi}{\varphi} \right) = \sin^2 \gamma \left(\frac{\Delta \varphi}{\varphi} \right) \qquad (5.5)$$

Equation (5.5) indicates that the amount of cable twist ($\Delta \varphi / \varphi$), thus the torsion, is proportional to the strain ($\Delta l / l$) experienced by the coaxial cable. As discussed in [32], the strain is in linear relationship with the resonant peak shift of the interferogram form by the coaxial cable Fabry-Perot interferometer.

One of the key benefits of the coaxial cable Fabry-Perot interferometry is its distributed sensing capability. The strain of each section between two adjacent reflectors can be obtained using the joint-time-frequency domain demodulation method as explained in Chapter 2. With this method, the strain (torsion) distribution along the whole cable (shaft) can be obtained.

5.3 Torsion measurement in a single section

To understand the relationship between the shaft torsion and the cable signal, we first test the torsion response of a single cable Fabry-Perot interferometer made by a pair of reflectors. The test setup is shown in Figure 5.2. The coaxial cable used to make the sensor was a RG-58 cable (Consolidated Wire RG58/U Mil Spec Cable) with a characteristic impedance of 53.5□ and outer diameter of 4.95mm. The reflectors were created by clamping two ferrules (Pan Pacific Enterprise FER-5.6-58U) on the cable. The inner diameter of the ferrule was 5.6mm, slightly larger than that of the cable. The clamp

induced deformation of the dielectric material in the cable and generated a characteristic impedance discontinuity on the cable. In general, the impedance discontinuity is proportional to the amount of deformation. As such the magnitude of the reflection can be controlled by the amount of the deformation. While a large deformation of the cable produces a strong reflection signal, it also increases the loss and limit the maximum number of reflectors that can be implemented on a single cable for distributed sensing. In our experiments, we adjusted the clamping force so that the reflection coefficient was about 5% to balance the signal strength and number of sections. The crimper we used (Paladin 1300 series) in the experiment has 6 settings for crimp depth, which helps to control the reflectivity of the reflectors.

After the two reflectors were created, the cable was wrapped around a testing shaft with a diameter of 12mm. Under pre-strain, the cable was fixed to the shaft at the clamped ferrule points using two hose clamps. The fixing points were collocated with the reflector ferrules to avoid unwanted reflections along the cable. The pre-strain could improve the linearity of the sensor when torsion was applied in both clock-wise and counter-clock-wise directions. The shaft used in the test was relatively soft and easy to twist so that the sensor can be tested within a large dynamic range.

In the experiment, one end of the coaxial cable was connected to the VNA (Agilent E8363), and the other end was connected to a 50 Ohm terminator. The top end of the shaft was fixed on a frame by a holder, while the bottom of the shaft was attached on a rotation stage (Newport PM360). The torsion could thus be applied by rotating the shaft bottom with the shaft top fixed. The distances between the two fixed points on the

shaft was L1=50cm, and the distance between the two reflectors on the cable was

L2=22.7cm.
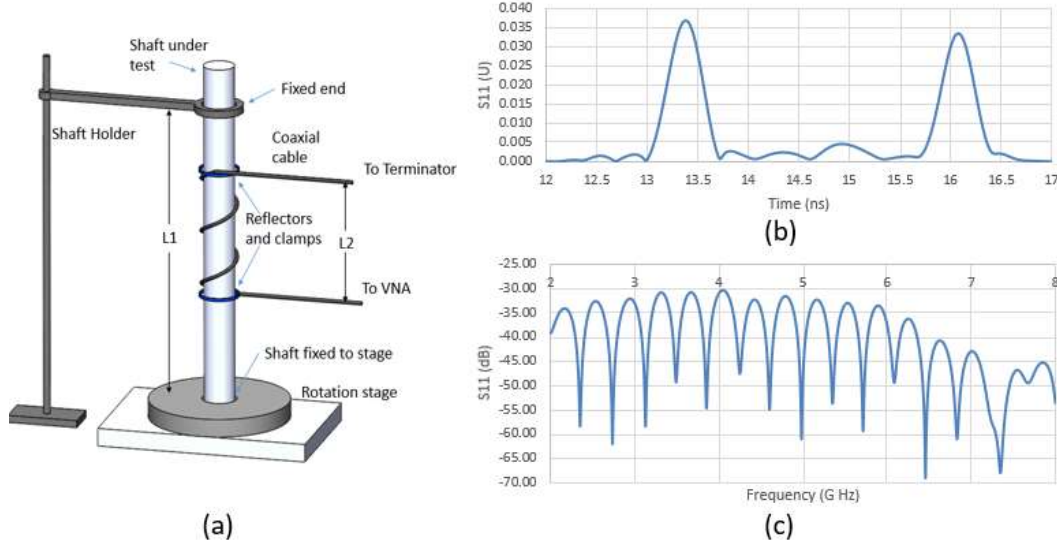
Figure 5.2. Single-section torsion sensor test. (a) Setup to test the single-section torsion sensor, (b) Time-domain reflection signal of the two reflectors defining the Fabry-Perot interferometer, (c) reconstructed interferogram.

The VNA swept its frequency from 2 GHz to 8 GHz to acquire the S11 of the cable. The intermediate frequency bandwidth (IFBW) was 3 kHz and the total number of sampling points was 16001. The acquired S11 spectrum was first transformed to obtain the time-domain reflection signal as shown in Figure 5.2 (b) where the two reflectors could be clearly identified. To improve the signal-to-noise ratio (SNR), a gate function is applied to eliminate the unwanted reflections such as those from the connectors. The gated time-domain signal was then transformed back to the frequency domain. In this way, an interference pattern was obtained as shown in Figure 5.2(c) where constructive

and destructive interference peaks and valleys could be clearly identified. The inference spectrum could thus be used to calculate the change in electromagnetic distance between the two reflectors as a result of torsion.

During the test, the rotational stage was manually rotated with steps of about 5 to 10 degrees. After each step of movement, the S11 of the sensor was collected and processed according to the procedures described above. Figure 5.3 inset shows the interference valley near 4.2G Hz as the rotation angle changed. The valley shifted monotonically towards the lower frequency as the rotation angle increased, indicating increased electrical lengths of the cable between the two reflectors as a result of the increased torsion. Figure 5.3 plots the center frequency of the interference valley as a function of the rotation angle. The response is quite linear with R2=0.99424 in the range from 0 to 250 degrees, which corresponds to 8.726 rad/m in twist rate according to Equation (5.1). The sensitivity of measurement, estimated based on the slope of the fitted line, is 1.834MHz/(rad/m). According to Equation (5.5), the sensitivity can be improved by increasing the installation angle of the cable □, as the cable strain is in proportion to 〚sin〛^2 γ. However, large installation angle requires longer cable wrapped on the same shaft length, making the sensor system bulky. In the extreme case of □=90°, infinite long cable is needed for any length on the shaft, which is not possible. In practice, a moderate □ is advisable to achieve a relatively high sensitivity while keeping the cable on the structure not so bulky. In our experiment, the total number of sampling points is 16001 points, and the frequency span is 6G Hz, so the separation between two sampling points is 0.231 M Hz. However, we can improve the accuracy by curve fitting and interpolation

on the Fabry-Perot cavity spectrum. From our experience, the real limitation on measurement accuracy lies in the stability of the spectrum measured on the VNA, which is influenced by the instrument itself and the stability of the measurement system. Usually we can have the stability of the spectrum of about 10-5. At the pit near 4G Hz, the stability is about 40K Hz, which means that the torsion measurement accuracy is about 0.022 rad/m.
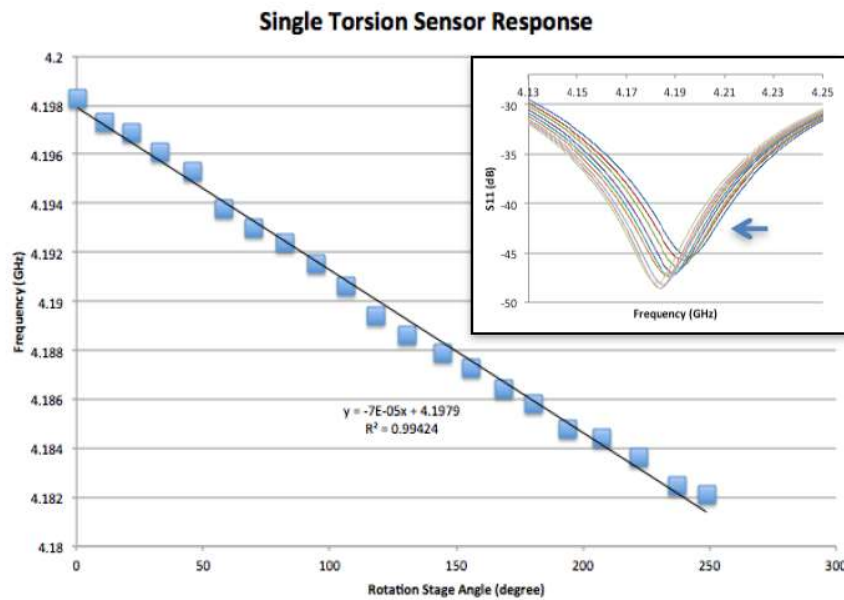
Figure 5.3. Torsion sensor spectrum valley shift with rotation stage position near 4.2 GHz. (Inset: spectra of selected data recorded, shifting left with increased rotation angle.)

5.4 Distributed torsion sensor system

To demonstrate the capability of the distributed torsion sensing, a coaxial cable sensor with three sensing sections was wrapped along the shaft. More individual sensors can be cascaded into the system, but three-section configuration was enough to

demonstrate the distributed sensing principle. To apply torsions on the 3 sections separately, we added some space between the sensor sections to avoid significant crosstalk to adjacent sections when the torsion was applied to an individual section as shown in Figure 5.4. Sensor 1, 2 and 3 were the sensing sections formed by wrapping pre-strained cable FPI sensors around the shaft. Sections of A, B, C and D were relaxed cable sections that did not work as sensors. To show the system's capability for distributed torsion measurements, a torsion was applied to the 2nd sensor section while the other two sections (1 and 3) were relaxed. This was realized by fixing the section B while twisting the shaft at section C using a rotation stage.
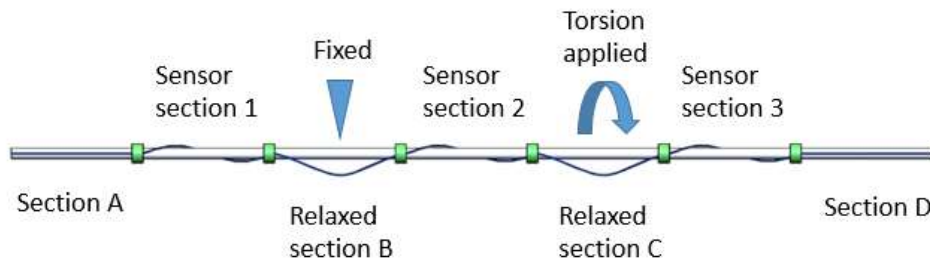
Figure 5.4. Test arrangement to verify the distributed torsion sensing capability of the coaxial cable sensors.

Figure 5.5 (a) shows the reconstructed spectra of the sensor section 2 near the interference valley at 5.1G Hz. With increased torque, the spectrum shifts to the lower frequency indicating the increase of strain. The inset is the spectrum over the whole 6G Hz measurement span. Figure 5.5 (b) shows the response of the 3 sensors when the twist of Section 2 was increased in 5 steps. The sensor of section 2 responded to the applied

torsion as indicated in the frequency shift of the coaxial cable FPI. There were some crosstalks shown in the other sensor sections, which might be caused by the twist crossed through the shaft.

Although only 3 sections were demonstrated, more sensors can be cascaded. Because each reflector will reflect some power, the total reflectors that can be multiplexed on a cable is limited. Theoretically, if the reflectivity of each reflector is R%, and the noise and loss along the cable is negligible, we can multiplex 100/R sensors on the cable. In our other experiment, we have successfully multiplexed 10 reflectors (9 sensor sections) on a cable with good signal to noise ratio, when the reflectivity of the reflectors is about 2%. In real applications, no relaxed section is needed because in principle the time-domain gating can effectively separate the sections. A sensing cable with n reflectors can divide the entire shaft into n-1 sections. With 6G bandwidth, 3 kHz IFBW and 16001 points on the VNA, the data acquisition and processing time is about 2 to 3 seconds. Adding more sections will slightly increase the time for data processing, but the data acquisition time will not change because only one scan of spectrum (S11) is needed for the whole cable. Considering the most time consumption is in data acquisition, increasing the number of sensors will not significantly increase the total measurement time. Temperature crosstalk is another problem that can influence the performance of the sensor. One way to solve this problem is to reserve a relaxed section of sensor on the cable that do not attach to the shaft, just like the relaxed section we had when doing the 3 section distributed sensing experiment. That relaxed section can work as a temperature sensor and can be used for temperature compensation.
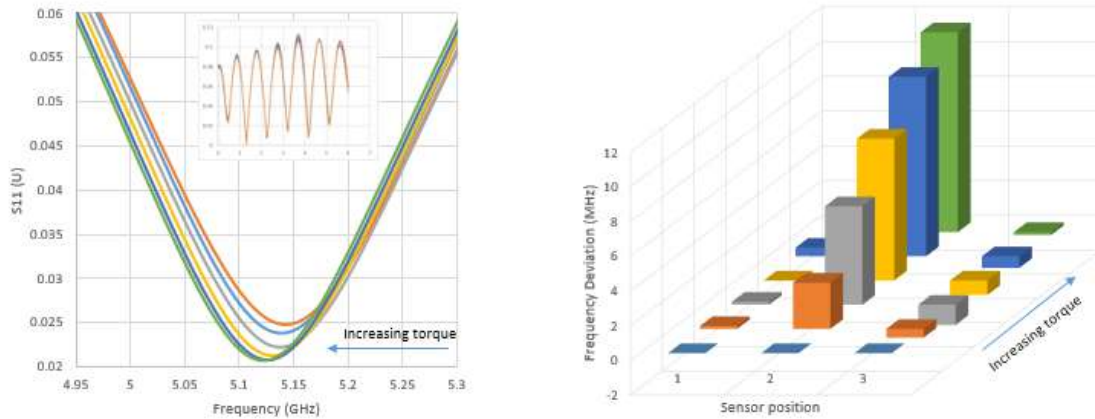
Figure 5.5. Distributed torsion sensing test result. (a) Spectra near 5.1GHz of the second sensor section as the torque increased. Inset is the whole spectra within the 6GHz available bandwidth of the VNA. (b) Responses of the 3 sensor sections along a shaft when the torque is applied to the second section only.

To summarize, a distributed torsion sensor is demonstrated based on cascaded coaxial cable Fabry-Perot interferometers. Multiple reflectors are implemented along a single flexible cable. Any two consecutive reflectors form a FPI that can be used to measure the strain applied between the two reflectors. Reflectors should be weak enough so that interrogating microwave signal can transmit through the whole cable and multiple reflections between the reflectors are negligible. By applying a gating function to the time-domain signal, these reflectors can be isolated and paired to identify the individual sections for distributed sensing. When spiraled around a shaft, the torsion of the shaft can be measured by the distributed coaxial cable strain sensors. The test on a single section showed that a linear response with sensitivity of 1.834MHz/(rad/m) was achieved in the twist rate range of 0 to 8.726rad/m. The distributed sensing capability was also

84

demonstrated in an experiment with three sensors cascaded on the same coaxial cable. The distributed coaxial cable sensor is suitable for many applications including the torque condition monitoring on the drilling bit and pipe condition monitoring in the petroleum industry, as well as other applications such as the structure health monitoring and machine failure detection.

CHAPTER SIX

VI.   3D BEAM SHAPE ESTIMATION BASED ON DISTRIBUTED COAXIAL

CABLE INTERFEROMETRIC SENSOR

6.1 Introduction

[34]Real time deformation monitoring and shape estimation is an important

research area in structure health monitoring (SHM) which helps to detect damage and

ensure efficient maintenance for structures [35][36]. It is also crucial for aerospace

applications such as control of morphing aircraft [37] and aerospace structure condition

assessment [38]. The most straightforward way for deformation monitoring is direct

displacement measurement. Level gauge, deflection gauge and other traditional

displacement sensors have been used, but they suffer from limitations such as vertical

displacement detection only, or difficult to install and monitor in large quantities. Optical

methods such as CCD camera imaging [35][39], Moire projection interferometry [40] and

pattern recognition [41] were also studied, but these imaging methods are hard to use on

aerospace applications, because it is not possible to install the sensing system outside of

the structure to be monitored [38]. Other method such as GPS assisted estimation has also

been explored [42], but it can only work on large structures and the accuracy is relatively

low.

The other way for shape estimation is reconstruction from other characteristics of

the structure, such as strain or curvature. Curvature data has been used to reconstruct

surface profiles [43][44], but they rely on special curvature sensors and are hard to

deploy on large structures. Later, reconstruction methods from strain data have attracted a

lot of attention. Theoretically, displacement-strain transform (DTS) has been studied in multiple research papers [45][46][47]; experimentally, several groups have reported their works of deformation monitoring based on strain measurement [48][49], where the measured data are usually obtained by strain gauges.

Recently, fiber optic sensors have received more and more attention in distributed strain sensing. Multiple fiber based sensors such as fiber Bragg gratings (FBG) or Fabry-Perot interferometers can be multiplexed on a single fiber to avoid deploying large amount of point sensors on a structure as in strain gauge based systems. Techniques such as OTDR and Brillouin-scattering based sensors can achieve distributed strain data with high spatial resolution along the fiber. Specifically, long-gauge fiber sensors [50], FBG sensor systems [51][52], and Brillouin-scattering based sensors [53][54] have been reported to be used in shape estimation systems. However, fiber sensors are less robust and have a small tensile strain limit (<0.4%) due to the brittleness of the materials made of fibers, which limits their applications in harsh environment, large deformation and heavy duty scenarios.

On the other hand, coaxial cables share the same electromagnetic theory with optical fibers as electromagnetic wave carrier, which makes it possible to migrate mature fiber optic sensor technologies to coaxial cable platform. In recent years, several fiber optic sensing devices have been mimicked on coaxial cables, such as Bragg gratings [32], couplers [14] and interferometers [9]. Comparing to fiber devices, coaxial cable based sensors have the advantage of robustness and large strain capability, which make them suitable for structure health monitoring applications.

In this chapter, a 3D beam shape sensing system based on distributed coaxial cable sensors is presented. In the following sections, the working principle of the sensor and the system is introduced first. The sensor fabrication and installation is then discussed, followed by the details of the signal processing method. In the end, we show the experiment results of the distributed strain sensing and beam shape reconstruction.

6.2 Working principle of coaxial cable based beam shape sensor

The working principle of the proposed sensor system is shown in Figure 6.1. The system consists of two distributed coaxial cable sensors connecting to a vector network analyzer (VNA). The VNA sends out the linearly swept frequency microwave signal, and measures the reflected or transmitted magnitude and phase of the input signal at the same swept frequency within the intermediate frequency bandwidth (IFBW) The cables are attached to the beam under load, one on the top and the other on the side, and they will pick up the strain data corresponding to the bending in the vertical and horizontal plane respectively. Multiple reflectors are embedded on the cables to create proper reflections. Each adjacent reflector pair on the cable will form a virtual Fabry-Perot cavity, which is the sensing element for local strains.

In a single scan, the VNA will take up the amplitude and phase of the reflection signal of the cable, which include the reflections from all the reflectors along the cable. Although there are multiple virtual Fabry-Perot cavities on the cable, individual cavity interferogram can be reconstructed with signal processing methods, which will be introduced in the later sections in this paper. The strain can be calculated from the

88

frequency domain data. Assuming the cavity length is L, the mth order resonant

frequencies of a virtual Fabry-Perot cavity is

$$f_m = \frac{mc}{2L\sqrt{\varepsilon_r}}$$
(6.1)

Here, m=0, 1, 2, …, and c is the speed of light in the coaxial cable. ε_r is the effective

dielectric constant of the coaxial cable.

Assume that the effective dielectric constant remains the same, when there is a

cavity length change of ΔL, the resonant frequency change is

$$\Delta f_m = \frac{mc}{2(L+\Delta L)\sqrt{\varepsilon_r}} - \frac{mc}{2L\sqrt{\varepsilon_r}} = -\frac{mc}{2}\frac{\Delta L}{L(L+\Delta L)\sqrt{\varepsilon_r}} = -f_m\frac{\Delta L}{L+\Delta L} \approx -f_m\frac{\Delta L}{L}$$

when $\Delta L \ll L$.

Which means

$$\frac{\Delta f}{f} = -\frac{\Delta L}{L} = -\varepsilon_x$$
(6.2)

at any resonant frequency, where ε_x is the local axial strain on the cable.

In this way, the strain at each section of the sensor can be calculated, and the distributed

strain data in both vertical and horizontal plane can be obtained.
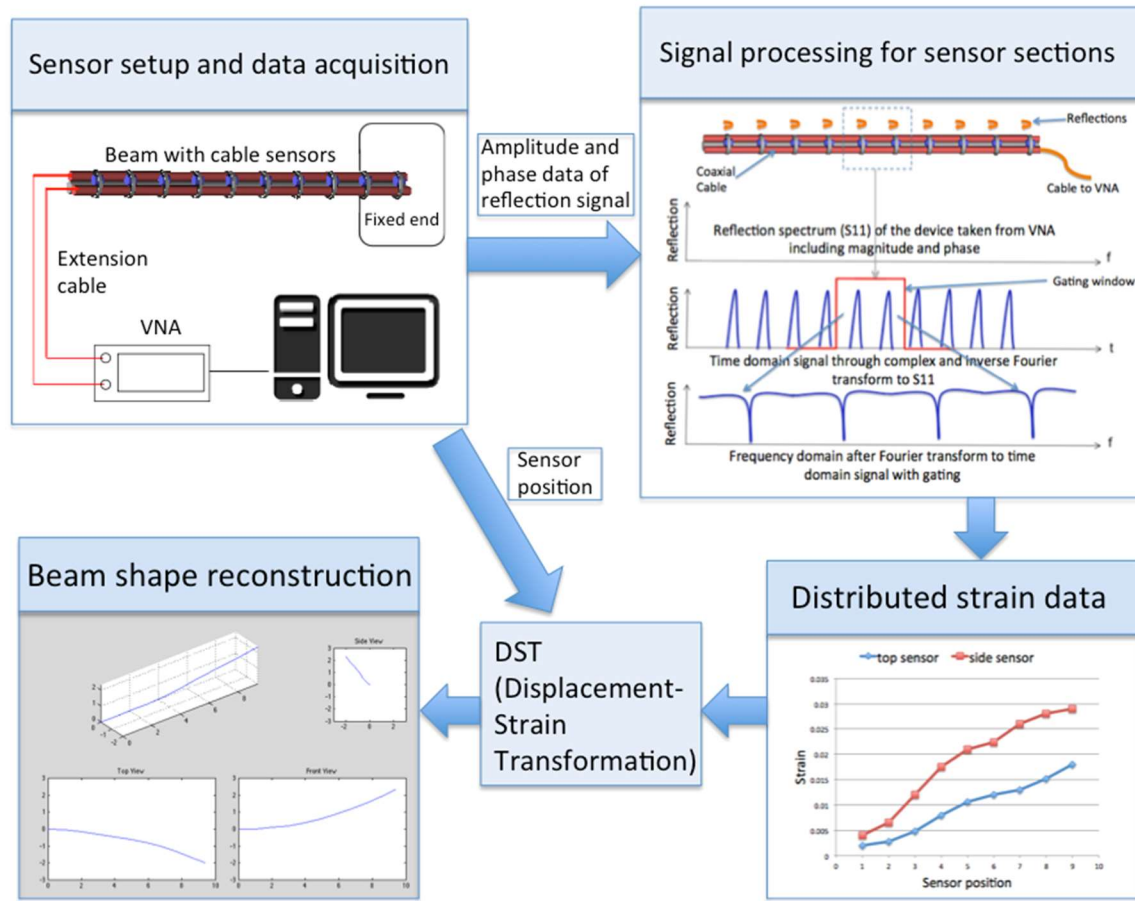
Figure 6.1. Working principle of the proposed 3D beam shape sensor system.

The next step is to reconstruct the beam shape from the strain data. This is realized by displacement-strain transformation (DST), which has been studied a lot in shape sensing area. Here, we use a simple integration method, and the principle is explained below.

Let's first look at the sensor arrangement. Assume a situation of 3-D bending of a beam of circular cross section with radius r. In the coordination shown in Figure 6.2(a),

the cross section of the beam is in y-z plane and the length of the beam is along the x-axis, the strain in the x direction at a certain point can be given by,

$$\varepsilon_x = -\frac{z}{\rho_y} - \frac{y}{\rho_z} \qquad\qquad (6.3)$$

where y is the distance from the point to the neutral plane in y direction, z is the distance from the point to the neutral axis in z direction, ρ_y is the radius of curvature of the beam at the point in x-z plane, ρ_z is the radius of curvature of the beam at the point in x-y plane. To avoid cross talk, we put one sensor cable on the top of the beam in the x-z plane (the cable is at the intersection of y=0 and z=r plane), and the other cable on the right side of the beam in the x-y plane (at the intersection of z=0 and y=r plane). When the bending happens in x-z plane in the negative z direction, the top sensor cavities will be elongated to produce a strain. However, the right side sensor is in the neutral plane of the bending, so there is no change in the effective length of each cavity, and no strain will be produced. This ensures that the top cable sensors only take up the strain in x-z plane, and the right side sensors only take up the strain in x-y plane; no cross talk will happen here.

(a)   (b)

91
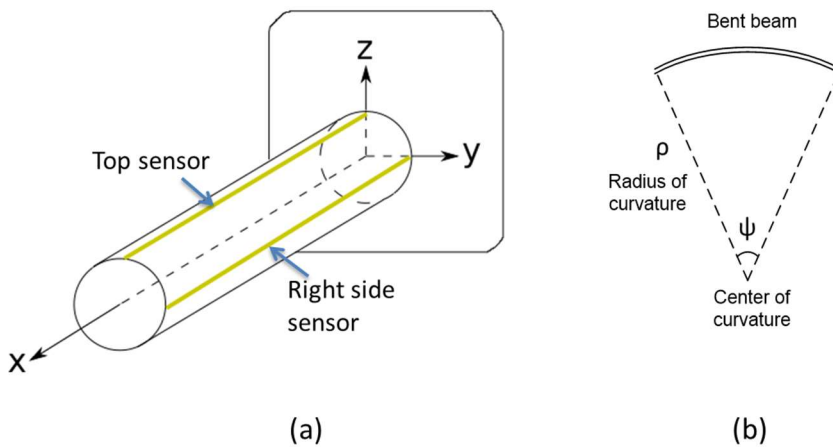
Figure 6.2. Beam shape sensor position. (a) Placement of the two coaxial cable sensors on the beam. (b) Radius of curvature of a beam section.

Suppose the projection of the neutral axis in x-y plane is y(x). In this plane, the radius of curvature of a beam section is ρ, as shown in Figure 6.2(b). On the y(x) curve at any point, ρ has the following relationship with y' and y''

$$\frac{1}{\rho} = \frac{y''}{[1+(y')^2]^{3/2}} \approx y'', if\ y' \ll 1 \qquad (6.4)$$

For the sensor on the right side, we have y=r, z=0. Bring them as well as equation (6.4) into equation (6.3), we find that

$$\varepsilon_{side} = -\frac{r}{\rho_z} = -ry''$$

Integrate y'' two times to express y as

$$y(x) = \int_0^x \int_0^x y'' dx^2 = \frac{1}{r}\int_0^x \int_0^x \varepsilon_{top}(x)dx^2 \quad (6.5)$$

Similarly, z can be expressed as

$$z(x) = \frac{1}{r}\int_0^x \int_0^x \varepsilon_{side}(x)dx^2 \quad (6.6)$$

Where $\varepsilon_{top}(x)$ and $\varepsilon_{side}(x)$ are strain distribution along the beam measured by the top and right-side sensor respectively. Equations (6.5) and (6.6) are the relationship between displacement and strain. If we know the continuous strain distribution function along the cable, the shape of the beam can be calculated from this relationship in theory. However, in practice, we can only have discrete strain data along the beam from our measurement system. The strain distribution can be estimated by assuming uniform strain distribution on each section, or other method such as spline regression from the discrete strain data.

6.3 Sensor fabrication and setup

The structure of the sensor and its setup is shown in Figure 6.3. Two RG 58 flexible coaxial cables are attached to the round beam under test. Each cable has ten ferrules crimped on them to create reflections. The crimp depth is adjusted so that the reflection is about 1% to 3%. Too low reflection will cause problems in signal to noise ratio, while too high reflection will limit the number of reflectors on the same cable. One of the cables is attached on the top of the beam and the other cable is attached to the right side as mentioned in the previous section. Ideally, the two cables are 90 degrees apart in the cross section of the round beam to eliminate cross talk between vertical and horizontal bending. To fix the cables on the beam, a hose clamp is used, and the clamping point is right at the ferrules on the cable to avoid creating additional reflections. This also requires the ferrules on the two cables to be at the same positions along the cable, so the two cables can be fixed on the beam with the same hose clamp. In this experiment, a dummy cable section of proper radius is inserted in the hose clamp to help ensure the position of the two cables to be 90 degrees apart in cross section plane. It is worth noting that a pre-strain is needed when fixing the sensor sections. This is done by pulling the cables while fixing the clamps. The pre-strain does not have to be very big, as long as the cables are not relaxed. Any relaxation on the cable will cause the measured strain data to be inaccurate.
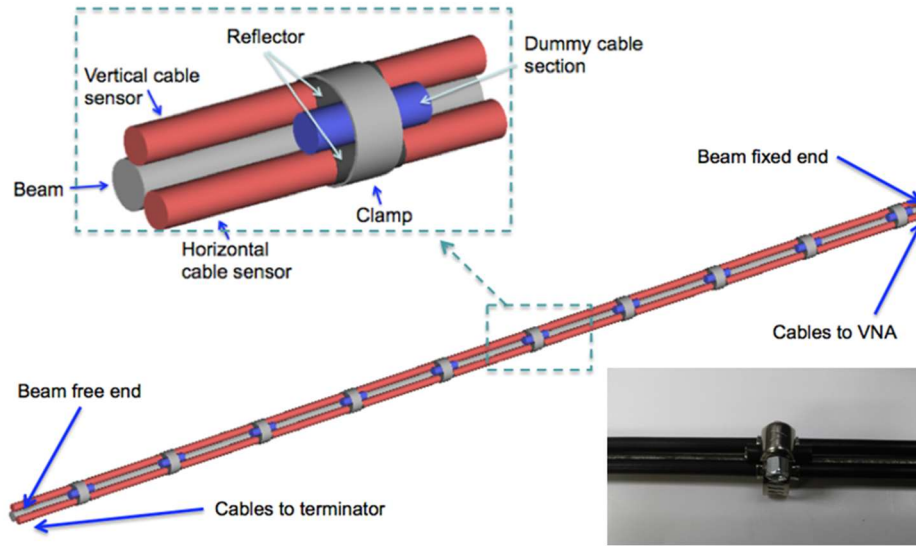
Figure 6.3. Sensor structure and arrangement.

In our experiment, 10 reflectors are embedded on each cable, forming 9 sections of virtual Fabry-Perot cavities. The length of each section is about 10cm. The beam under test is 1m long. When mounting the sensors, we tried to cover the beam with the cable from the fixed end, and left some space on the free end for the convenience of applying load. One end of the cable is connected to the port of VNA to acquire reflection signals, and the other end can be left open or connect to a terminator. The original data we get from the VNA is the reflection coefficient (S11 or S22) as complex number in the frequency domain. Using the joint-time-frequency domain demodulation method, the strain of each section between two adjacent reflectors can be obtained.

6.4 Single section strain response

We first measure the strain response of the sensors on the cable by fixing the cable on a tensile machine and record the spectra while applying strain. Using the aforementioned signal processing method, we are able to reconstruct the interference pattern of each sensor section. Here, we choose the section between the 4th and the 5th reflector as an example to study the strain response of one section of the sensor.

Figure 6.4(a) shows the spectrum dip near 3.3 GHz of the reconstructed interference pattern that shift with the applied strain. With the strain increased from 1mε to 8mε, the dip shifts towards the lower frequency by about 22 MHz. The whole spectra shift is shown in Fig. 5(a) inset. The frequency of the minimum point of the dip is plot against applied strain in Fig. 5(b). A linear regression is applied and the slope is found to be 3.768 MHz/mε with R2=0.9975. This means a 0.114% relative frequency shift per mε for this section. Apply this analysis to all the 9 sections, the relative frequency shifts per mε of the 9 sections range from 0.063% to 0.114%, and the average relative frequency shift is 0.085% per mε.

According to equation (6.2), if the dielectric constant remains the same, the relative frequency shift $\Delta f/f$ should be the same value with the relative length change of the cavity, which is the strain. This means that the relative frequency shift should be 0.1% per mε. The measured average relative frequency shift is 0.085%, lower than the 0.1% theoretic value. This means that we need to take into account the dielectric constant change. From equation (6.1), a change in the peak frequency can be represented by

$$\Delta f_m = \frac{\partial f_m}{\partial L}\Delta L + \frac{\partial f_m}{\partial \varepsilon_r}\Delta \varepsilon_r = -f_m \frac{\Delta L}{L} - \frac{1}{2}f_m \frac{\Delta \varepsilon_r}{\varepsilon_r}$$

This means that the relative frequency shift is

$$\frac{\Delta f_m}{f_m} = -\frac{\Delta L}{L} - \frac{1}{2}\frac{\Delta \varepsilon_r}{\varepsilon_r}$$

So a strain induced dielectric constant change will actually influence the measured strain value.

At the same time, we can actually observe a large strain response difference between the sections on the same cable. In our opinion, this is maybe due to the unbalanced reflections from the reflectors, which induce some distortion in the spectrum. It is hard to make the cavities to have the same strain sensitivity, so we need to calibrate each section of the sensors before use.
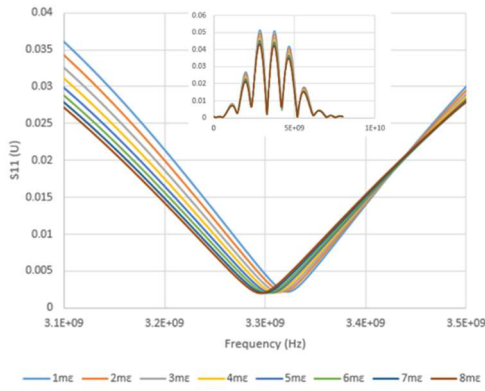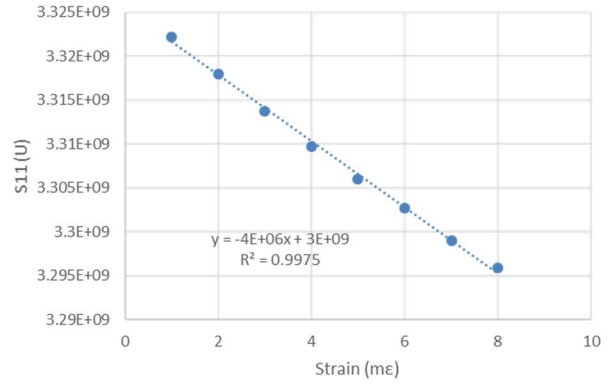
(a)   (b)

Figure 6.4. (a) Spectrum shift and (b) dip minimum point frequency change with applied strain.

In the frequency domain, although the separation between two sampling points is about 600 kHz, we can always use curve fitting and interpolation to improve the accuracy when we try to find the minimum point of the dip. So the real limitation on the accuracy of finding the dip frequency lies in the system stability. Figure 6.5 shows the experiment

96

result of the measured dip frequency of a stationary coaxial cable cavity. The measurement is done every 5 seconds for 100 points. Here, the average value of the dip frequency is 3.30 GHz, and the standard deviation is 50.95 kHz, about 1.5*10-5 of the dip frequency value.
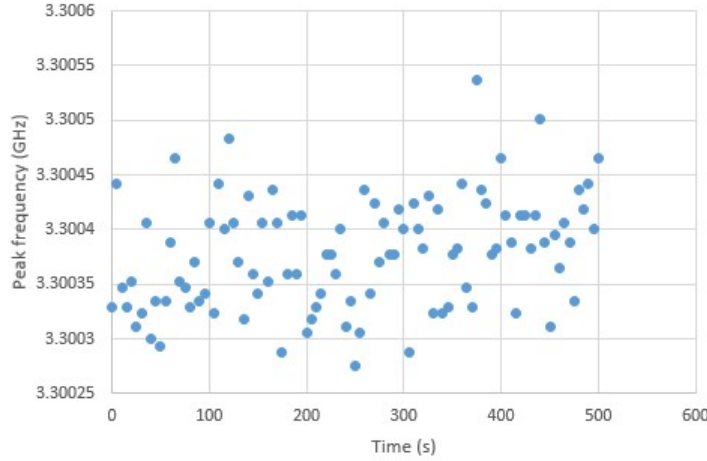
Figure 6.5. Stability of the dip frequency of a stationary coaxial cable cavity.

6.5 Strain distribution measurement on a beam under load

To verity the strain distribution measured by the system, a load is applied in the z-axis direction at the free end of the beam, and the strain data from the top sensor is recorded. We can easily calculate the bending momentum distribution along the beam, which is linearly distributed with the maximum bending momentum M_max=FL at the fixed end, and 0 bending momentum at the free end, where F is the load applied, and L is the total length of the beam.

From Flexural formula[25], we have

$$\varepsilon_x E = \sigma_x = \frac{-Mz}{I}$$

Which gives

$$\varepsilon_x = \frac{\Delta f}{f} = -\frac{Mz}{IE}$$

where E is the Young's modulus of the beam's material, M is the bending momentum at the measurement point, I is the Momentum of Inertia of the beam, for circular beam, I=πd^4/64; z is the position of the sensor in z direction away from the neutral plane, for circular beam, z=d/2. This formula shows the relationship between the sensor response and the bending momentum on the beam. According to the measured slope value in the previous section, factors ranging from 0.63 to 1.14 are applied on each section to make them represent the strain value. As the cables are fixed on the beam, the effective Young's modulus of the beam is a little different from the material's original value, and we can calibrate it with a specific load. After the calibration, the calculated and the measured strain are shown in Figure 6.6, when different loads of 2.97N, 4.02N and 5.45 N are applied respectively. From the figure, we can clearly see the linear strain distribution along the beam from the measurement when load is applied at the free end.
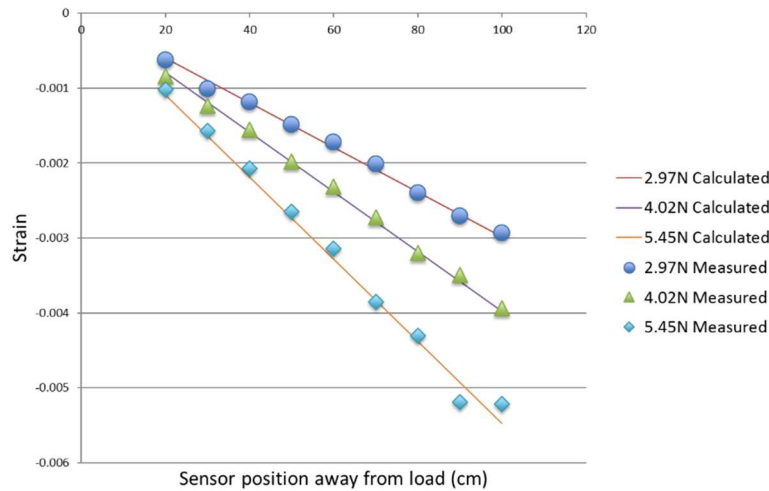
Figure 6.6. Measured and calculated strain with one cable sensor under different loads applied at the end of the beam.

Figure 6.7 (a) and (c) shows the measured strain distribution when loads are applied at different location on the beam. Figure 6.7 (b) and (d) are the pictures taken in the experiment of distributed strain measurement using the system. Here, only one cable is fixed at the bottom of a cantilever beam and the measured strain distribution is shown in the monitor screen with the red curve in the pictures. (a) is the measurement result when a simple load going upwards is applied at the free end of the cantilever, (b) is the picture taken under this load. In this situation, the strain should be linearly increased long the beam, and we can see that the measurement result agrees with this pattern qualitatively. (c) is the measured strain distribution when one load is applied in the middle, pushing down, while another small load is applied at the free end, pulling up, and (d) is the picture taken under this load. In this situation, the biggest strain should occur at the middle point where the load is applied, and linearly change towards the two ends. We can again see that the measurement result agrees with this pattern qualitatively.
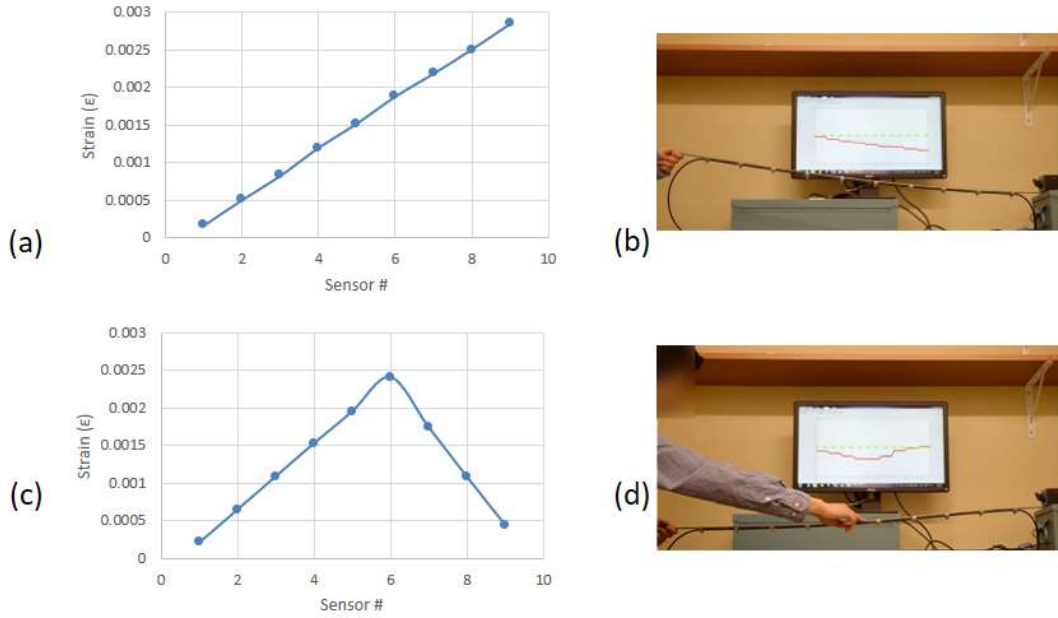
Figure 6.7. Strain distribution measured by cable sensor under different loads.

6.6 Transform from strain distribution to beam shape

The next step is to transform the measured strain data into the beam shape. Equations (6.5) and (6.6) represents the relationship between strain and displacement in theory. In real applications, such as the experiment here, we do not have continuous strain data, but discrete data points along the beam, so we cannot use direct integration. In discrete form, Equations (6.5) and (6.6) become,

$$y[i] = \frac{1}{r}\sum_{n=1}^{i}\left(\sum_{m=1}^{n}\varepsilon_{top}L_m\right)L_n \qquad (6.7)$$

$$z[i] = \frac{1}{r}\sum_{n=1}^{i}\left(\sum_{m=1}^{n}\varepsilon_{side}L_m\right)L_n \qquad (6.8)$$

If the measured strain data along the beam is dense enough, each section of the cable sensor can be approximated as a straight line, and the beam shape can be expressed

as connections of these straight lines, which can be calculated from Eq. (6.7) and (6.8). Alternatively, we can assume each section to be a curve with radius of curvature of ρ, the radius of curvature of the nth section ρ_n can be calculated from its measured strain by $\rho\_n = \varepsilon\_n/r$ based on Eq. (6.3), where r is the radius of the round beam. The shape of the beam can then be expressed by ρ_n and the length of each section L_n. We can also use curve fitting and interpolation to calculate more strain values along the beam. Here, we have 9 strain values as the distributed data. We can interpolate it so that we have much more data points, which helps to produce a smoother shape reconstruction.

With this method, an example of the transform is shown in Figure 6.8 and Figure 6.9. Figure 6.8 is the measured distributed strain data from the top and right side cable sensor, both including 9 sections. Figure 6.9 is the reconstruction result of the beam shape and shown in 3D view as well as 3 orthographic views. The calculation of the reconstruction is done in Matlab. There are many researches done on the strain-shape-transformation algorithms [45][46][47], and they can also be used with this sensor system for different applications. It is worth noting that we should choose the algorithm according to the application situation, such as small deflection, large deflection or dynamic shape monitoring. Some algorithms are only efficient in specific situations.
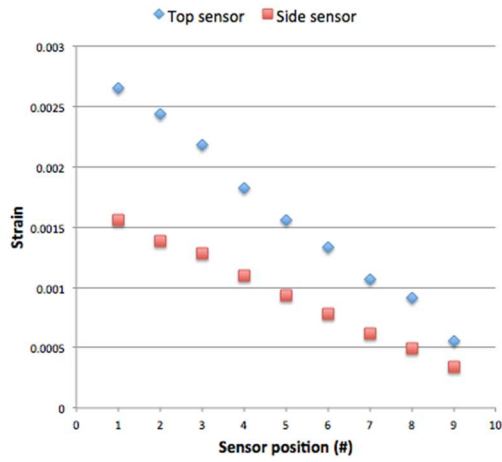
Figure 6.8. Measured strain data from the two cables.
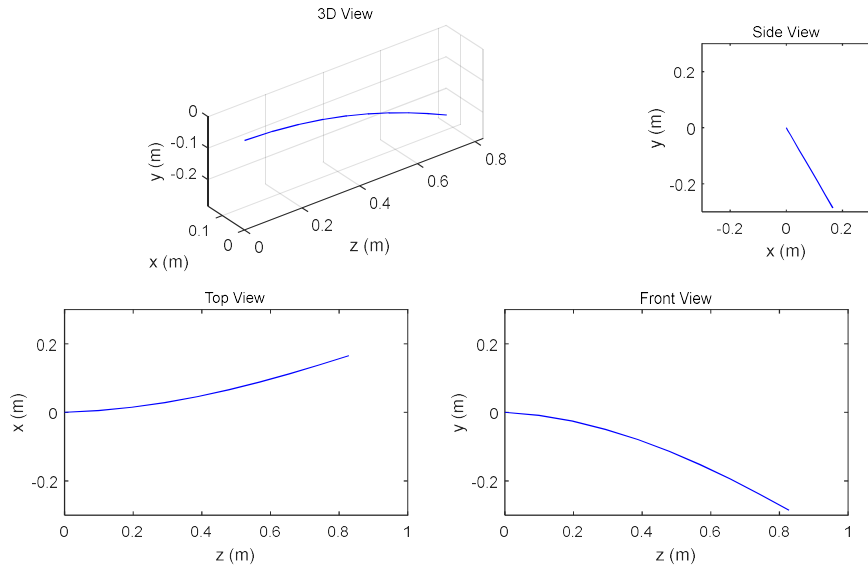
Figure 6.9. The reconstructed beam shape from the strain data on the two cables in different views.

A beam shape monitoring test is done with this system. In our experiment, with 10001 sampling points, 6 GHz bandwidth and 1kHz IF bandwidth, the total time for one

cycle of measurement is about 5 seconds. The data processing and the shape reconstruction takes very little time in computer, less than half second. The most time consuming part of this system is the data acquisition from VNA and the data transmission from VNA to the computer. Any method of reducing the data acquisition time, such as reducing the sampling rate or increase the IF bandwidth, can help to reduce the response time of the system.

To evaluate the performance of the sensor, a beam end position experiment is performed. In this experiment, one end of the 1-meter-long beam is fixed, while the other end is attached to a x-y translation stage to allow controlled bending in two dimensions. The last reflector on the beam is very close to the beam end. Before the test, the beam is bent in each direction to have 1cm displacement at the beam end, and we calibrate the system to obtain the factors that make the calculated position to be also 1cm in both directions. In the experiment, the beam is first bent in the x-z plane, and the position of the beam end is controlled to be from 0cm to 17.5cm, with a step separation of 2.5cm. After each step, the calculated beam end position in x and y direction is recorded, and the result is shown in Figure 6.10(a). After this, the beam is returned to the original position, and then bend in the y-z plane. Still, the beam end is controlled to be from 0cm to 17.5cm position with step of 2.5cm, and the calculated beam end position in x and y direction is recorded, as shown in Figure 6.10(b). When bending in x-z plane, the average position error in x direction is 0.249cm, and the average relative position error in x direction is 2.98%. In y direction, the value has an average error of 0.071cm from 0. When bending in y-z plane, the average position error in x direction is 0.296cm, and the average relative

position error in x direction is 3.70%. In x direction, the value has an average error of 0.069cm from 0.
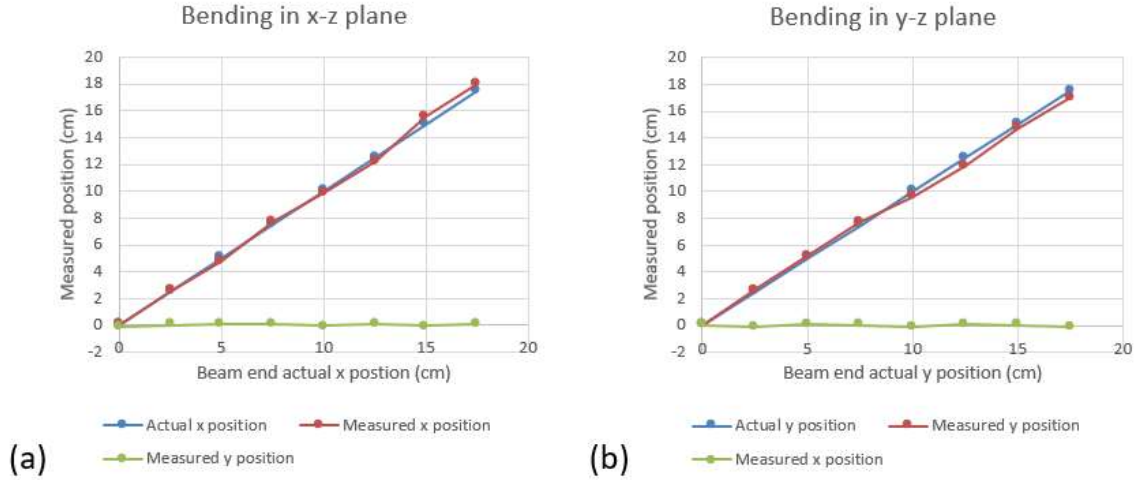
Figure 6.10. Beam end position experiment result when the beam is bent in a controlled manner. (a) Beam bent in the x-z plane, (b) beam bent in the y-z plane.

In our system, we use two orthogonal positioned cables to measure the distributed strain data. Usually, two channels of data from the cables are enough to reconstruct the beam shape. In some of the other works that use fiber optic sensors for shape reconstruction [26][27], three fibers are used, but the third fiber is redundant and only for temperature compensation. In some other cases, the third channel of signal is for torsion measurement [28]. In the case that a longitudinal strain exists on the beam, all the cables will experience an offset in the strain. To solve this problem, a fourth cables can be included to realize true differential strain measurement. In situations where torsion and longitudinal strain are not considered, two channels of data are enough for beam shape reconstruction. To solve the temperature crosstalk problem, we can add a relaxed sensor

section on the cable, which will respond to environment temperature but not influenced

by the strain.

Because the beam shape is calculated from the distributed strain data, the shape accuracy

is also determined by the measurement accuracy of the strain. Assume that the

measurement deviation of the strain is $\Delta\varepsilon$, and the induced shape deviation is Δy , From

equation (6.5), the shape deviation can be expressed by

$$\Delta y(x) = \frac{1}{r}\int_0^x \int_0^x \Delta\varepsilon_{top}(x)dx^2$$

Divide both sides by equation (6.5) again, we have

$$\frac{\Delta y(x)}{y(x)} = \frac{\frac{1}{r}\int_0^x \int_0^x \Delta\varepsilon_{top}(x)dx^2}{\frac{1}{r}\int_0^x \int_0^x \varepsilon_{top}(x)dx^2} = \int_0^x \int_0^x \frac{\Delta\varepsilon_{top}(x)}{\varepsilon_{top}(x)}dx^2$$

Here, $\frac{\Delta y(x)}{y(x)}$ is the relative shape error at location x, and $\frac{\Delta\varepsilon_{top}(x)}{\varepsilon_{top}(x)}$ is the relative

measurement error of the strain on the top of the beam. Equation (6.9) shows that the

error of the shape reconstruction will accumulate along the beam, and the farthest

position will have largest error. It also shows that at the same position, the relative shape

error is directly proportional to the relative strain error.

In conclusion, a coaxial cable interferometer based distributed sensing system for

3D beam shape estimation is presented in this chapter. Multiple strain sensors can be

fabricated on the same coaxial cable, and the strain data along the cable can be measured

with a single scan from the connected VNA. The sensor elements on the cables are virtual

Fabry-Perot cavities created on the cables with simple tools. With sensors embedded on

them, two cables are mounted in vertical and horizontal position on the beam to obtain

strain data. The cables are arranged in proper position to eliminate the cross talk between the two series of sensors in the two different bending directions. By using the proposed signal processing method, the strain at each virtual Fabry-Perot cavity is measured. With displacement-strain transformation, the shape of the beam is reconstructed from the distributed strain data. Consisting of only two modified cables and a VNA, this system is easy to implement, and suitable for beam shape monitoring. With the proposed system, we demonstrated its ability to reconstruct the beam shape in 2-axis bending. It is always possible to add more cables into the system for more complicated applications such as shape sensing of structures with large surfaces.

CHAPTER SEVEN

VII.   COAXIAL CABLE MAGNETIC FIELD SENSOR BASED ON FERROFLUID

FILLED FABRY-PEROT INTERFEROMETER STRUCTURE

7.1 Introduction

[55]Ferrofluid is a type of stable colloidal suspension with single domain

magnetic nanoparticles that dispersed uniformly in a liquid carrier [56][57]. When

exposed to external magnetic field, the nanoparticles inside the ferrofluid will be

rearranged, resulting in properties change of the solution such as refractive index and

absorption coefficient of electromagnetic radiation [58]. Based on its unique properties, a

lot of magnetic field sensors have been proposed. Among them, optical fiber based

ferrofluid sensors have attracted a lot of interests because of the advantage of compact

size and high sensitivity. Various configurations of fiber optics ferrofluid magnetic field

sensor has been reported, such as singlemode-multimode-singlemode (SMS) structure

[59], tapered microstructed optical fiber [60], asymmetric optical fiber taper [61], and

fiber Fabry-Perot interferometers [62], etc.

Recently, we reported the use of coaxial cable for sensor development. As a low

loss waveguide that transmit radio frequency electromagnetic waves, coaxial cables have

many similarities to optical fibers, because they share the same electromagnetic

cylindrical waveguide theory. Hence, a lot of fiber optics based devices can be migrated

on coaxial cables, such as coaxial cable Bragg gratings [63], coaxial cable Fabry-Perot

interferometers (FPI) [9]. Sensors such as temperature [64], strain [32] and torsion

sensors[15] have also been developed. Physically, coaxial cables are more robust than fibers, making them more suitable for large strain and heavy-duty applications. Different from optical signal, the phase of microwave signals that transmit on the coaxial cables can be easily obtained from commercially available equipment, such as vector network analyser (VNA). With the help of Fourier transform, people can obtain and manipulate both the time domain and frequency domain microwave signal, which offers distributed sensing capability to coaxial cable sensing platform [33].

In this paper, we propose a ferrofluid filled coaxial cable FPI sensor for magnetic field measurement. This sensor is capable of measuring static magnetic field, and has a linear response between 50 Gauss to 160 Gauss, with the sensitivity of 459 kHz/Gauss. Integrated on the coaxial cable sensing platform, it will be a good sensor head for remote and distributed magnetic field sensing applications.

7.2 Principle of ferrofluid filled coaxial cable cavity

The structure of the sensor is shown in Figure 7.1. A coaxial cable consists of the inner conductor, outer conductor and the dielectric layer. By removing a small section of dielectric layer in the cable, an air cavity is created inside the cable. A small hole is drilled on the top of the outer conductor, which is used to fill in the ferrofluid, then sealed with tapes. After filling, the interface of the dielectric material and the ferrofluid will act as reflectors, forming a Fabry-Perot (F-P) cavity. Suppose that the reflection coefficient at the two interfaces are equal, when a microwave signal is launched into the cable, the reflected signal at the two interfaces can be expressed as,

$$U_1 = \Gamma\cos(2\pi ft)$$

$$U_2 = \Gamma\cos[2\pi f(t + \tau)]$$

And $\tau = \frac{2d\sqrt{\varepsilon_r}}{c}$.

where Γ is the reflection coefficient of the interfaces, f is the microwave frequency, τ is the time delay between the two interfaces of the Fabry-Perot cavity, d is the length of the cavity, ε_r is the effective dielectric constant of the ferro-fluid filled cavity.
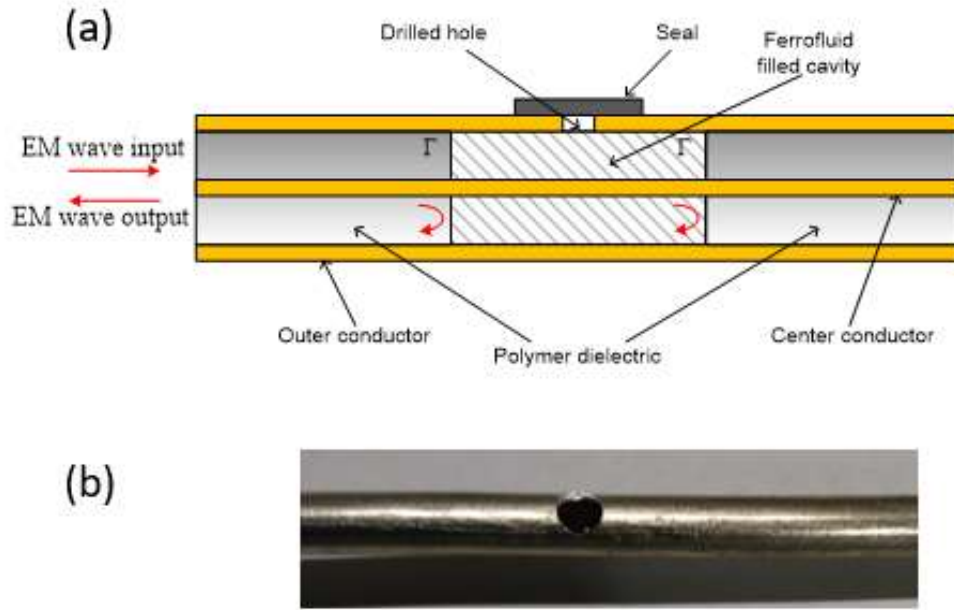
Figure 7.1. (a) Schematic of the ferrofluid filled coaxial cable sensor. (b) Picture of the sensor (before sealing).

The total reflection signal is the superposition of the 2 reflected signal from the two interfaces of the Fabry-Perot cavity, and can be expressed as,

109

$$U = 2 \cdot \Gamma \cos(\pi f \tau) \cos[2\pi f (t + \tau/2)] \qquad (7.1)$$

This means that the amplitude and the phase of the reflected signal are related to the

frequency of the microwave (f) as well as the time delay of the Fabry-Perot cavity (τ).

The spectrum of the reflected signal will exhibit sinusoidal wave in amplitude as an

interference pattern, and frequencies of the interference peaks/valleys are,

$$f_N = \frac{N}{\tau} = \frac{Nc}{2d\sqrt{\varepsilon_r}}$$

Where $N = 1,2,3, ...$

When the spectrum shifts due to the cavity property change, the relative frequency shift is

$$\frac{\Delta f_N}{f_N} = -\frac{\Delta d}{d} - \frac{1}{2}\frac{\Delta \varepsilon_r}{\varepsilon_r} \qquad (7.2)$$

Because ε_r of the ferrofluid is related to external magnetic field B, when an

external magnetic field is applied, the relative frequency shift of the Nth peak/valley is

$$\frac{\Delta f_N}{f_N} = -\frac{1}{2}\frac{\Delta \varepsilon_r(B)}{\varepsilon_r(B)} = -\frac{\Delta n}{n} \qquad (7.3)$$

Where n is the effective refractive index of the cavity.

7.3 Sensor fabrication and time domain characteristic

A semi-rigid cable (CrossRF SR-250) is used to fabricate the ferrofluid filled

coaxial cable Fabry-Perot interferometer. The outer and inner diameter of the outer

conductor are 6.35 mm and 5.31 mm respectively, and the diameter of the center

conductor is 1.628 mm. The dielectric material is PTFE. We first pull the outer conductor

away from the semi-rigid cable. A section of the polymer dielectric material of about 7

cm is cut away from the cable After that, we put the outer conductor back, and an air

cavity is created. At the center of the air cavity, a hole of about 2mm is drilled on the

outer conductor. The ferrofluid (FerroTec EMG909) is filled into the cavity by syringe.

After the filling, the hole is sealed with multiple layers of tapes to prevent leakage. This

sensor is then connected to the port 1 of a vector network analyzer (VNA). After reading

out the S11 information both in magnitude and phase, a complex inverse Fourier

transform is performed and we can obtain the time domain reflection (TDR) signal. On

the VNA, the frequency span is set from 6 GHz to 12 GHz, the IF bandwidth is set to 5

kHz, and the total sampling points is 16001.

The TDR signal of the sensor before and after filling the ferrofluid is shown on

figure 7.2(a). The blue curve is the TDR before filling. The two reflections of the Fabry-

Perot cavity are at time of 2.50 ns, and 2.95 ns with the reflection coefficient of 0.20109

and 0.14247. The third reflection at 5.54 ns is caused by the open end of the cable.

(a)
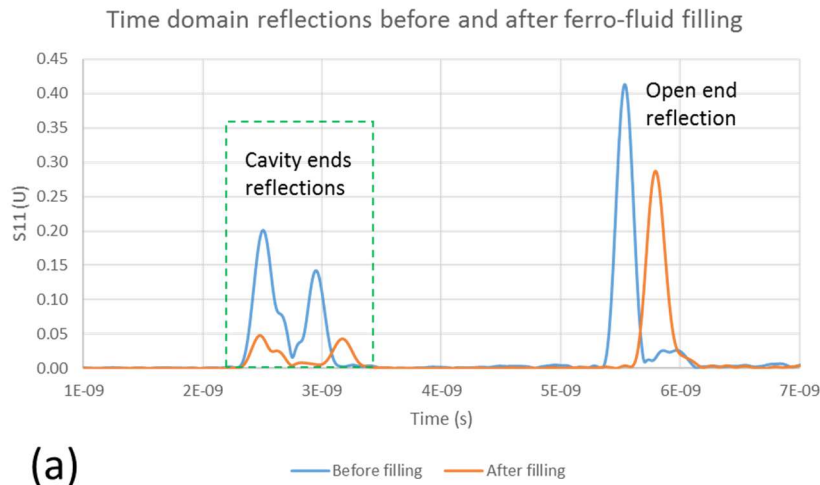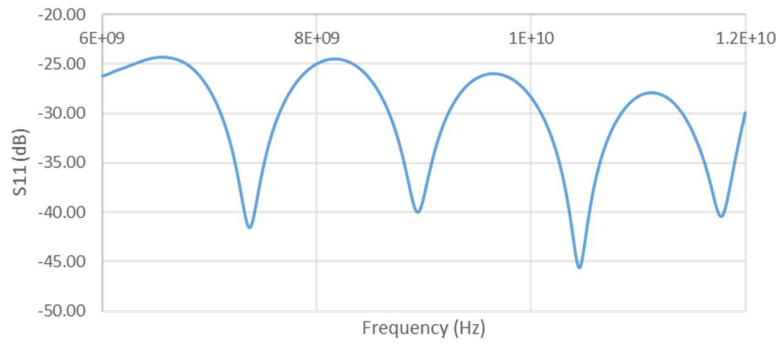
(b)

Figure 7.2. (a)Time domain reflection signal of the sensor, and (b)Reconstructed interference spectrum of the Fabry-Perot cavity.

The red curve is the TDR after filling the ferrofluid into the cavity. The two reflections of the Fabry-Perot cavity are at time of 2.48 ns, and 3.17 ns with the reflection coefficient of 0.04788 and 0.04312. The new open end reflection peak is at 5.79ns with reflection coeffeicition of 0.28714. After the ferrofluid filling, the reflections decreased from about 20.1% and 14.2% to 4.8% and 4.3% respectively. The reflection on the open end also drop from about 41.3% to 28.7%. There are two reasons for the decrease of the reflection intensity. The first reason is the decrease in refractive index contrast. The reflection coefficient between two sections of coaxial cables is determined by the contrast of the characteristic impedance, which is in turn in proportion to the contrast in refractive index. Before filling the ferrofluid, the contrast is between the cable material and air. After filling, the contrast is between the cable material and the ferrofluid, which is much smaller. This will result in the decrease of reflection intensity at the cavity ends. The second reason is that the ferrofluid will introduce some transmission loss, which will

result in reflection intensity drop at the interfaces after the cavity. The reflection peak position that comes after the cavity also changed significantly. Comparing to the TDR before filling, the time delay between the two peaks of the cavity interfaces is increased about 0.24 ns, and the open end reflection peak is delayed about 0.25 ns. Since the cavity length keeps the same, this delay change is induced by the effective refractive index of the ferrofluid. From the contrast of the peak position in the time domain, we can see that the filled ferrofluid introduced an effective index of 1.53.

The next step is to use a gating window to isolate the two reflectors in time domain, suppressing the other reflection signal. This gating window is shown as a green dotted rectangular in figure 7.2(a). A Fourier transform is then performed on the gated time-domain signal to convert it back to frequency domain. This technique comes from the joint-time-frequency domain demodulation method, which is the method to realize the distributed sensing capability in cascaded coaxial cable Fabry-Perot interferometry. The details of this technique can be found in [33]. After the transformation, the interference spectrum of the Fabrt-Perot cavity is obtained in frequency domain. Because the interfaces of the cavity are not perfectly created reflectors, and the intensity of the two reflections are not balanced, the resulted spectrum is not a pure a sinusoidal wave as in Equation (7.1), but with a little distortion as shown in Figure 7.2(b). Despite of the distortion, when the cavity property change, the spectrum will still shift according to Equation (7.2).

7.4 Measurement of magnetic field

Figure 7.3 shows the experiment setup and procedure for testing the response of the sensor to external magnetic field. The cable is connected to the VNA, and a bar magnet is positioned near the Fabry-Perot cavity on the cable to create a magnetic field. A Gauss meter is used to read the field strength, and the probe tip is placed close to the Fabry-Perot cavity. By moving the bar magnet's position, different magnetic field strength from about 0 Gausss to 160 Gausss is created near the sensor, and the frequency domain complex S11 signal is recorded at each field strength. The highest magnetic field the sensor works is limited by the saturation magnetization of the ferrofluid, which is 220 Gauss±10%.
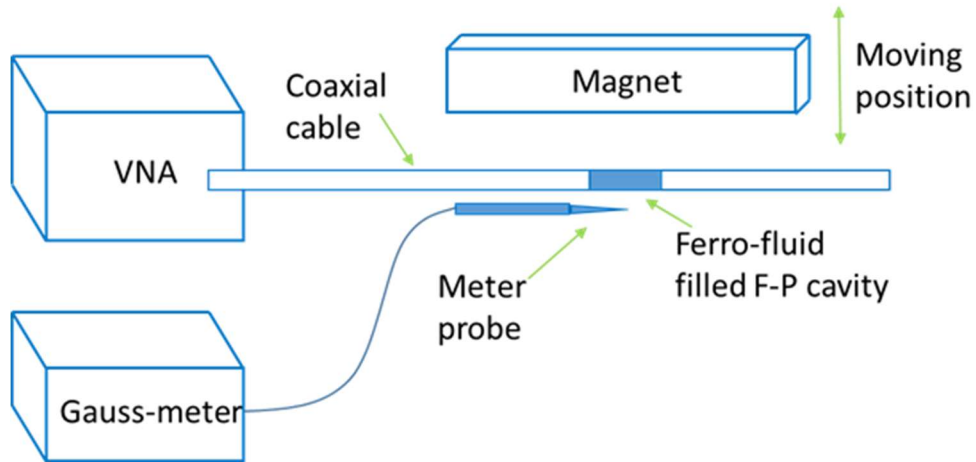
Figure 7.3. Schematic of the experiment setup for magnetic field measurement.

We first transform the complex S11 signal to time domain and study the change of the peak intensities of the two interfaces of the cavity. In the experiment, the magnetic field is first increased, then decreased. The intensity change is shown in Figure 7.4.
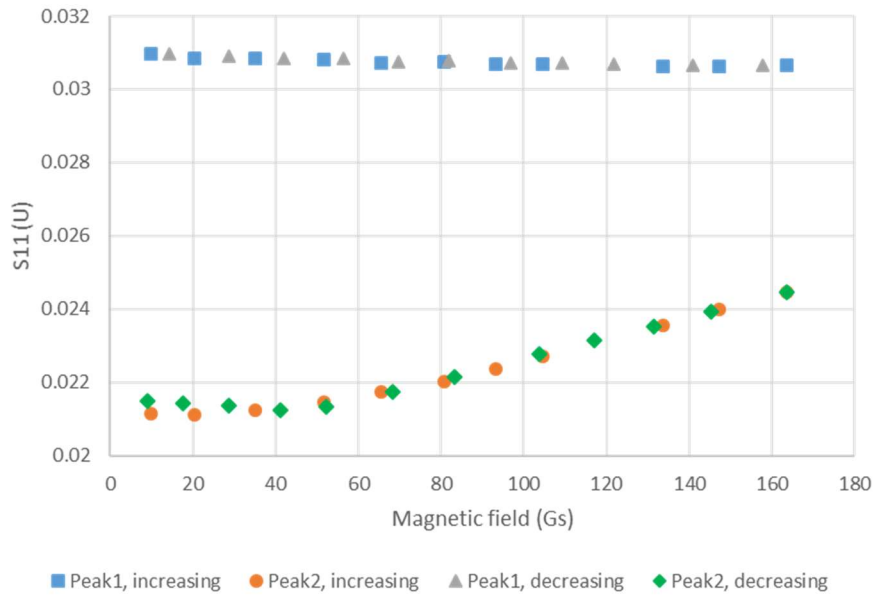
Figure 7.4. The reflection intensity of the two cavity interfaces during the process of increasing and decreasing the magnetic field.

From the figure we can see that the reflection intensity of the first interface does not change too much, but the reflection intensity of the second interface increase with the increased magnetic field. There are two possible reasons for the increasing of the intensity: the first is the magnetic field induced refractive index change of the ferrofluid, the second is magnetic field induced microwave absorption change of the ferrofluid. If the dominating reason is the refractive index change, then the intensity from both interfaces should increase, which is not happening. So the intensity change mainly comes from the microwave absorption change. As the external magnetic field increase, the increasing reflection intensity indicates that the microwave absorption is decreased. This

is maybe due to the abnormal permeability behaviour in microwave frequency for ferromagnetic nanoparticles [65][66][67].

From Equation (7.3) we can see that each dip on the spectrum will respond to the magnetic field, with slight different sensitivity according to the peak frequency. Figure 7.5 shows the whole spectrum shift when the magnetic field is changed from 0 Gauss to about 160 Gauss. We choose the dip near 9 GHz and plot the spectra near that frequency in Figure 7.5. As we discussed previously, the intensity of the second reflection increases with the magnetic field, making the intensity of the two reflection more balanced. As a result, the fringe visibility of the interference spectrum also increased from 13 dB to 17 dB at the 9 GHz dip. The frequency of the dip is determined by finding the smallest value of the spectrum near 9 GHz. To increase the accuracy, curve fitting and interpolation is used. The dip frequency shift with the change of the magnetic field is shown in Figure 7.6. The magnetic field is first increased from 3 Gauss to 164 Gauss, then decreased to 4 Gauss. The figure shows that from 50 Gauss on, the relationship between the dip frequency and the magnetic field is very linear, and the sensitivity is about 459 kHz/Gauss. Calculated from the data, the refractive index change of the ferrofluid with the magnetic field strength is about $\Delta f/f = -\Delta n/n = 0.51\%$ per 100 Gauss, larger than the 0.3% change per 100 Gauss value in optical frequency that was reported in [62].
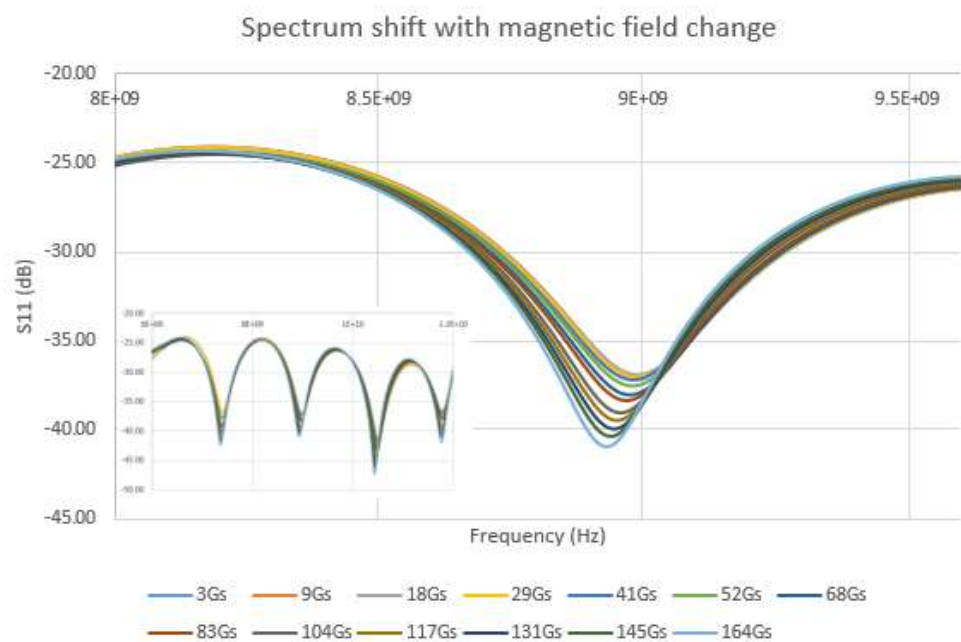
Figure 7.5. Frequency dip near 9 GHz shifts with magnetic field increase. Inset:

Complete spectrum (6 GHz to 12 GHz) shift.
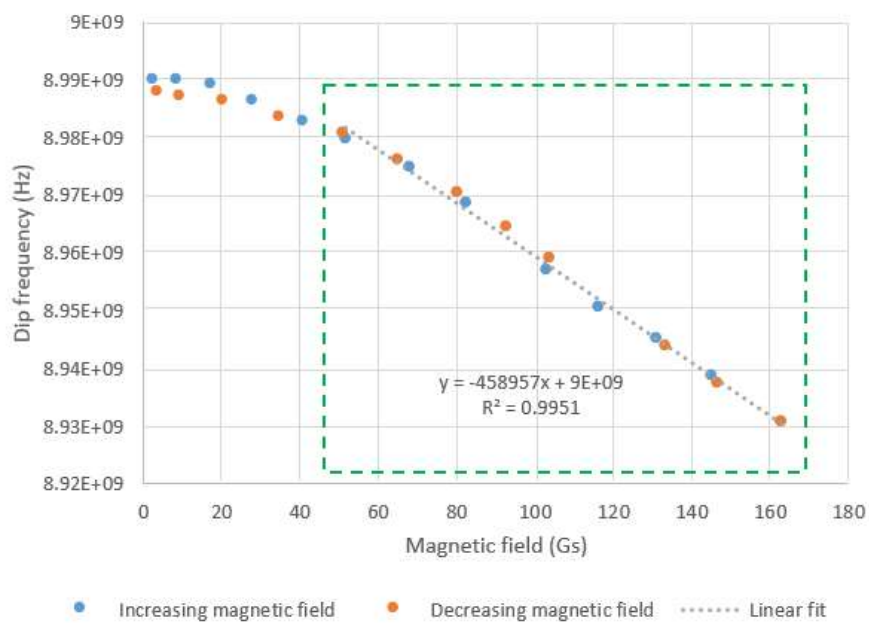
Figure 7.6. Dip frequency shifts with the process of increasing and decreasing the magnetic field.

In the experiment, the frequency span is 6 GHz, and the maximum sampling points from the VNA is 16001, so the minimum frequency separation between to sampling points is 0.375 MHz. However, we can find spectrum dip with higher accuracy by curve fitting and interpolation in the spectrum. From our understanding, the real limitation on the measurement accuracy lies in the stability of the measured spectrum by the VNA, which is influenced by the instrument itself. This stability is usually about 10-5 according to our experience. So the stability of spectrum at about 9 GHz is 90 kHz, which is 0.196 Gauss in the magnetic field measurement. Note that the IF bandwidth in the experiment is set to 5 kHz, but we cannot achieve that accuracy, because the 90 kHz spectrum stability limit is much larger than it. Temperature crosstalk is also a problem that can influence the sensor performance of the sensor. Temperature variation can change the cavity length with thermal expansion, which induce the Δd to occur in Equation (2), and the refractive index of the ferrofluid may also change with temperature. A solution to it is to cascade another Fabry-Perot cavity on the sensor to compensate the thermal expansion part, and the refractive index part can be calculated using RI-temperature coefficient of the ferrofluid, which can be characterized in other experiments.

The proposed magnetic field sensor is based on coaxial cable, which is also a transmission line, making it a good remote sensor. If integrated with other kinds of

coaxial cable sensors, multi-function remote sensing can be fulfilled on this platform. If cascaded on a single cable, it also has the potential to realize distributed magnetic field sensing. However, the sensor currently has about 30% insertion loss, which will limit the number of sensors that can be cascaded. In the future work, we will try to improve the design of the sensor to reduce the loss.

In conclusion, we propose a ferrofluid filled coaxial cable Fabry-Perot interferometer for magnetic field sensing. The Fabry-Perot cavity is created by cutting away a section of the dielectric material in a semi-rigid coaxial cable, then inject ferrofluid into it. The interferogram of the Fabry-Perot cavity shifts with the external magnetic field because of the refractive index change of the ferrofluid, and the reflection intensity of the cavity interface also change because of the microwave absorption change. The sensor is tested to work from 0 Gauss to 160 Gauss, and has a highly linear response above 50 Gauss, with sensitivity of 459 kHz/Gauss. The spectrum stability is 90 kHz, so the measurement accuracy can be 0.196 Gauss in theory. Based on coaxial cable platform, this magnetic field sensor is good for remote sensing and has the potential for distributed magnetic field sensing applications.

CHAPTER EIGHT

VIII. CONCLUSION AND FUTURE WORK

8.1 Conclusions

In this dissertation, we studied the CC-FPI based sensors and their applications. Like fiber optic sensors, coaxial cable sensors are suitable for distributed sensing. The main problem of fiber sensors is the lack of robustness: they are easy to break and have very low strain limitation. For harsh environment and heavy duty applications, coaxial cable sensors have their unique advantage while keeping the strength of long distance distributed sensing capability.

The principle of coaxial cable FPIs is discussed at the beginning of the thesis. The spectrum changes of the sensor with regard to environment such as temperature and strain is studied. The property of the cable materials and dimensions also have influence on the sensitivity of the sensor. The joint-time-frequency domain demodulation method can be used to realize distributed sensing when multiple FPIs are cascaded on a cable. This is used for two applications: distributed torsion sensing and 3D beam shape estimation. For the distributed torsion sensor, the torsion on the shaft is converted to the strain of the cable by arranging the cable around the shaft in spiral form. This sensor has potential applications in petroleum industry. The 3D beam shape sensor consists of two cascaded CC-FPI sensor cables, arranged along a beam in orthogonal position to measure the strain distribution of the beam in the cross section plane. Displacement-strain transformation (DST) is then used to reconstruct the shape of the beam.

It is also possible to modify the cable itself to achieve special function for CC-FPIs. The first example is the metal ceramic coaxial cable that is fabricated in lab for high temperature sensing. The reflectors that forming the FPI are dielectric thin disks or just air gaps. The conductors and dielectric materials are chosen to be able to survive high temperature, while their dimensions are designed to be able to transmit power and signals effectively to instruments. Different materials are tried and different reflector structures are studied. The resulted metal ceramic coaxial cable FPI sensor is tested and can survive up to 900 C with good response. Another example is a magnetic field sensor based on ferrofluid filled coaxial cable FPI. Ferrofluid is a type of colloidal suspension that is dispersed with magnetic nanoparticles. The property of the ferrofluid will change when external magnetic field is applied. The sensor contains a hollow cavity in a semi-rigid coaxial cable, and the cavity is then filled with ferrofluid. The sensor is tested up to 160 Gauss and the response shows good linearity.

The CC-FPI sensors have the advantage of distributed sensing capability, and can be modified to measure different physical quantities. This dissertation demonstrated the principle and several applications of this kind of sensor, and it will have great potential to be a practical sensing tool in a lot other application fields.

8.2 Future work

This dissertation shows several applications of CC-FPI sensors. In fact, a lot of other sensors based on this principle is being developed, including chemical sensor based on Zeolite filled CC-FPI, liquid level sensor based on distributed hollow coaxial cable,

121

and bending sensor based on structure modified semi-rigid coaxial cable. Preliminary experiments have been done and they can all be developed into practical sensors. We believe that the coaxial cable sensing platform can be very useful when more kinds of coaxial cable based sensors are developed. Besides sensor development, the instrumentation system can also be improved in the future. Parameters such as spatial resolution, sensitivity and stability all needs to be further studied to give a better performance of this system. This can be done either by optimizing the instruments combinations and choosing proper parameters, or by improving the signal processing methods.

REFERENCE

[1]   K. T. V. Grattan and T. Sun, "Fiber optic sensor technology: an overview,"
        Sensors Actuators A Phys., vol. 82, no. 1–3, pp. 40–61, May 2000.

[2]   A. D. Kersey, T. A. Berkoff, and W. W. Morey, "Multiplexed fiber Bragg grating
        strain-sensor system with a fiber Fabry - Perot wavelength filter," *Opt. Lett.*, vol.
        18, no. 16, p. 1370, Aug. 1993.

[3]   K. Hill and G. Meltz, "Fiber Bragg grating technology fundamentals and
        overview," *J. Light. Technol.*, 1997.

[4]   M. Froggatt and J. Moore, "High-spatial-resolution distributed strain measurement
        in optical fiber with Rayleigh scatter," *Appl. Opt.*, 1998.

[5]   J. Dakin, D. Pratt, G. Bibby, and J. Ross, "Distributed optical fibre Raman
        temperature sensor using a semiconductor light source and detector," *Electron.
        Lett.*, 1985.

[6]   Y. Dong, L. Chen, and X. Bao, "Time-division multiplexing-based BOTDA over
        100 km sensing length.," *Opt. Lett.*, vol. 36, no. 2, pp. 277–9, Jan. 2011.

[7]   X. Bao and L. Chen, "Recent progress in distributed fiber optic sensors.," *Sensors
        (Basel).*, vol. 12, no. 7, pp. 8601–39, Jan. 2012.

[8]   J. Huang, T. Wei, S.-P. Wu, X.-W. Lan, J. Fan, and H. Xiao, "Coaxial Cable
        Bragg Grating Sensors for Structural Health Monitoring," *Int. J. Pavement Res.
        Technol.*, vol. 5, no. 5, pp. 338–342, 2012.

[9]   J. Huang, T. Wang, L. Hua, J. Fan, H. Xiao, and M. Luo, "A coaxial cable fabry-
        perot interferometer for sensing applications.," *Sensors (Basel).*, vol. 13, no. 11,

pp. 15252–60, 2013.

[10] F. Surre, T. Sun, and K. T. Grattan, "Fiber Optic Strain Monitoring for Long-Term Evaluation of a Concrete Footbridge Under Extended Test Conditionss," *IEEE Sens. J.*, vol. 13, no. 3, pp. 1036–1043, Mar. 2013.

[11] T. Kawanishi and M. Izutsu, "Coaxial periodic optical waveguide," *Opt. Express*, vol. 7, no. 1, p. 10, Jul. 2000.

[12] H.-N. Li, D.-S. Li, and G.-B. Song, "Recent applications of fiber optic sensors to health monitoring in civil engineering," *Eng. Struct.*, vol. 26, no. 11, pp. 1647–1657, Sep. 2004.

[13] Shishuang Sun, D. J. Pommerenke, J. L. Drewniak, Genda Chen, Liang Xue, M. A. Brower, and M. Y. Koledintseva, "A Novel TDR-Based Coaxial Cable Sensor for Crack/Strain Sensing in Reinforced Concrete Structures," *IEEE Trans. Instrum. Meas.*, vol. 58, no. 8, pp. 2714–2725, Aug. 2009.

[14] J. Huang, T. Wei, T. Wang, J. Fan, and H. Xiao, "Control of critical coupling in a coiled coaxial cable resonator," *Rev. Sci. Instrum.*, vol. 85, no. 5, p. 54701, 2014.

[15] B. Cheng, W. Zhu, L. Hua, J. Liu, Y. Li, R. Nygaard, H. Xiao, "Distributed torsion sensor based on cascaded coaxial cable Fabry–Perot interferometers," *Meas. Sci. Technol.*, vol. 27, no. 7, p. 75103, Jul. 2016.

[16] J. P. de Wardt, M. Behounek, C. Chapman, and D. Putra, "Drilling Systems Automation - Preparing for the Big Jump Forward," in *SPE/IADC Drilling Conference*, 2013.

[17] M. Zamora and G. Hildebrand, "Design Aid for Charting a Drilling Automation

Roadmap," in *SPE/IADC Drilling Conference*, 2013.

[18]   J. L. Thorogood, "Automation in Drilling: Future Evolution and Lessons from Aviation," in *IADC/SPE Drilling Conference and Exhibition*, 2013.

[19]   A. P. Pink, H. Kverneland, A. Bruce, and J. B. Applewhite, "Building an Automated Drilling System Where the Surface Machines are Controlled by Downhole and Surface Data to Optimize the Well Construction Process," in *IADC/SPE Drilling Conference and Exhibition*, 2013.

[20]   G. Hareland, R. Nygaard, and B. K. Virginillo, "Drilling Simulation versus Actual Performance in Western Canada," in *Rocky Mountain Oil & Gas Technology Symposium*, 2013.

[21]   E. H. M. Al Dushaishi, R. Nygaard, S. Hellvik, M. Andersen, "Post Well Vibration Analysis in the North Sea: A Tool to Understand Drilling Performance," in *OMAE2015*, 2015.

[22]   C. Raap, A. D. Craig, and D. Perez Garcia, "Understanding and Eliminating Drill String Twist-Offs by the Collection of High Frequency Dynamics Data," in *SPE/IADC Middle East Drilling Technology Conference and Exhibition*, 2013.

[23]   K. Miyashita, T. Takahashi, S. Kawamata, S. Moringa, and H. Yoshikazu, "Non contact magnetic torque sensor," *IEEE Trans. Magn.*, vol. 26, no. 5, pp. 1560–1562, 1990.

[24]   R. F. Wolffenbuttel and J. A. Foerster, "Noncontact capacitive torque sensor for use on a rotating axle," *IEEE Trans. Instrum. Meas.*, vol. 39, no. 6, pp. 1008–1013, 1990.

[25]   R. J. Hazelden, "Optical torque sensor for automotive steering systems," *Sensors Actuators A Phys.*, vol. 37–38, pp. 193–197, Jun. 1993.

[26]   K. Lee and C. Cho, "A Feasibility Study of a Noncontact Torque Sensor with Multiple Hall Sensors," *J. Sensors*, vol. 2015, p. 6, 2015.

[27]   Weigang Zhang, G. Kai, Xiaoyi Dong, Shuzhong Yuan, and Qida Zhao, "Temperature-independent FBG-type torsion sensor based on combinatorial torsion beam," *IEEE Photonics Technol. Lett.*, vol. 14, no. 8, pp. 1154–1156, Aug. 2002.

[28]   C. Shen, Y. Zhang, W. Zhou, and J. Albert, "Au-coated tilted fiber Bragg grating twist sensor based on surface plasmon resonance," *Appl. Phys. Lett.*, vol. 104, no. 7, p. 71106, Feb. 2014.

[29]   Y.-P. Wang, J.-P. Chen, and Y.-J. Rao, "Torsion characteristics of long-period fiber gratings induced by high-frequency CO2 laser pulses," *J. Opt. Soc. Am. B*, vol. 22, no. 6, p. 1167, Jun. 2005.

[30]   W. Chen, S. Lou, L. Wang, H. Zou, W. Lu, and S. Jian, "Highly sensitive torsion sensor based on Sagnac interferometer using side-leakage photonic crystal fiber," *IEEE Photonics Technol. Lett.*, vol. 23, no. 21, pp. 1639–1641, Nov. 2011.

[31]   W. Yiping, M. Wang, and X. Huang, "In fiber Bragg grating twist sensor based on analysis of polarization dependent loss.," *Opt. Express*, vol. 21, no. 10, pp. 11913–20, May 2013.

[32]   J. Huang, T. Wei, X. Lan, J. Fan, and H. Xiao, "Coaxial cable Bragg grating sensors for large strain measurement with high accuracy," *Spie*, vol. 8345, no. 5, p.

83452Z–83452Z–9, 2012.

[33]   J. Huang, X. Lan, W. Zhu, B. Cheng, J. Fan, Z. Zhou, and H. Xiao, "Interferogram Reconstruction of Cascaded Coaxial Cable Fabry-Perot Interferometers for Distributed Sensing Application," *IEEE Sens. J.*, vol. 16, no. 11, pp. 4495–4500, Jun. 2016.

[34]   B. Cheng, W. Zhu, J. Liu, L. Yuan, and H. Xiao, "3D beam shape estimation based on distributed coaxial cable interferometric sensor," *Smart Mater. Struct.*, vol. 26, no. 3, p. 35017, Mar. 2017.

[35]   J. J. Lee and M. Shinozuka, "Real-Time Displacement Measurement of a Flexible Bridge Using Digital Image Processing Techniques," *Exp. Mech.*, vol. 46, no. 1, pp. 105–114, Feb. 2006.

[36]   H.-I. Kim, J.-H. Han, and H.-J. Bang, "Real-time deformed shape estimation of a wind turbine blade using distributed fiber Bragg grating sensors," *Wind Energy*, p. n/a-n/a, Jul. 2013.

[37]   W. Akl, S. Poh, and A. Baz, "Wireless and distributed sensing of the shape of morphing structures," *Sensors Actuators A Phys.*, vol. 140, no. 1, pp. 94–102, Oct. 2007.

[38]   S. Rapp, L.-H. Kang, J.-H. Han, U. C. Mueller, and H. Baier, "Displacement field estimation for a two-dimensional structure using fiber Bragg grating sensors," *Smart Mater. Struct.*, vol. 18, no. 2, p. 25006, Feb. 2009.

[39]   T. H. T. Chan, D. B. Ashebo, H. Y. Tam, Y. Yu, T. F. Chan, P. C. Lee, and E. Perez Gracia, "Vertical Displacement Measurements for Bridges Using Optical

Fiber Sensors and CCD Cameras -- A Preliminary Study," *Struct. Heal. Monit.*, vol. 8, no. 3, pp. 243–249, May 2009.

[40]   G. A. Fleming and S. A. Gorton, "Measurement of rotorcraft blade deformation using projection moire interferometry," in *Third International Conference on Vibration Measurements by Laser Techniques: Advances and Applications*, 1998, pp. 514–527.

[41]   O. Schneider, "Analysis of SPR measurements from HART II," *Aerosp. Sci. Technol.*, vol. 9, no. 5, pp. 409–420, Jul. 2005.

[42]   Y. Fujino, M. Murata, S. Okano, and M. Takeguchi, "Monitoring system of the Akashi Kaikyo Bridge and displacement measurement using GPS," in *SPIE's 5th Annual International Symposium on Nondestructive Evaluation and Health Monitoring of Aging Infrastructure*, 2000, pp. 229–236.

[43]   M. Grédiac, "Method for surface reconstruction from slope or curvature measurements of rectangular areas," *Appl. Opt.*, vol. 36, no. 20, p. 4823, Jul. 1997.

[44]   C. Elster, J. Gerhardt, P. Thomsen-Schmidt, M. Schulz, and I. Weingärtner, "Reconstructing surface profiles from curvature measurements," *Opt. - Int. J. Light Electron Opt.*, vol. 113, no. 4, pp. 154–158, Jan. 2002.

[45]   R. Glaser, V. Caccese, and M. Shahinpoor, "Shape Monitoring of a Beam Structure from Measured Strain or Curvature," *Exp. Mech.*, vol. 52, no. 6, pp. 591–606, Jul. 2011.

[46]   M. Gherlone, P. Cerracchio, M. Mattone, M. Di Sciuva, and A. Tessler, "Shape sensing of 3D frame structures using an inverse Finite Element Method," *Int. J.*

Solids Struct., vol. 49, no. 22, pp. 3100–3112, Nov. 2012.

[47]   A. Derkevorkian, S. F. Masri, J. Alvarenga, H. Boussalis, J. Bakalyar, and W. L. Richards, "Strain-Based Deformation Shape-Estimation Algorithm for Control and Monitoring Applications," *AIAA J.*, vol. 51, no. 9, pp. 2231–2240, Sep. 2013.

[48]   Z.-C. Wang, D. Geng, W.-X. Ren, and H.-T. Liu, "Strain modes based dynamic displacement estimation of beam structures with strain sensors," *Smart Mater. Struct.*, vol. 23, no. 12, p. 125045, Dec. 2014.

[49]   J. Wu, C. Song, H. S. Saleem, A. Downey, and S. Laflamme, "Network of flexible capacitive strain gauges for the reconstruction of surface strain," *Meas. Sci. Technol.*, vol. 26, no. 5, p. 55103, May 2015.

[50]   W. Chung, S. Kim, N.-S. Kim, and H. Lee, "Deflection estimation of a full scale prestressed concrete girder using long-gauge fiber optic sensors," *Constr. Build. Mater.*, vol. 22, no. 3, pp. 394–401, Mar. 2008.

[51]   R. T. Jones, D. G. Bellemore, T. A. Berkoff, J. S. Sirkis, M. A. Davis, M. A. Putnam, E. J. Friebele, and A. D. Kersey, "Determination of cantilever plate shapes using wavelength division multiplexed fiber Bragg grating sensors and a least-squares strain-fitting algorithm," *Smart Mater. Struct.*, vol. 7, no. 2, pp. 178–188, Apr. 1998.

[52]   H.-I. Kim, L.-H. Kang, and J.-H. Han, "Shape estimation with distributed fiber Bragg grating sensors for rotating structures," *Smart Mater. Struct.*, vol. 20, no. 3, p. 35011, Mar. 2011.

[53]   M. Nishio, T. Mizutani, and N. Takeda, "Shape identification of variously-

deformed composite laminates using Brillouin type distributed strain sensing system with embedded optical fibers," in *The 15th International Symposium on: Smart Structures and Materials & Nondestructive Evaluation and Health Monitoring*, 2008, p. 69322P–69322P–9.

[54]   M. Nishio, T. Mizutani, and N. Takeda, "Structural shape reconstruction with consideration of the reliability of distributed strain data from a Brillouin-scattering-based optical fiber sensor," *Smart Mater. Struct.*, vol. 19, no. 3, p. 35011, Mar. 2010.

[55]   B. Cheng, L. Yuan, W. Zhu, Y. Song, and H. Xiao, "A coaxial cable magnetic field sensor based on ferrofluid filled Fabry-Perot interferometer structure," *Sensors Actuators A Phys.*, vol. 257, pp. 194–197, 2017.

[56]   S. W. Charles, "The Preparation of Magnetic Fluids," Springer Berlin Heidelberg, 2002, pp. 3–18.

[57]   T. Kruse, H.-G. Krauthäuser, A. Spanoudaki, and R. Pelster, "Agglomeration and chain formation in ferrofluids: Two-dimensional x-ray scattering," *Phys. Rev. B*, vol. 67, no. 9, p. 94206, Mar. 2003.

[58]   S. Y. Yang, Y. F. Chen, H. E. Horng, C.-Y. Hong, W. S. Tse, and H. C. Yang, "Magnetically-modulated refractive index of magnetic fluid films," *Appl. Phys. Lett.*, vol. 81, no. 26, p. 4931, 2002.

[59]   Y. Chen, Q. Han, T. Liu, X. Lan, and H. Xiao, "Optical fiber magnetic field sensor based on single-mode-multimode-single-mode structure and magnetic fluid.," *Opt. Lett.*, vol. 38, no. 20, pp. 3999–4001, Oct. 2013.

[60] M. Deng, C. Huang, D. Liu, W. Jin, and T. Zhu, "All fiber magnetic field sensor with Ferrofluid-filled tapered microstructured optical fiber interferometer.," *Opt. Express*, vol. 23, no. 16, pp. 20668–74, Aug. 2015.

[61] M. Deng, D. Liu, and D. Li, "Magnetic field sensor based on asymmetric optical fiber taper and magnetic fluid," *Sensors Actuators A Phys.*, vol. 211, pp. 55–59, 2014.

[62] R.-Q. Lv, Y. Zhao, D. Wang, and Q. Wang, "Magnetic Fluid-Filled Optical Fiber Fabry–Pérot Sensor for Magnetic Field Measurement," *IEEE Photonics Technol. Lett.*, vol. 26, no. 3, pp. 217–219, Feb. 2014.

[63] J. Huang, T. Wei, J. Fan, and H. Xiao, "Coaxial cable Bragg grating assisted microwave coupler," *Rev. Sci. Instrum.*, vol. 85, no. 1, pp. 1–5, 2014.

[64] A. Trontz, B. Cheng, S. Zeng, H. Xiao, and J. Dong, "Development of Metal-Ceramic Coaxial Cable Fabry-Pérot Interferometric Sensors for High Temperature Monitoring," *Sensors*, vol. 15, no. 10, pp. 24914–24925, Sep. 2015.

[65] C. Mitsumata and S. Tomita, "Negative permeability of magnetic nanocomposite films for designing left-handed metamaterials," *Appl. Phys. Lett.*, vol. 91, no. 22, p. 223104, 2007.

[66] V. P. Shilov, J.-C. Bacri, F. Gazeau, F. Gendron, R. Perzynski, and Y. L. Raikher, "Ferromagnetic resonance in ferrite nanoparticles with uniaxial surface anisotropy," *J. Appl. Phys.*, vol. 85, no. 9, p. 6642, 1999.

[67] Y. Gu and K. G. Kornev, "Magnonics: Selective heat production in nanocomposites with different magnetic nanoparticles," *J. Appl. Phys.*, vol. 119,

no. 9, p. 95106, Mar. 2016.